THE UNIVERSITY OF CHICAGO

OBSERVATIONS OF DIRECT CERENKOV LIGHT IN GROUND-BASED TELESCOPES AND THE FLUX OF IRON NUCLEI AT TEV ENERGIES

A DISSERTATION SUBMITTED TO
THE FACULTY OF THE DIVISION OF THE PHYSICAL SCIENCES
IN CANDIDACY FOR THE DEGREE OF
DOCTOR OF PHILOSOPHY

DEPARTMENT OF PHYSICS

BY
STEPHANIE ANN WISSEL

CHICAGO, ILLINOIS
JUNE 2010

To Nathan

TABLE OF CONTENTS

LIST OF FIGURES

LIST OF TABLES

ACKNOWLEDGMENTS

I was fortunate enough to meet Scott Wakely and Simon Swordy through an undergraduate research experience. Because of their influence, I became fascinated with understanding the origins of cosmic rays. Also, through their fortitude to try something new, my thesis project was born. I thank them for their support and expert guidance. Liz Hays, Brian Humensky, and Patrick "Jojo Boyle" provided tremendous guidance and insight as I was starting my graduate work. Since then, a number of people at the University of Chicago have supported me: Luis Reyes, Nahee Park, Maria Patterson, Melinda Morang, and Tom Weisgarber. I credit the above with my knowledge of the field of cosmic-ray astrophysics.

Building TrICE turned out to be one of the most enriching experiences of my graduate career, as I was able to participate in an experiment from the construction phase to decommisioning. Rich Northrop, Paul Waltz, Casey Smith and Gary Kelderhouse of the University of Chicago Engineering Center were all vital to the construction of the TrICE telescope, and also fun to learn from. Karen Byrum and Bob Wagner were also supportive of my work on TrICE.

I must acknowledge the expert technical support staff at the Fred Lawrence Whipple Observatory where VERITAS is located. Ken Gibbs and Jeremy Perkins permit the smooth operation necessary to take a multi-year measurement. The entire VERITAS collaboration is acknowledged for the construction and observing of the array. VERITAS is supported by grants from the U.S. Department of Energy, the U.S. National Science Foundation and the Smithsonian Institution, by NSERC in Canada, by Science Foundation Ireland and by the STFC in the U.K. I also acknowledge Trevor Weekes and Victor Acciari for their support while observing at the Whipple 10-m telescope. Other VERITAS collaborators who have provided useful discussions with regard to this work include, but are not limited to: Andrew McCann, Andy Smith, John E. Ward, Gernot Maier, Jamie Holder, and Lucy Fortson.

Fellow graduate students have provided tremendous support over the years, as well as a

few laughs. They include: Ali Brizius, Sophia Domokos, Shilpa Chatlani and Tom Spears. My husband, Nathan Keim, through his love and fascination with my work, renews my curiosity with particle astrophsyics. Of course, ultimately I owe my passion for science to my parents and grandparents.

ABSTRACT

Cosmic rays with energies up to at least a few PeV are confined by the magnetic fields in galaxy and therefore, expected to be accelerated within it. While there is currently no direct evidence for it, diffusive shock acceleration in supernova remnants remains the prevailing theory that explains the origin of galactic cosmic rays. Strong magnetic fields close to the shock confine particles to the shock. The particles adiabatically cross the shock and gain energy, with some probability of escaping the acceleration region that is dependent on the ratio of momentum and charge (rigidity). The finite lifetime of supernova remnants implies that particles can only be accelerated to some maximum energy, expected to be $\sim 3Z \times 10^{15-17}$ eV, where Z is the charge of the particle.

Measuring the composition of cosmic rays accurately at high energies is a unique experimental problem, because flux of all cosmic rays falls steeply with energy. Experiments flown above the Earth's atmosphere achieve elemental and sometimes isotopic charge resolution, but become limited by statistics at the few TeV/amu regime, because of their limited collecting area. Ground-based telescopes can expand the collecting area by using the atmosphere as a calorimeter and estimating the charge from the air shower properties, but have limited charge resolution. By measuring the Cerenkov radiation of the primary particle, the direct Cerenkov method is shown here to measure the flux of cosmic rays with better than 25% charge resolution.

The TrICE experiment was designed to discover direct Cherenkov radiation, by exploiting the inherent timing and angular separation between the direct Cerenkov radiation and the Cerenkov radiation produced in the particle air shower. TrICE was capable of imaging high-resolution showers using a multi-anode photomultiplier camera with angular resolution of 0.086°. While DC light was not observed over the background in TrICE, VERITAS can select for DC events by using stereoscopic techniques. VERITAS achieves a charge resolution of 21.5% and an energy resolution of 16.5%. The flux of iron nuclei are measured from 22

TeV to 141 TeV, and can be described by a power law given by $\Phi = (5.8 \pm 0.84_{stat} \pm 1.2_{sys}) \times 10^{-7} (E/50 \text{ TeV})^{-2.84 \pm 0.30_{stat} \pm 0.3_{sys}}$ TeV^{-1} m^{-2} sr^{-1} s^{-1}. The data agree well with direct measurements from satellite- and balloon-borne experiments, as well as the measurements made by H.E.S.S. using the same technique.

CHAPTER 1

INTRODUCTION

Victor Hess first discovered that radiation was coming from outside of the Earth's atmosphere in the form of cosmic rays. Cosmic rays are mostly protons, but in general are atoms accelerated to such high energies (> GeV) that they are stripped of their electrons. Their flux falls rapidly with energy, but can be described by a power law over many orders of magnitude. A confluence of supporting evidence (1.1) and theoretical developments (1.2) give credence to the idea that the expanding shocks of supernova remnants (SNRs) accelerate cosmic rays up to high energies (at least 10^{15} eV). Identifying the sources of cosmic rays (CRs) conclusively has proven to be a difficult endeavor, largely because magnetic fields deflect cosmic rays up to a certain energy, causing them to quickly isotropize. The paucity of features and power-law distribution in the all-particle spectrum (1.1) suggests that a small number of non-thermal source classes could produce the cosmic rays from 10^{12} eV up to 10^{20} eV.

Phenomenological work focuses on predicting the energy at which extra-galactic sources begin to dominate the observed spectrum, spallation of nuclei during propagation, the magnetic field enhancement near the shocks, and expected secondary production near the acceleration sites, among others. While no "smoking" gun signal of ion acceleration has been found, combining results from experiments measuring composition, anisotropy, and spectra of the cosmic rays themselves, along with the production of γ rays near the cosmic-ray acceleration sites appears to be the most promising way to approach the problem.

1.1 Properties of Cosmic Rays

1.1.1 All-Particle Energy Spectrum

The all-particle energy spectrum of cosmic rays follows a broken power law over many orders of magnitude. That the spectrum itself is nearly featureless implies a single mechanism for the acceleration of cosmic rays over many orders of magnitude in energy. The power-law shape can be generated by any acceleration mechanism wherein a fractional gain in energy is accompanied by a fractional loss in the number of the remaining particles (Fermi, 1949)

In Figure 1.1, the differential flux of cosmic rays is plotted over a wide range of energies. At GeV energies, the flux is ~ 1 cm^{-2} sr^{-1} s^{-1} GeV^{-1}, meaning that hundreds of particles stream through astronauts' hands every second. Such a flux is high enough that direct measurements can be made using balloons or satellites flown above the Earth's atmosphere. The spectrum falls steeply at a rate proportional to E$^{-2.7}$. By approximately 10^{15} eV, the geometric factors of such experiments are too low to detect the flux. Ground-based detectors measure the flux above ~ 1 TeV using the Earth's atmosphere as a calorimeter. When a high-energy particle enters the Earth's atmosphere, it interacts with air molecules, thereby depositing its energy into a large cascading particle air shower. Using surface detectors, Cerenkov counters and fluorescence detectors, experiments can exploit the large area over which the shower of particles is distributed.

There are two main features wherein the spectral index changes: the "knee" at 3×10^{15} eV where the spectrum steepens to $E^{-3.1}$and the "ankle" at 3×10^{18} eV where the spectrum flattens out. Some suggest a "second knee" appears at $\sim 10^{17}$ eV where the spectrum steepens slightly. The low-energy CRs are thought to be produced in galactic sources and confined to the galaxy. This is demonstrated by the enhanced abundance of the spallation products of nuclei as they travel through the galaxy with respect to the solar system abundances. The transition from the knee to the ankle is commonly inferred to be due

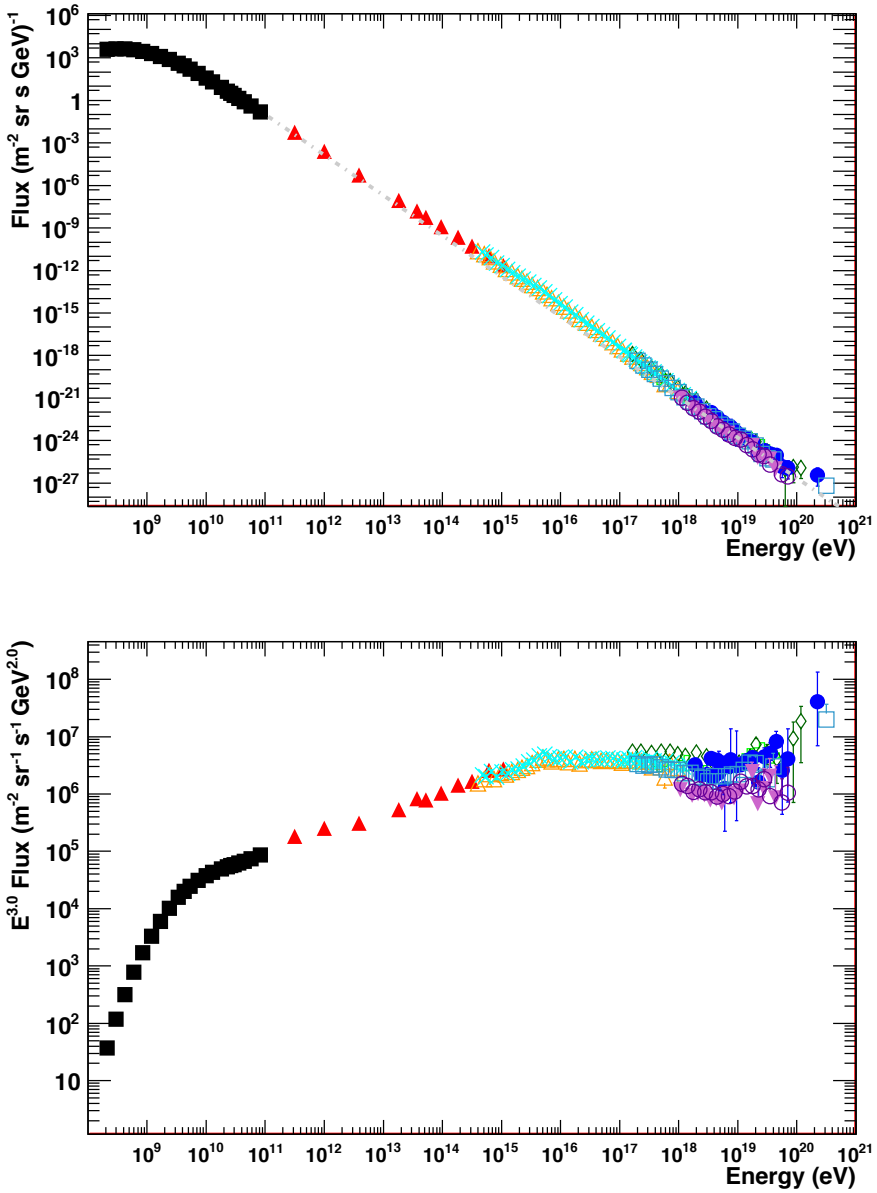

Figure 1.1: The flux of cosmic rays, compared with a power law with a slope of -2.7 (grey dashed line) in the top panel and multiplied by E^3 in the bottom panel to enhance the spectral features (modified from the version compiled by S. Swordy (Cronin et al., 1997). Hybrid data from PAO using both surface detectors and fluorescence detectors are shown in filled downward triangles (Perrone, 2008); just the surface detectors in open circles (The Pierre Auger Collaboration: J. Abraham et al., 2009).

to the transition from a spectrum dominated by galactic cosmic rays to an extra-galactic one (for a review see Hillas (2005)). The change is gradual and likely due to rigidity-dependent cut-offs in the nuclear components of the spectrum (see 1.2 for a discussion), as the dominant component switches from galactic to extragalactic. However, the precise energy at which extragalactic sources begin to dominate is under debate. Scenarios can be constructed such that the extra-galactic component overpowers the galactic component at energies closer to 10^{17} eV (Berezinsky et al., 2004), or those closer to the ankle (Wibig & Wolfendale, 2004).

Ultra-high energy cosmic rays (UHECRs, E$> 10^{17}$ eV) are also expected to interact with the CMB to produce pions via the delta resonance. This would induce a sharp steepening in flux at 5×10^{19} eV, termed the Greisen-Zatsepin-Kuz'min (GZK) cutoff after the authors who independently suggested the mechanism (Greisen (1966), Zatsepin & Kuz'min (1966)). In the 1990's, the AGASA experiment observed a flux consistent with the $E^{-3.1}$ spectrum from 10^{18} eV to 10^{20} eV (Takeda et al., 1998), while the Hi-Res experiment suggested that the GZK cutoff was in place (Abbasi et al., 2005). Differences in their detection techniques (surface detectors at AGASA and fluorescence detectors at Hi-Res) prompted interest in building a hybrid experiment combining the two such that the systematic difficulties with measuring a low flux from large particle air showers could be reduced. The Pierre Auger Observatory (PAO) is one such experiment, and it has most recently verified that the GZK cutoff to a high-level of significance (Abraham et al., 2010a).

1.1.2 Composition

The vast majority (98%) of cosmic rays are hadronic and the remaining 2% are electrons and positrons. At 10.6 GeV/nucleon, 94.8% percent of the hadronic component are protons, 4.5% are helium and less than one percent are the heavier nuclei above 1 GeV (e.g. Amsler et al. (2008)).

The chemical abundances of high-energy cosmic rays roughly mimic the solar system

abundances. Nuclei from both the solar system and the cosmic rays arriving at Earth show an oscillating pattern in which those with an even number of nucleons are more prevalent than those with an odd number (see e.g., George et al. (2009)), as expected from the carbon-nitrogen (CNO) cycle in stellar nucleosynthesis and the associated $\alpha-$particle capture mechanism (Burbidge et al., 1957). However, there are considerably more nuclei with a nuclear charge, Z, greater than 1 in the CR data than in the solar system (Amsler et al., 2008). Light elements such as lithium, beryllium, and boron are dramatically more abundant in cosmic rays than in the solar system and the elements lighter than iron are also enhanced in the CR data. This suggests that the nuclear components of galactic cosmic rays originate in stars through nucleosynthesis, and that the spallation of the nuclei during their propagation through the galaxy divide certain heavier (primary) elements into lighter (secondary) nuclei. Specifically, the spallation products of carbon and oxygen make up the LiBeB group and those of iron comprise the sub-iron group (for a review see Gaisser (1990)).

Measuring the ratio of those components gives an idea of how cosmic rays propagate through the galaxy. The spallation process will also affect the shape of the all-particle spectrum and the spectra of the individual components, because more rigid nuclei have a higher cross section for spallation. The ratio of light nuclei to the CNO group is 0.25, while the sub-iron to iron ratio is 1.5 (Longair, 1994). Recent measurements of the boron-to-carbon ratio find that they scale as $E^{-(0.5-0.6)}$ (Ahn et al. (2008) Müller (2009)). The interpretation of these data is discussed in more detail in Section 1.4.

Isotopic abundances, particularly radioactive ones, indicate the confinement time of the cosmic rays in the galaxy. In particular, the ratio of the radioactive ^{10}Be to the stable isotopes ^{7}Be and ^{9}Be is low: 0.028, implying that the cosmic rays have propagated long enough for much of ^{10}Be to decay (Garcia-Munoz et al., 1977). The most accurate measurements of isotopic abundance in the low-energy range, <100 MeV, to date have been made by the CRIS detector on the satellite ACE. CRIS found that the ^{22}Ne/^{20}Ne ratio in galactic cosmic

rays is a factor of 5 higher than that found in the solar wind. Additionally, the $^{12}C/^{16}O$ and $^{58}Fe/^{56}Fe$ ratios are also elevated (Binns et al., 2008).

The composition as a function of energy can be measured using direct experiments, flown on either balloons or satellites. All of the nuclear components can be described by a power-law spectrum in energy, with a spectral index between 2.6 and 2.7 (Ave et al. (2008) Ahn et al. (2009)). Direct experiments have not observed any cut-offs in the energy spectra up to a few TeV/amu (Ave et al., 2008).

The KASCADE experiment, however, recently reported observations of rigidity-dependent cut-offs close to the knee in the all-particle spectrum (Antoni et al., 2005). KASCADE measures the composition indirectly by reconstructing particles' masses and energies on a statistical basis from the air shower produced when the cosmic ray interacts, with limited charge resolution. Measurement techniques are described in more detail in 2.

Because heavy nuclei have smaller nuclear interaction lengths, they interact to produce large particle air showers at shallower depths than lighter nuclei. Measurements of the depth of maximum particle production at ultra-high energies disagree as to whether protons or iron nuclei are the more dominant component. Recent measurements from HiRes assert that the major component remains protonic at energies greater than 1.6 EeV (Abbasi et al., 2009). However, hybrid measurements from PAO provide strong evidence that the fraction of heavy nuclei increases with energy (Abraham et al., 2010b). Both experiments favor a break in the composition: at ankle energies ($10^{18.25}$ eV) for PAO; and at $10^{18.75}$ eV for the HiRes experiment. The break in the PAO spectrum is at the energy where they report that the composition becomes heavier.

1.1.3 Isotropy

Because of their charged nature, cosmic rays will be deflected by magnetic fields as they travel from their source to the Earth. Cosmic rays are anisotropic at the level of 1 part

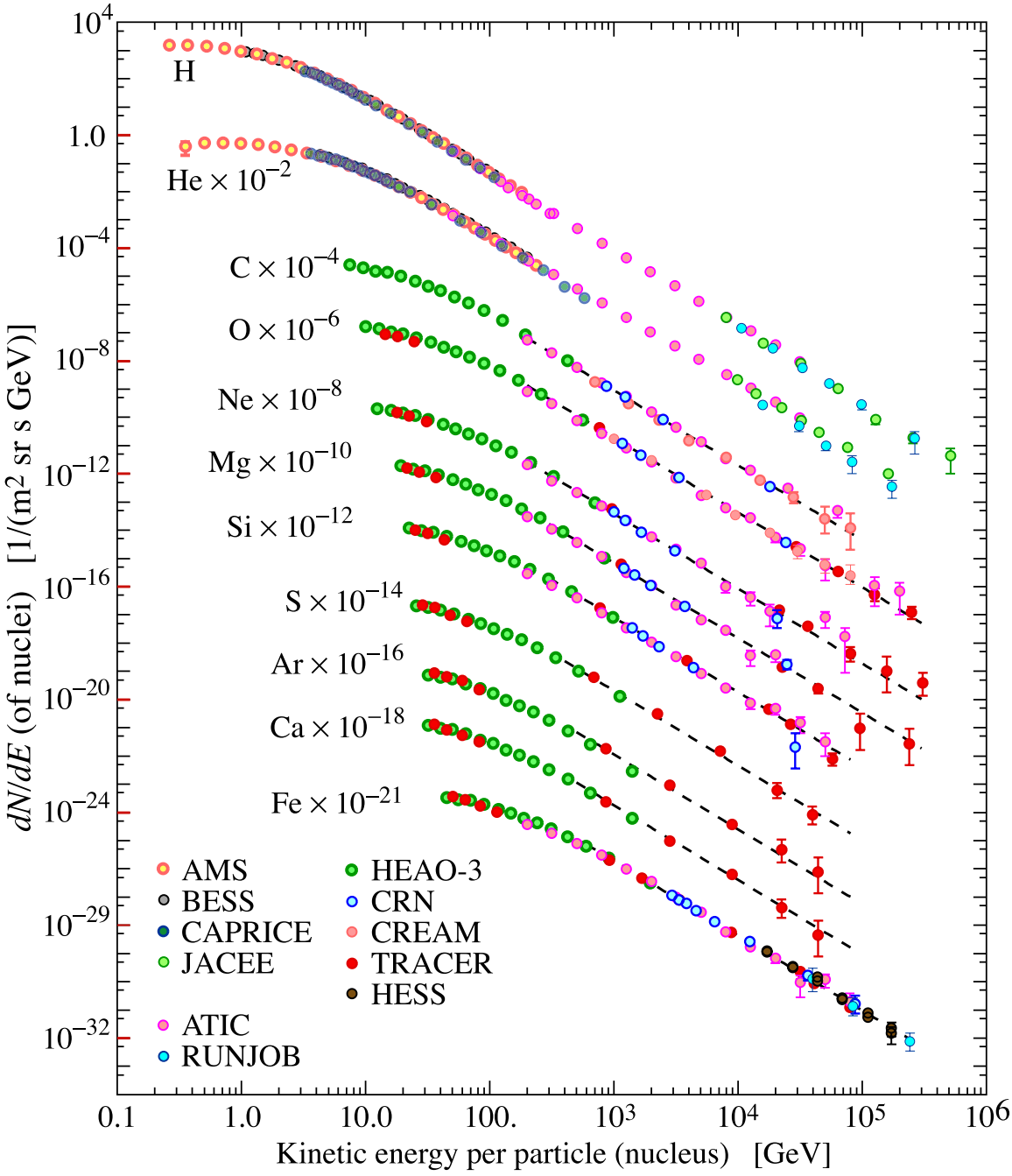

Figure 1.2: A compilation of direct measurements of the composition of cosmic rays, provided by P. J. Boyle (Amsler et al., 2008). [a]

a. Reprinted from Physics Letters, B667, Amsler, C. et al, *Review of particle physics* 1, Copyright (2008), with permission from Elsevier

in 10^3 up to energies of 10^{14} eV (e.g. Longair (1992)). If the sources of cosmic rays were unevenly distributed within the galaxy, located outside of the galaxy, or concentrated close to the solar system, anisotropies would be greater than the observed levels.

Both the expected and observed levels of anisotropy increase as a function of energy. For example, a proton accelerated to high energies within the galaxy will be deflected by the interstellar magnetic field ($\sim 3\ \mu$G $= 3 \times 10^{-10}$ T). The proton will remain confined to the galaxy if its gyro-radius is less than the smallest dimension of the galaxy (i.e., the scale height of the galaxy ~ 300 pc). For a relativistic particle, the gyro-radius, r_g, is given by the equation:

$$r_g = 3 \times 10^9 \gamma \left(\frac{B}{10^{-9} T} \right) m \tag{1.1}$$

where B is the magnetic field of interest and γ is the Lorentz factor. This means that protons with energies greater than $\sim 9 \times 10^{17}$ eV are more likely to escape the galaxy, and therefore, are expected to be anisotropic. Protons below that energy would necessarily be isotropized.

Large-scale anisotropies are still expected in galactic cosmic rays, however, due to the movement of the Earth through space. If the Earth travels through a plasma of cosmic rays as it moves around the sun, then the intensity of cosmic rays should be enhanced along the direction of motion (Compton & Getting, 1935). This effect, known as the Compton-Getting effect, has been seen diurnally among cosmic rays up to 10^{15} eV and indicates that the cosmic rays up to that energy originate in the galaxy (Cutler & Groom (1986), (Abbasi et al., 2009)). GCRs are also shown to be co-rotating with the galaxy (Amenomori et al., 2006).

MILAGRO, a ground-based water Cerenkov telescope, recently announced 2 regions of the sky with enhanced fluxes of > 10 TeV cosmic rays on small angular scales. One of the

regions of enhanced intensity corresponds to the local heliotail direction and the other is close to the galactic anti-center (Abdo et al., 2008). Protons of such an energy would have gyro-radii of 10^{-3} pc. The signature of the supernova explosion that caused the Geminga pulsar could produce an excess at the measured levels (a fractional excess of 6×10^{-4}) (Salvati & Sacco, 2008), but would also produce multipole anisotropies (Drury & Aharonian, 2008). Sources of neutrons produced in the heliotail can also be excluded (Drury & Aharonian, 2008). The origin of these anisotropies remains an open question.

1.2 Acceleration Mechanisms

Fermi pointed out in 1949 that cosmic rays could be accelerated to high energies through collisions with moving magnetic fields (Fermi, 1949). In his original treatment, clouds of hot magnetized plasma act as the magnetic mirror off of which particles stochastically gain energy. Each interaction changes the particle's energy incrementally, such that the energy gain is proportional to the square of the velocity of the plasma. It is referred to as *second order* Fermi acceleration both because the change in energy is second-order in velocity, and because while there is a net gain of energy after many encounters, the particle can either gain or lose energy with each encounter, depending on the scattering angles. Intuitively, one could argue that the net gain in energy results from head-head collisions–which more often result in a fractional energy gain–are more likely than tail-head collisions, which more frequently result in fractional energy losses (e.g. Longair (1994)). Head-head collisions result in energy gains, while the head-tail collisions result in energy losses. On average, the energy increases after many collisions, because the face-on collisions are more likely (e.g. Gaisser (1990)).

Second-order Fermi acceleration predicts a power-law spectrum. The small changes in energy build up over time so that the number of particles at a certain energy is dependent on the number of encounters and on the likelihood that a particle might escape the cloud.

Following Gaisser (1990), after n encounters the the energy, E_n is:

$$E_n = E_0(1+\xi)^n \tag{1.2}$$

where ξ is the fractional gain in energy per scatter and E_0 is the initial particle energy. After each encounter the probability of escape from the acceleration region, P_{esc}, is multiplicative, but the number of particles at a certain energy, E, is additive and results in a geometric series:

$$N(\geq E) \propto \sum_{m=n}^{\infty}(1-P_{esc})^m = \frac{(1-P_{esc})^n}{P_{esc}} \tag{1.3}$$

Solving 1.2 for n and inserting it into 1.3, a power distribution naturally emerges:

$$N(>E) = \frac{1}{P_{esc}}(\frac{E}{E_0})^{-\Gamma} \tag{1.4}$$

where $\Gamma \sim \frac{P_{esc}}{\xi}$ to first order. It is important to note here that such a power law would arise for any acceleration process which results in incremental energy gains performed many times.

A more efficient mechanism, *first order* Fermi acceleration or Diffusive Shock Acceleration (DSA), was discovered in the 1970s in which the energy gain scaled linearly with the shock velocity, instead of the square of the shock velocity (Blandford & Ostriker (1978), Krymskii (1977), Bell (1978a), Bell (1978b)). While second order Fermi acceleration accelerates particles off the irregularities in the magnetic fields of gas clouds, first order Fermi acceleration accelerates particles by using an expanding shock front as the magnetic mirror. Each time a particle crosses the shock front it gains energy proportional to the shock's bulk velocity. Thus, this mechanism is more efficient at accelerating cosmic rays, both because the energy gain is linear in velocity and each collision results in energy gain.

Consider a system with a blast wave moving at supersonic speed, v_1, into a cold medium at rest. The shocked medium behind it moves at v_{rel}. In the rest frame of the shock, the shocked medium moves away at speed v_2, while the unshocked medium moves towards it at v_1. (Note that in the reference frame of the unshocked medium, $v_{rel} = v_1 - v_2$.) The fluid must follow the shock jump conditions, known as the Rankine-Hugionoit relations, that preserve mass, momentum, and energy across the shock. If the shock expands into a cold medium, the temperature, and therefore pressure, in the unshocked medium are small compared to the hot compressed gas behind the shock. In this case, the shock jump conditions reduce to:

$$\begin{aligned} \rho_1 v_1 &= \rho_2 v_2 && \text{mass conservation} \\ \rho_1 v_1^2 &= P_2 + \rho_2 v_2^2 && \text{momentum conservation} \\ \frac{1}{2} v_1^2 &= \frac{\gamma}{\gamma - 1} \frac{P_2}{\rho_2} + \frac{1}{2} v_2^2 && \text{energy conservation} \end{aligned} \tag{1.5}$$

where the ρ's are the densities, the v's are the velocities, the P's are the pressures in the unshocked (indicated by the subscript "1") and the shocked media ("2"). γ represents the ratio of the specific heats of the two media. It is convenient to define a compression ratio across the shock $\sigma \equiv \frac{v_1}{v_2}$ which is also equivalent to ρ_2/ρ_1 due to mass conservation. The continuity equations 1.5 can be solved to find that

$$\sigma = \frac{\gamma + 1}{\gamma - 1} \tag{1.6}$$

which reduces to 4 for a monatomic gas ($\gamma = 5/3$) and is generally true for non-relativistic shocks.

Particles are scattered and quickly isotropized off of the small-scale magnetic field irregularities on both sides of the shock front. High-energy particles move with a speed close to

c, but the average velocity of each medium is much lower than that, so the particles can cross the shock many times and still be contained in the acceleration region. Particles gain an energy upon each cycle back and forth through the shock of $\xi = \frac{4}{3}\frac{\sigma-1}{\sigma}\frac{v_1}{c}$. However, since the shocked medium is moving away from the shock front, a particle can eventually escape the acceleration region. The probability of escape is given by $P_{esc} = \frac{4}{\sigma}\frac{v_1}{c}$. Solving 1.4 for Γ:

$$\Gamma = -\frac{P_{esc}}{\xi} = -\frac{3}{\sigma - 1} = -1 \tag{1.7}$$

So the differential flux of cosmic rays produced at a strong, plane wave shock in the DSA framework should follow a power law in energy with an index of -2.0.

Particles trapped in the acceleration region must obey the diffusion equation with a momentum-dependent diffusion coefficient $D(p)$. Krymskii (1977) emphasizes that particle acceleration, taken in this context, is a rather slow process. In the steady-state solution, the time taken for a cosmic ray to make one cycle back and forth across the shock front, T_{cycle}, determines the amount of time it takes for a particle to be accelerated to a momentum p:

$$\begin{aligned} T_{cycle} &= \frac{4}{v_{part}}\left(\frac{D_1}{v_1} + \frac{D_2}{v_2}\right) \\ \frac{dp}{dt} &\approx \frac{\Delta p}{T_{cycle}} = \frac{p}{\frac{D_1}{v_1} + \frac{D_2}{v_2}} \end{aligned} \tag{1.8}$$

Therefore the time it takes to accelerate a particle would be dependent on the spatial diffusion coefficient, and the time that a shock remains strong sets a limit on the maximum energy that it can produce. The diffusion coefficient is rigidity-dependent; Lagage & Cesarsky (1983) derive a minimum diffusion coefficient dependent on the charge of the particle, Z, the magnetic field, B, and the particle's kinetic energy, pc, of $D(p) = r_g c/3 = pc/3ZeB$.

1.3 Acceleration Sites

The preferred candidates for the sites of shock acceleration are the expanding shocks of supernova remnants for three main reasons:

- the shocks of SNRs can provide the energy density found in cosmic rays
- the expected flux spectrum from supernova remnants matches the all-particle spectrum when corrected for propagation effects
- the maximum energy expected from supernovas extends from the 10^{15}–10^{17} eV

Cosmic rays require $\sim 10^{41}$ erg/s, assuming that the power needed to replenish them is the energy density in cosmic rays (1 eV cm^{-3}) times the volume of the Milky Way divided by the residence time of cosmic rays in the disk (2×10^7 yr from the secondary to primary ratios). Between two and three supernovae explode every century in the Milky Way, and since each supernova produces 10^{51} ergs, then the power available from supernova shocks is 10^{42} erg/s. If 10% of the explosive energy produced by each supernova goes into particle acceleration, then SNRs can provide the energy required.

Radio observations of supernova remnants typically have power law spectra (with a spectral index α), so it is appropriate to assume that the momentum distribution of electrons in the shells also follows a power law in momentum: $f \propto p^{-(3+2\alpha)}$. Diffusive shock acceleration predicts a universal power-law spectrum in momentum – dependent only on the compression ratio of the shock, σ – of the form: $f \propto p^{-3\sigma/(\sigma-1)}$. So the theory would be consistent if $\alpha = \frac{1}{2}$ (Drury, 1983). Electron acceleration in SNR shocks is evident in the non-thermal X-ray imaging of RXJ 1713.7-3946 where the thin filaments of X-rays indicates that strong magnetic fields are present (Uchiyama et al., 2007).

An astrophysical source can only accelerate particles if its radius is larger than the particle's Larmor radius, otherwise the particle will escape the acceleration region. This implies

that a source of a certain size and magnetic field strength can only accelerate particles to a finite maximum energy, E_{max}, given by the equation (Hillas, 1984):

$$E_{max} = 3B_{source}R_{source}V_{shock}Z \text{ [eV]}. \tag{1.9}$$

For SNRs, the magnetic field behind the shock is thought to be 3 times that of the ISM ($\sim 9\mu$G), which places the maximum energy produced by SNRs at $3Z \times 10^{15}$ eV. More strict limits can be placed on the maximum energy, as in the case of Lagage and Cesarsky's claim that protons can only be accelerated to 10^{13} eV in SNRs if you only consider incremental changes in energy over the lifetime of a SNR (Lagage & Cesarsky, 1983). However, when considering changes in the compression ratio of the shock to the ISM and self-amplification of magnetic fields, maximum energies even up to 10^{17} eV can be produced in supernova remnants (Bell & Lucek, 2001).

Massive stars that generate wind-blown shocks and develop into Wolf-Rayet stars or that eventually explode into supernovae are more concentrated in dense star-forming regions, like OB associations. After $\sim\ 5-6$ supernovae, the shocks from these explosions can merge together to form a superbubble. Particle acceleration is likely to occur in the many shocks contained within the superbubble, and there is some evidence that this is happening, at least in the energy range where the isotopic abundance is available.

The anomalous ^{22}Ne/^{20}Ne ratio can be explained as the summed contributions from Wolf-Rayet stars and supernova ejecta being injected into the acceleration region (i.e., the shocks of supernovae within the superbubble). Twenty percent of the GCR material must have originated as WR stellar ejecta in order to properly account for this ratio (Higdon & Lingenfelter, 2003) (Binns et al., 2005). Furthermore, the low level of the radioactive isotope ^{59}Ni in GCRs demonstrates that it must have been accelerated 10^5 years after synthesis in

supernovae to provide enough time for its decay via electron capture: ^{59}Ni$\rightarrow^{59}$Co (Binns et al., 2008). Speculative theories can be made to explain these observations in conjunction with others, such as where Streitmatter & Jones (2005) use a two-component (proton and iron) model of superbubble-accelerated cosmic rays to reproduce the sharp knee of the cosmic-ray spectrum and to predict that the second knee arises from the rigidity-dependent escape of cosmic rays out of the Local Bubble in which the Milky Way resides.

Acceleration across the galaxy and even into the extended halo could also accelerate particles up to high energies in a more distributed fashion. While this idea does not exclude SNRs and superbubbles from being the site of first acceleration, it is possible that re-acceleration at the galactic termination shock and in other regions dispersed through the galaxy could help explain the low-level anisotropy of GCRs and in some models, predict the cosmic-ray spectrum up to the second knee (Seo & Ptuskin, 1994).

1.4 Cosmic-ray Propagation

After being accelerated, cosmic rays will diffuse through the galaxy and collide with material therein. Measurements of the secondary to primary ratios indicate that CRs are confined until they travel through ~ 1 gm/cm^2 of matter at 1 TeV/amu (Swordy et al., 1990). Their motion can be modeled by the transport equation that states that the time-derivative of the number of particles is equal to the sum of a diffusion term, an energy loss and gain term (through re-acceleration), a convection term, a source term, a spallation term and a cascade term (Gaisser, 1990).

Turbulence in the galactic magnetic fields can scatter particles as they propagate. A simple model assumes self-similar perturbations in the magnetic field over many correlation lengths throughout the galaxy, and predicts that the diffusion coefficient follows a Kolmogorov scaling law in rigidity: $R^{-1/3}$ (Strong et al., 2007). More complex models predict a $R^{-1/2}$ scaling law, which agrees better with recent measurements of the boron-to-carbon

ratio (Müller (2009) Ahn et al. (2008)).

The simplest model of propagation, the Leaky Box Model, assumes that evenly distributed sources inject high-energy particles into a volume (or box) where they are contained for some time, τ_{esc}, before leaking out of the galaxy. The probability of escape is constant and independent of spatial position (Strong et al., 2007). The escape path length, λ_{esc} scales with the escape time as $\lambda_{esc} \equiv \rho\beta c\tau_{esc}$, where rho is the mean density of interstellar gas and *beta* is the ratio of the particle's velocity to the speed of light. Then the cosmic-ray transport equation reduces to a diffusion term ($-N/\tau_{esc}$), a source term, a spallation term and a cascade term. Solving for λ_{esc} yields a power-law in rigidity of index $\delta \approx 0.6$, so higher energy particles are more likely to escape. If the source generates cosmic rays with a flux $\sim E^{-\alpha}$, then the spectrum measured at Earth will be $E^{-\alpha-\delta}$ (Gaisser, 1990).

More complicated models can be constructed, such as the Nested Leaky Box Model, where the cosmic-ray sources are concentrated in regions of high matter density, which would predict a plateau in escape time above a certain energy (Swordy et al., 1990). In detailed simulations, sources are typically assumed to be more concentrated towards the center of the galaxy (Strong et al., 2007), as indicated by differences in diffuse gamma-ray spectra towards the inner and outer regions of the galaxy (Hunter et al., 1997).

The confinement time of cosmic rays can be constrained by measuring the flux of radioactive isotopes and their daughter products, like ^{10}Be and ^{26}Al. Garcia-Munoz et al. (1977) showed that because much of the ^{10}Be isotope had decayed before reaching the solar system, the escape time was longer than the ^{10}Be half-life. Therefore, the confinement time of the GCRs in the galaxy is $\sim 2 \times 10^7$ years.

1.5 Gamma-ray Production at CR Acceleration Sites

High-energy gamma rays will be produced when cosmic rays interact with protons in molecular clouds, magnetic fields or ambient electromagnetic radiation, such as starlight or the

cosmic microwave background. Thus, observations of gamma rays from potential cosmic-ray production sites could provide the direct evidence necessary for identifying the sources of cosmic rays.

Proton-proton collisions can produce gamma rays by generating neutral pions which then decay into two gamma rays: $p + p \rightarrow \pi^0 \rightarrow 2\gamma$. High-energy electrons also produce gamma rays through bremsstrahlung in the presence of an atom and through inverse Compton radiation, in which the high-energy electron up-scatters a lower-energy photon. Even though electrons should be accelerated along with the nuclear material in the supersonic shocks, leptonic gamma-ray emission can also be due to more complicated astrophysics, such as the winds of pulsars commonly found in the center of supernova explosions resulting in pulsar wind nebula (core-collapse supernovae). Secondary emission also arises from charged pion interactions that decay into muons, neutrinos and electrons. The electrons can then produce gamma rays via pair production.

Thus, the cleanest way to identify cosmic-ray acceleration at shock fronts is to first detect gamma-ray emission from the shell of a supernova and then clearly show that it is of hadronic origin. Naturally, to confirm that the entire class of supernovae are indeed the main accelerators of cosmic rays, this process need be repeated for many SNRs at various stages in their evolution. On the other hand, clearly establishing leptonic origin of gamma-ray emission in SNRs probes the local environment of the SNR (Porter et al., 2006). Association with a molecular cloud that provides the target material for protons and nuclei to undergo photopion production or the detection of gamma rays at energies above the cutoff expected for electrons due to synchrotron losses (> 100 TeV) points to hadronic origin while the case where non-thermal X-rays are spatially coincident with the TeV emission favors leptonic emission. In both cases, detailed spectral modeling is necessary.

Gamma rays from number of shell-type supernova remnants have been detected at VHE energies with ground-based instruments. Table 1.1 gives a brief description of the high-

energy observations and show that notable SNRs favor a hadronic origin of gamma-ray production (RX J1713.7-3946, W 28, CTB 37B, RX J0852.0-4622), one strongly favors a leptonic scenario (RCW 86), but that most cannot confirm or exclude one scenario or the other. Older SNRs like IC 443, G106.3+2.7 and W 28 exhibit gamma-ray emission that could be associated with a molecular cloud (MC) and therefore indicative of hadronic emission. However, IC 443 and G106.3+2.7 are both close to pulsar wind nebulae (PWNe) that could accelerate electrons to high energies, which would then interact with the molecular cloud.

Looking at other galaxies with regions of high star formation is another way to seek out evidence for cosmic-ray acceleration in shocks. Star-forming regions have high cosmic-ray densities, because the elevated stellar density implies that there would be more supernova explosions that produce shock fronts wherein particles are accelerated. Recent VERITAS and H.E.S.S. observations of starburst galaxies demonstrate high-energy particle acceleration in M 82 (VERITAS Collaboration et al., 2009) and NGC 253 (The HESS Collaboration: F. Acero, 2009). Observations by Fermi confirmed their results in the lower energy regime (Fermi LAT Collaboration & Abdo, 2009). Because the starburst galaxies exhibit negligible active galaxy activity from the central black hole (as in the case of radio galaxies), and no relativistic jets (as in the case of blazars) to power gamma-ray production, the gamma-rays were likely produced by cosmic rays in regions with many shocks. However, the connection established between star-forming regions and particle acceleration does not exclude the possibility that the main accelerators are larger shocks from superbubbles or galactic rotation (Butt, 2009). The γ-ray spectrum from M 82 agrees with existing hadronic emission models, but the data cannot exclude leptonic emission.

1.6 Summary

Measurements of abundances of radionuclides indicate that cosmic rays up to high energies are confined to the galaxy for $> 10^7$ years, and therefore, likely to have been produced within

Table 1.1: Short summary of gamma-ray observations of SNRs from the VHE γ-ray catalogue TeVCat (Horan & Wakely, 2008). The abbreviations "H." (hadronic), "L." (leptonic), and "U." (uncertain) are used to indicate which gamma-ray production mechanism is favored. "Γ" indicates the spectral index on the power-law fit to the energy spectrum.

Name	Emis.	Observations	Reference
IC 443	U	Maser emis. & MC close to γ-ray centroid., supports H. PWN possible site of L.	Acciari et al. (2009b) Albert et al. (2007a)
RX J0852.0-4622	H	Thin-shell of γ-rays and spectrum disfavor L.	Aharonian et al. (2007)
RCW 86	L	$\Gamma = -2.4, > 1$ TeV; H. req. break in spec. below 1 TeV	Aharonian et al. (2009)
SN 1006	U	Two distinct lobes of emis. in NE & SW	Naumann-Godo et al. (2008)
RX J1713.7-3946	H	Lack of spectral break up to 100 TeV disfavors L.	Aharonian et al. (2007a)
CTB 37B	H	γ-ray obs. likely from shell. X-ray obs. cons. with thermal emis.	Aharonian et al. (2008a)
CTB 37A	U	γ-ray & X-ray emis. likely from MC interacting with SNR. PWN would favor L.	Aharonian et al. (2008b)
W 28	H	γ-ray emis. displaced from W28, but coincident with MC fields. Older SNR favors H. because of rapid electron energy losses.	Aharonian et al. (2008c)
OFGL J1954.4+2838	U	Field spatially coincident with SNR G65.1+0.6 and PSR 1957+2831	Abdo et al. (2009)
G106.3+2.7	U	Extended TeV emis. close to MC, VERITAS meas. from 1-12TeV and MILAGRO meas. > 35 TeV favor H. PWN not clearly disassociated with TeV emis.	Acciari et al. (2009a) (Abdo et al., 2009)
Cassiopeia A	U	Young SNR in clean environment with lower than expected flux. Unable to distinguish L. from H.	Aharonian et al. (2001) Albert et al. (2007b) (Acciari et al., 2010)
VER J2019+407 γCygni	U	TeV centroid overlaps with radio contours of shell, but PWN not excluded	Weinstein (2009)

it. Extensive theoretical work in the field of diffusive shock acceleration provides a framework in which supernova remnants (or other powerful cosmic accelerators with strong shocks) can accelerate these galactic cosmic rays up to a certain rigidity-dependent energy. Ratios of isotopic abundances at low energy indicate a significant portion of the particles injected into the acceleration site must come from winds blown off of WR stars. Particle acceleration is seen in some supernova remnants, but there are too few gamma-ray observations as of yet to make the claim that they are the main accelerators. Measurements of the composition of cosmic rays above energies where direct measurement techniques become limited by statistics are needed to explore the energy range where supernova remnants are expected to cut off.

CHAPTER 2

OBSERVATIONAL TECHNIQUES

The previous chapter explains how critical measuring the composition of high-energy cosmic rays is to understanding their origin, but two factors make this a unique experimental problem: the rapidly falling flux with increasing energy and the interactions of cosmic rays with the atmosphere. The latter issue actually enables researchers to circumvent the former, but comes at a cost in charge resolution. Here, I describe the methods used for measuring the composition of cosmic rays, including one where the charge of a cosmic ray can be determined by measuring Cerenkov radiation coming from the primary particle itself (see Section 2.4), which is the subject of this thesis.

Figure 2.1 shows a high-energy particle as it enters the atmosphere. The cosmic ray quickly interacts with the atmospheric molecules, producing an extensive air shower (EAS) that can be considered the superposition of many pion-induced hadronic cascades and electromagnetic showers. Direct methods (discussed in 2.1) avoid the secondary particles by flying above the height at which the cosmic ray first interacts hadronically, while indirect methods (discussed in 2.3) measure the secondary particles and radiation produced in the air showers.

Satellites and balloons can measure the energy and trajectory of incoming cosmic rays directly, because they fly above the Earth's atmosphere. These techniques boast impressive charge resolution, being able, in some cases, to determine the isotopic abundance, but are limited by the collecting area available (< 5 m^2 sr). Ground-based telescopes sample the particles or radiation generated in the air showers from primary cosmic rays interacting with the atmosphere. In this way, they can reach a higher energy regime by expanding the collecting area, but are dependent on the hadronic interaction models and have poor charge resolution. The direct Cerenkov technique seeks to marry the two methods by using an electromagnetic process to measure the charge of the incoming particle and standard

techniques from imaging Cerenkov telescopes to measure the energy.

2.1 Direct Measurement Techniques

As a cosmic ray travels through a dense medium, it interacts with the medium either through radiation or energy deposition. The charged particles can disrupt or ionize parts of the material leaving behind tracks. One measurement technique is to construct a dense detector block, expose it to cosmic rays and then recover the tracks left behind either through nuclear emulsions or etching (Gaisser, 1990). Nuclear emulsion chambers and calorimeters are examples of destructive techniques, because the particle must deposit its energy into the detector.

When traversing a material the cosmic ray will ionize the medium, losing energy as it travels through more material and eventually stopping. Ionization losses per unit track length depend only on the energy and charge of the incoming particle, rather than its mass. Each cosmic ray will leave a unique signature in an ionizing detector (Longair, 1992). Geiger-Müller counters and proportional tubes measure the energy deposited through ionization.

The cosmic ray can also collide with molecules in the detector, knocking off electrons and producing brief flashes of light or scintillation. Scintillation counters are common place in space-borne and balloon-borne experiments because they are inexpensive and light, and can directly measure the charge of the particle. Tracking hodoscopes are constructed out of multiple layers of scintillation paddles and will often be used in conjunction with other techniques.

Relativistic charged particles also stimulate the atoms in a medium to oscillate. When the particle moves faster than the speed of light in the medium, the wave-fronts generated during these oscillations add coherently, producing Cerenkov radiation, as shown schematically in Figure 2.2. Each atom emits a photon moving at group velocity c/n. If the charged particle moves faster than the group velocity of light in the medium, the wave fronts add coherently

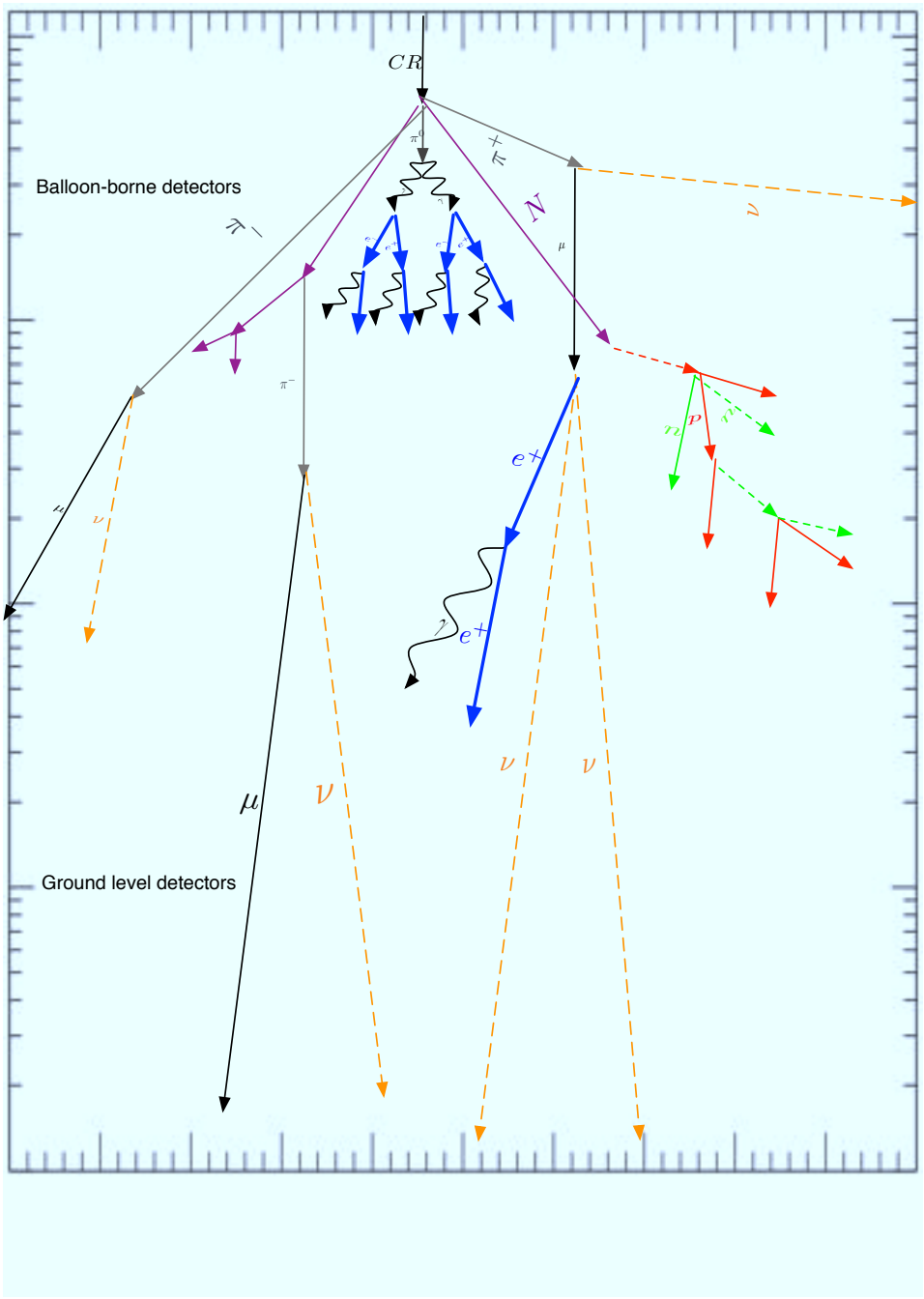

Figure 2.1: A cartoon of the particle air shower produced by a cosmic ray as in enters the atmosphere. Detectors on the ground, like muon and electron counters, Cerenkov counters, imaging Cerenkov telescopes and fluorescence detectors sample characteristics of the showers, while balloons and satellites collect the particles directly by flying above the mean first interaction height.

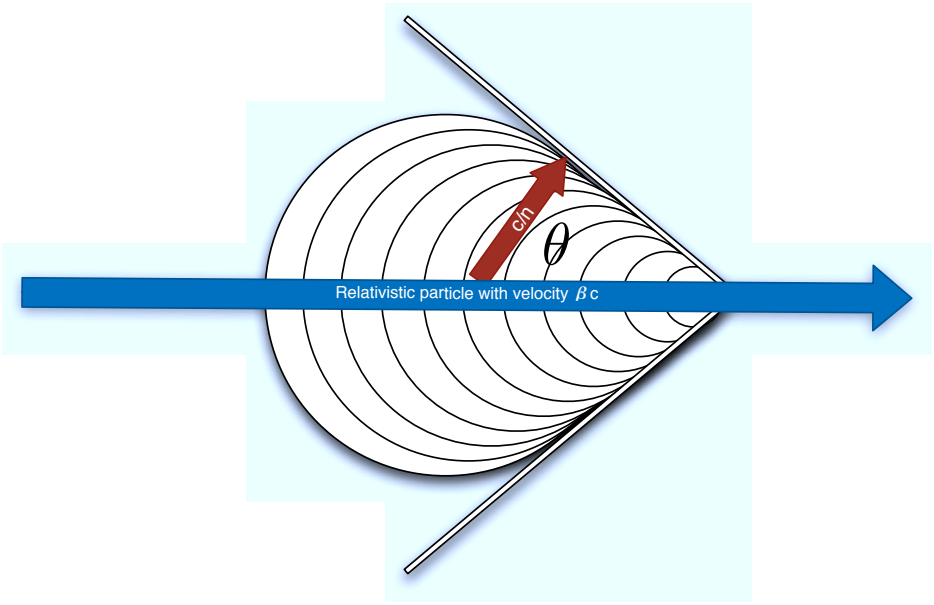

Figure 2.2: Cerenkov radiation

to produce radiation with a characteristic angle, θ_C, given by equation 2.1:

$$\cos\theta = \frac{1}{\beta n(\omega)} \tag{2.1}$$

The number of photons produced per unit track length scales with the square of the charge, so using a Cerenkov counter is a convenient way to measure the charge of the incoming particle. Aerogel silica have adjustable indices of refraction, permitting the experimenter to select the energy range probed by the instrument. The Cerenkov light can be collected using fast photomultipliers. Cerenkov radiation will be discussed in more detail in Section 2.4.

Charged particles will also initiate transition radiation when passing through the boundary between materials with different dielectric constants. Energy is released in photons due to the rapid change in electric field as the particle crosses the boundary. The photon yield is proportional to the relativistic gamma-factor of the particle.

Instruments based on destructive techniques can be massive, often too heavy to fly on

a balloon or satellite. In contrast, scintillation counters, Cerenkov counters, proportional counters and transition radiation detectors are non-destructive, because they measure radiation produced by a particle as it streams through the detector. Typically, many particle detectors are used in coincidence to accurately reproduce the particles' tracks and achieve optimal charge and energy resolution over a wide dynamic range.

Table 2.1: Comparison of direct methods. Balloon-borne experiments are labelled with a "B"; satellite-borne experiments, an "S". The charge resolution, $\Delta Z/Z$, geometric factor and energy range are given for a number of direct experiments flown since 1979.

Experiment	Type	Lifetime	$\Delta Z/Z$ [%]	Area [m^2 sr]	Fe Energy Range [GeV/amu]	Reference
HEAO-C3	S	1979–1981	6	0.04	$10 - 10^2$	Binns et al. (1988)
CRN SpaceLab	S	1985	3	2	$10 - 10^3$	Grunsfeld et al. (1988)
ACE CRIS	S	1997–present	1[a]	0.015	$0.05 - 0.5$	George et al. (2009)
ATIC	B	2001–2007	8	0.45	$0.5 - 3500$	Guzik et al. (2008)
TRACER	B	2003–2006	4	5	$1 - 1000$	Ave et al. (2008)
CREAM	B	2004–present	3	0.46	$10 - 1000$	Ahn et al. (2009)

[a] CRIS measures the mass of each particle in addition to its charge using ionization in silicon solid state detectors. The peaks in the charge histogram are clearly separated and include additional peaks for the isotopes of each element

Balloons and satellites can carry payloads up to 3600 kg. Satellites fly for typically 5-10 years, while balloon flights usually last a few weeks. As shown in Table 2.1, balloon- and space-borne experiments detect elemental, and in some cases isotopic, cosmic-ray abundances

in the MeV/amu to TeV/amu energy band. The charge resolution (typically better than 5%) of these experiments permits event-by-event reconstruction of each cosmic ray. However, they are limited by the size of the detector permitted to fly in space. A payload with a geometric factor 1 m^2 sr, flown for two weeks would detect, at most, 1 cosmic ray with an energy > 1 PeV. Expanding the detector area, as in the case of TRACER, accumulating statistics over the course of many flights, as in the case of CREAM, or developing capabilities for ultra-long duration balloon (> 100 days) flights will allow these experiments to probe the knee energy regime.

2.2 Cosmic-ray air showers

When high-energy particles encounter the Earth's atmosphere, they interact with the surrounding medium to produce a cascade of particles, often producing in excess of 10^{10} particles in a single shower. Ground-based cosmic-ray detectors focus on identifying air shower properties and using them to reconstruct the energy, arrival direction, and type of incoming particle.

2.2.1 Extensive Air Shower Development

When a cosmic ray enters the atmosphere it will collide with molecules in the air, rapidly producing many particles, most of which will decay or produce new, or secondary, particles. The secondary particles themselves will undergo interactions, and this process continues until the incoming particle's energy divides among enough particles that they are more likely to decay or dissipate their energy through ionization. The entire shower lasts for only microseconds, but can generate a cascade with a footprint > 10 km^2 for the highest-energy cosmic rays.

Most of the energy in the shower goes into the electromagnetic channel, so understanding

the processes involved is important. Rossi & Greisen (1941) treated air showers analytically by solving coupled cascade equations that consider pair production, bremsstrahlung radiation and collisional loses. The solutions to these diffusion equations yield three fundamental, macroscopic properties of electromagnetic showers (i.e., those generated by $e^{\pm}$ or γ rays):

$$N_{max} \propto E \tag{2.2}$$

$$\chi_{max} = \chi_0(\ln \frac{E}{E_0} - n),\ n = 1e^{\pm}, 0.5\gamma \tag{2.3}$$

$$\frac{dN}{dE} \sim \frac{\exp(\lambda(s)t)}{E^{s+1}}) \tag{2.4}$$

The number of particles produced at the depth of maximum, N_{max}, scales with the particle's energy, E. The depth of that maximum, χ_{max} in g cm^{-2}, grows with the logarithm of the energy. The energy spectrum of the new particles produced steepens with the shower's age, $s \equiv \frac{2n+3\chi}{\chi+2\ln\frac{E0}{E}}$. In other words, the number of low-energy particles builds as the shower develops.

In an effort to approach this complex problem using simple arguments, Heitler first introduced a simplified description of the development of electromagnetic extensive air showers, using only inelastic collisions (Heitler, 1954). Matthews (2005a) revisited this model and I follow his description here. An incoming photon with energy $E_{\gamma,0}$, will likely interact within one splitting length, defined as the distance, d, over which electron will radiate away one half of its energy, on average. Thus, $d = \lambda_r \ln 2$ where λ_r is the radiation length (37 g cm^{-2} in air). The interaction will produce an electron-positron pair with the photon's energy divided equally between the electron and positron. Each e$^{\pm}$ pair will produce more photons through bremsstrahlung radiation, which will then also produce another leptonic pair. A schematic illustration is shown in Figure 2.3. The total number of particles doubles within each splitting length, so that after the n-th splitting length, there will be $N = 2^n$ particles,

each with a total energy of $E_n = \frac{E_{\gamma,0}}{2^n}$. This process continues until the average electron energy reaches a critical energy where it is equally likely to lose energy through collisional losses in the atmosphere as it is to radiate bremsstrahlung photons. For electrons in air, the critical energy, E_{cr} is ~ 85 MeV. So a 10 TeV photon-induced shower will cease particle production after 16 splitting lengths, having generated 10^5 particles.

This simple model can be expanded to include nuclear interactions. Protons, for instance, will pass through a certain distance, d_I, before undergoing a strong interaction with air molecules that divides its energy, $E_{p,0}$ in two. Here, the relevant path length is given by the nuclear interaction length in the medium, λ_I, so that the relevant splitting length becomes $d_I = \lambda_I \ln 2$. The strong interaction will produce some number of pions: the charged ones will continue to interact hadronically and eventually decay into muons, while the neutral ones will decay quickly into two photons. Therefore, the $\pi^{\pm}$'s generate a series of hadronic sub-showers, while the π^0's initiate the electromagnetic showers described above. As before, the energy is divided among all of the particles produced in an interaction length. So assuming that the number of charged pions produced in each nuclear interaction is $N_{ch} = 10$, then after n interaction lengths, there will be $N_{\pi^{\pm}} = (N_{ch})^n$ charged pions with an average energy $E_{\pi^{\pm}} = \frac{E_{p,0}}{(3/2N_{\pi^{\pm}})^n}$. The hadronic portion of the shower will subside when the decay length for the charged pions is less than the interaction length. Typically, this will occur after $n = 3 - 6$ interaction lengths, leaving behind a series of lower-energy electromagnetic cascades and penetrating muons.

In each case, the primary energy is easily calculable if you can accurately measure the number of particles produced. For the electromagnetic shower, $\chi_{max} = \lambda_r \ln (E_{\gamma,0}/E_{cr,e})$ and for the hadronic shower it would be $\chi_{max} = \lambda_I \ln(E_{proton}/E_{cr,\pi})$. Note that χ_{max} scales as a logarithm with the primary energy.

In this simple framework, nuclear interactions from high-mass cosmic rays can be considered superpositions of many smaller protonic sub-showers. A particle of nuclear mass

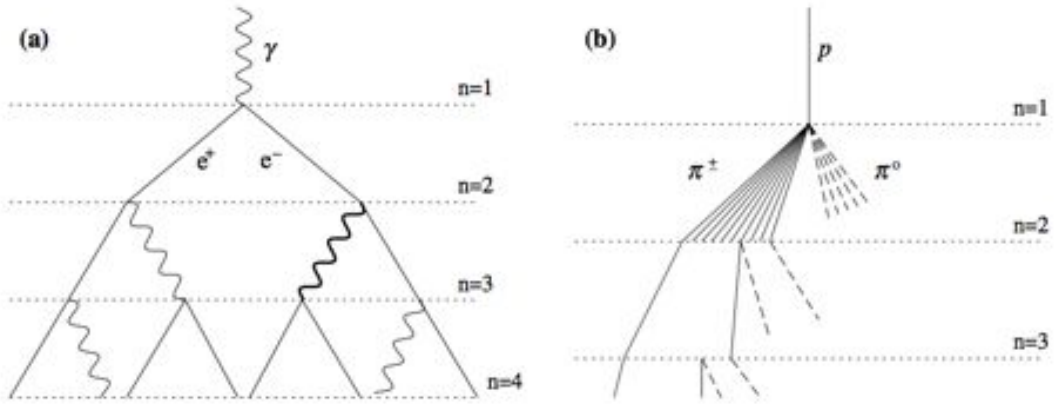

Figure 2.3: The Heitler model of electromagnetic (a) and hadronic (b) air showers. Neutral pions decay rapidly into electromagnetic showers. Charged pions continue to propagate hadronic showers (not all pion lines are drawn beyond n=2). [a]

a. Reprinted from Astroparticle Physics, 22, Matthews, J., *A Heitler model of extensive air showers*, 387, Copyright (2005), with permission from Elsevier.

number, A, and energy, E_A, would undergo nuclear collisions to produce many proton, each of energy $\frac{E_A}{A}$. The subsequent protons would then quickly be converted to pions and the hadronic and electromagnetic cascades ensue. The maximum depth would arrive earlier than for a simple proton shower, because the initial energy is divided among A^n particles after the n-th step for the nuclear shower and only 3^n particles for the proton shower: $\chi_{max} \rightarrow \lambda_I \ln(E_{proton}/AE_{cr,\pi})$. Additionally, nuclear showers will produce more muons than proton showers at the same initial energy.

The simple model is useful for understanding the overall development of the extensive air shower and the interactions therein, but it tends to overestimate the difference in χ_{max} between proton and iron showers by a factor of 50% (Fowler, 2000). The amount of energy going into the electromagnetic component varies from shower to shower. The depth of first interaction also varies according to the nuclear interaction cross sections of the primary particle, which depends on the incoming cosmic ray's mass and energy. Detailed Monte Carlo simulations are necessary for fully reconstructing a cosmic ray's energy, because full cross-

sections of the interactions involved must be used and because of the random fluctuations described above.

2.3 Indirect Measurement Techniques

Indirect methods for measuring the composition of cosmic rays collect secondary particles or radiation produced in the EAS to reconstruct the information about each incoming shower. For example, measuring the ratio of muons to electrons in a CR-induced air shower distinguishes purely electromagnetic showers from hadronic ones. The energy can be reconstructed by either sampling the secondary particle production either along the shower (longitudinally) or in a plane intersecting the air shower cone (laterally). In all cases, the charge can be reconstructed by estimating the depth of maximum particle production, because $\chi_{max} \propto \ln(\frac{E}{AE_{crit}})$.

Ground arrays measure the distribution of particles at a particular depth in the air shower, the depth at which the air shower impacts the ground. Cerenkov counters, constructed out of either Winston cones or large water tanks, map out the lateral development of an air shower that depends on χ_{max}, the primary's energy and electron multiple scattering. The arrival direction can be reconstructed by comparing the triggering times at each detector. The total number of particles sampled at the ground can vary dramatically because the variation in first interaction height changes the amount of material traversed by each shower. Reconstructing the lateral distribution also indicates the depth of maximum and therefore the primary's charge. Muon counters, placed underground, are sensitive to the hadronic component of the shower as well.

The longitudinal development of the shower can also be reconstructed by collecting the radiation produced along the shower. Fluorescence light is emitted by the atmosphere as the EAS particles stream through it. This light is emitted isotropically, permitting wide-angle observations. Cerenkov light is relativistically beamed, but produces a detectable signal at

lower energies ($\sim$ few hundred GeV). The air shower produced by a 1-TeV γ ray will generate $\sim 10^7$ Cerenkov photons, but they are spread out over a circle of radius $\sim$ 100 m so that the photon density is only 300 m^{-2}. Imaging atmospheric Cerenkov Telescopes (IACTs) utilize large mirror areas to focus light onto fast photomultipliers, because the Cerenkov light emitted arrives at the ground-level within a few nanoseconds. Such telescopes can reconstruct the development of the shower as it penetrates the atmosphere, because the number of Cerenkov photons scales with the number of relativistic charged particles in the shower,

KASCADE made precise composition measurements using an ensemble of indirect techniques (Antoni et al., 2005). The techniques include scintillators to measure the lateral distribution of muons and electrons, a large central detector containing ionization chambers, a calorimeter, wire proportional chambers, streamer tubes and triggering scintillators. Their results strongly depend on the hadronic interaction model used to simulate the development of the air showers. Furthermore, elemental charge resolution is unachievable with techniques that measure χ_{max}, as they can only reconstruct charges with a resolution of $\Delta Z/Z \sim \ln(A)$ at best.

2.4 Direct Cerenkov Light

Kieda et al. (2001) proposed a new technique for measuring the composition of cosmic rays with ground-based imaging telescopes. The direct Cerenkov (DC) technique aims to achieve the charge resolution available to balloons and satellites with the effective area of ground-based telescopes by collecting the Cerenkov light initiated by the primary particle. Sitte (1965) first suggested that balloon experiments could extend to energies $> 10^{14}$ eV by flying two Cerenkov counters in coincidence above the altitude at which the air showers begin ($\sim$40 km). The idea was further developed by Gough (1976), culminating in the detection of 6 iron nuclei during a short balloon flight with energies $> 10^{14}$ eV by Sood (1983).

The number of radiated photons, N, per unit path length, χ, follows equation 2.5 (Frank & Tamm, 1937), which reduces to equation 2.6, the number of photons emitted along a path per unit bandwidth:

$$\frac{dN}{d\chi} = \frac{Z^2 e^2}{c^2} \int_{n^2(\omega)>1/\beta^2} (1 - \frac{1}{\beta^2 n^2(\omega)}) \omega d\omega \tag{2.5}$$

$$\frac{dN}{d\chi dE} \approx 370 Z^2 \sin\theta_C(E) \text{ eV}^{-1} \text{ cm}^{-1} \tag{2.6}$$

So the amount of light emitted by a cosmic ray scales with the Z^2, the square of charge of the primary particle. Heavier nuclei generate a substantial signal; an iron nucleus produce > 600 times that produced by a proton. Figure 2.4a shows the lateral distribution of Cerenkov photons produced by a 50-TeV iron nucleus interacting at 30 km. Greater than 10^5 DC photons concentrate in a ring close to the shower core, because the DC light is confined to a narrow Cerenkov angle. The DC light is therefore quite bright and confined to a narrow range of distances from the shower core.

The index of refraction decreases with increasing altitude due to the exponentially decreasing density of the atmosphere (starting from the top of the atmosphere) according to:

$$n = 1 + \delta \exp -h/h_0 \tag{2.7}$$

where $\delta \approx 300 \times 10^{-6}$ and the scale height, $h_0 = 8$ km.

Cerenkov radiation produced at the top of the atmosphere will therefore be more beamed than that emitted at the bottom of the atmosphere. As a example, a non-interacting 100 TeV iron nucleus would generate Cerenkov light at an angle of 0.16° at 35 km and 0.53° at 10 km. In reality, the iron nucleus would have produced a large particle air shower, so particles above the Cerenkov threshold at 10 km would radiate at slightly wider angles, as

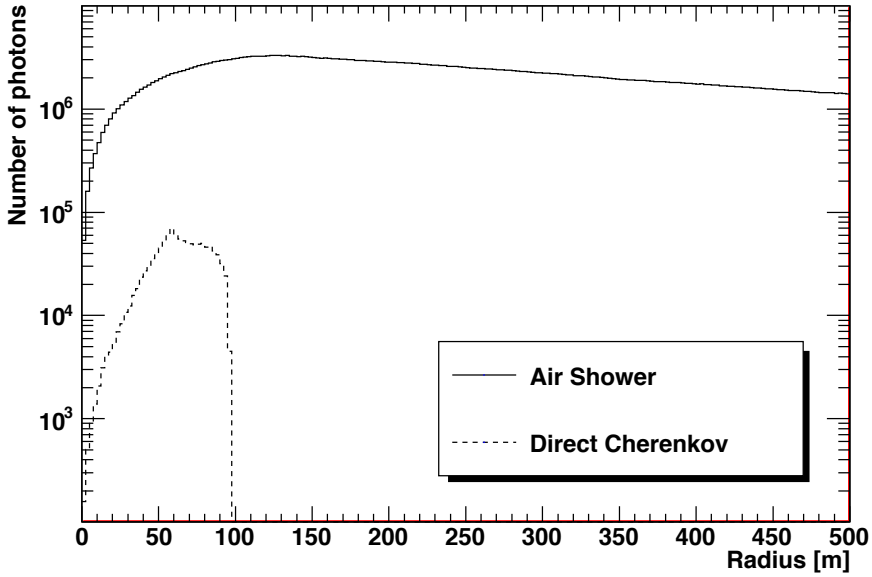

(a)

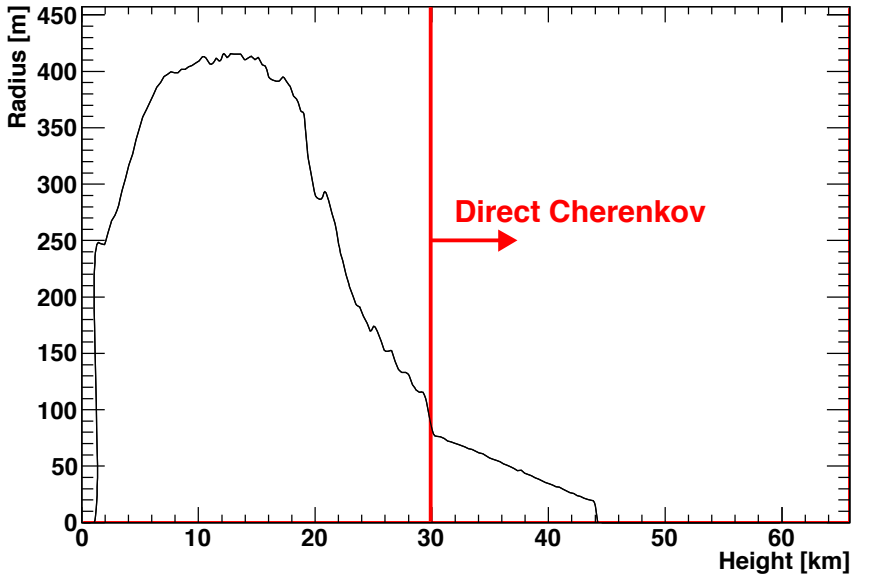

(b)

Figure 2.4: Simulated vertically-incident 50 TeV iron shower (a) number of photons emitted during the entire air shower (solid line) and above the first interaction height (30 km) (b) the mean radius from the shower core where a photon emitted at a certain height lands. The average Cerenkov angle, $\theta_C \sim R/H$.

shown in Figure 2.4b. Above the first interaction height, the Cerenkov angle changes slowly with the changing index of refraction. Below that height, it changes more rapidly. As the shower approaches the ground, the average impact parameter shrinks because the distance between the emission height and ground collapses.

Light produced by heavy nuclei is appreciable, but the difficulty lies in separating the Cerenkov light initiated by the primary particle from that from the extensive air shower. Most cosmic rays interact hadronically between 30 and 60 km above the ground. Above that height, the particle initiates DC light with a narrow Cerenkov angle, because the air at the top of the atmosphere is rarefied. Comparatively, light emitted in the extensive air shower will be emitted at broader angles with respect to the particle trajectory. The DC light will also arrive $\sim$2 ns after the extensive air shower, because it has to traverse more material than the photons produced lower in the atmosphere. The simulation shown in Figure 2.5 shows that by exploiting these two characteristics, the DC light can be identified.

An ideal detector with angular resolution a factor of 10 higher than the angular distance between the EAS light and the DC light and Giga-samples-per-second time sampling should achieve a charge resolution of $\frac{\Delta Z}{Z} \sim 5\%$ (Kieda et al., 2001). The H.E.S.S. collaboration, using an existing γ-ray telescope first detected direct Cerenkov light in 2005 achieving a charge resolution (17-25%) that improved with higher charges and energies. In a detailed analysis, they were unable to reconstruct the charge on an event-by-event basis, but extracted one of the most precise measurements of the differential iron spectrum on a statistical basis. Their spectrum, shown in Figure 7.1, extends to 200 TeV and agrees well with direct measurements from balloons and satellites. H.E.S.S. also compared the event reconstruction using simulations of two competing hadronic interaction models, QGSJET-II and SYBILL, seeing little disagreement in the energy and charge reconstruction (Aharonian et al., 2007b).

This thesis aims to measure the very-high-energy spectrum of iron nuclei using the direct Cerenkov technique. I begin by exploring new technologies meant to exploit the timing and

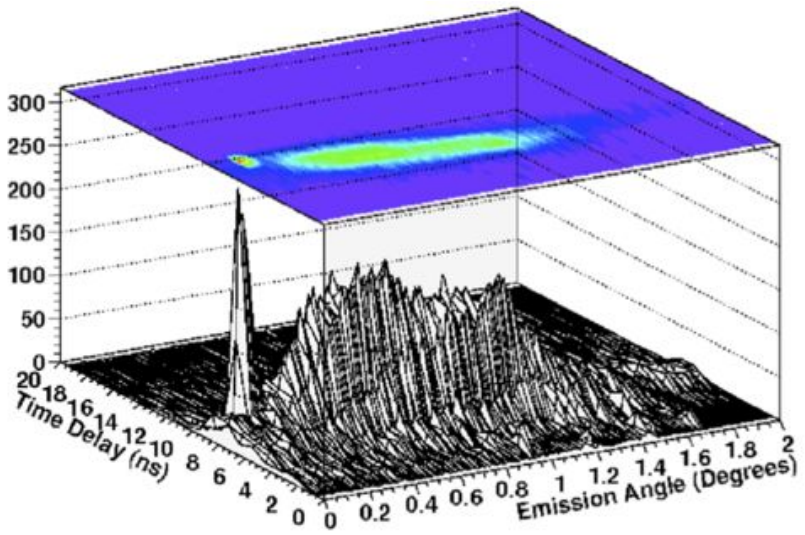

(a)

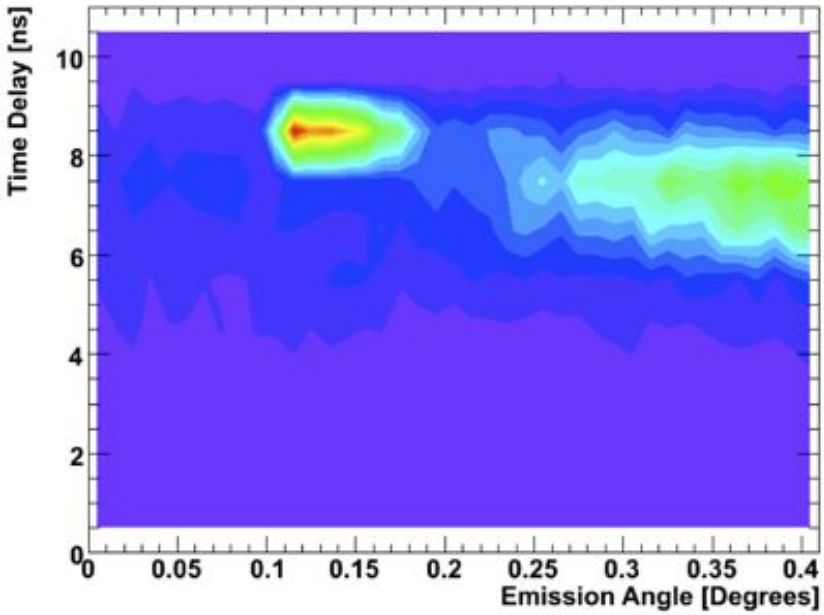

(b)

Figure 2.5: Photons emitted via Cerenkov radiation starting from the top of the atmosphere. The DC component is compact in both time and angular space (0.05° in angular extent and 1 ns in duration) and cleanly separated from the extensive air shower component by 2 ns and 0.2°.

angular separation of the DC and EAS light. Then I describe the detailed analysis used to extract iron nuclei from the background of the γ-ray observations of VERITAS.

CHAPTER 3

THE TRICE PROTOTYPE

The Track Imaging Cerenkov Experiment (TrICE), sited at Argonne National Laboratory, serves as a test bed for new technologies that exploit the timing and angular characteristics of DC events. In particular, it employs a novel optical trigger, described in 3.2, and a camera composed of multi-anode photomultiplier tubes (MAPMTs) to image cosmic-ray events in both high- and low-resolution modes. Thus, the primary objective was engineering a test facility for camera technology and the secondary objective was to act as a pathfinder for the discovery of DC light.

3.1 Motivation

As discussed in 2.4, measuring the composition of cosmic rays using the DC method is critically dependent on a telescope's ability to distinguish air shower light from light initiated by the primary. The DC signal is compact in both time and angular space, while the extensive air shower is more broad, both because the air shower light is emitted at a wide range of heights and because the air is rarefied at the top of the atmosphere. A telescope that makes use of the timing and angular separation between the two signals will be able to measure the species of the primary particle to high energy, provided that it has enough effective area to account for the diminishing flux at higher energies.

As an example, consider a 50 TeV vertically-incident iron nucleus that interacts 25 km above the observation level, as shown in Figure 3.3. When an instrument similar to VERITAS images it, the DC signal is easily visible in the camera plane and concentrated into one phototube, towards the front of the shower. However, the timing separation ($\sim$2 ns) is ambiguous because of the non-isochronous mirrors, and while the DC signal is visible, it is likely contaminated by air shower light because the angular separation between the DC light

Figure 3.1: The completed TrICE telescope with the baffle and electronics rack in the center of the telescope. The planar mirror and Fresnel lens are placed 3 m above the optical axis of the 4-m focal length spherical mirrors, on top of motor mounts allowing for precision focusing of the secondary mirror. Photo credit: Bob Wagner and Liz Hays, used with permission.

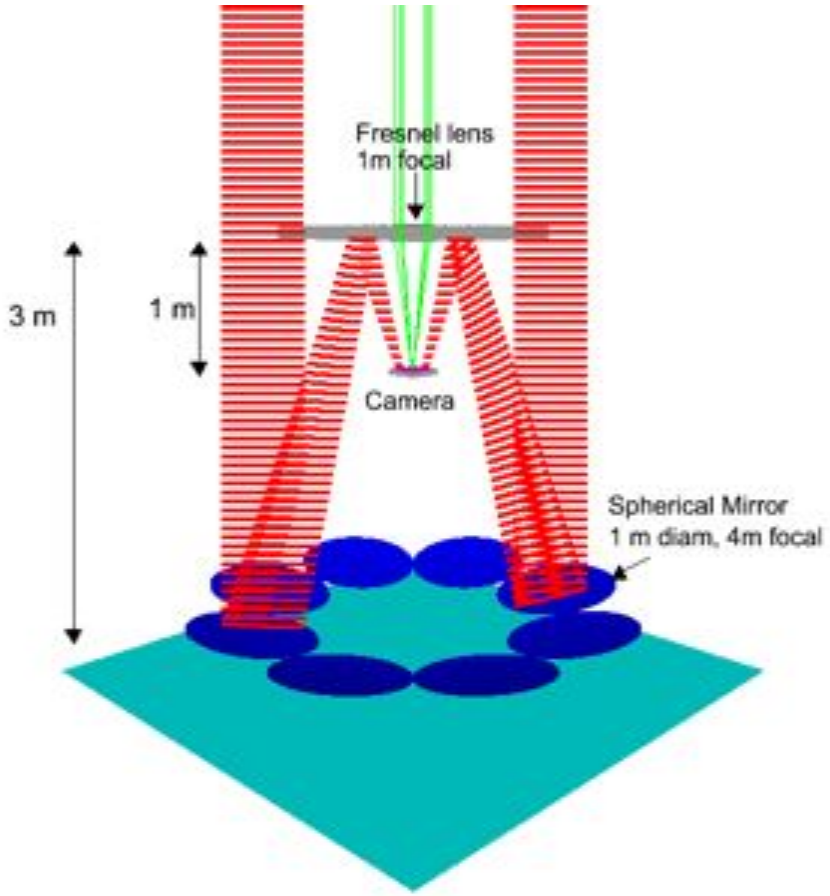

Figure 3.2: A ray-traced simulation of TrICE. Collimated light impacting the spherical mirrors, shown in red, are reflected onto the camera plane by the planar mirror, while those impacting the Fresnel lens, shown in green, are focused directly onto the camera plane

and the end of the shower, 0.2°, is only slightly larger than the 0.15° viewing angle of a pixel PMT. The TrICE telescope, with its improved angular resolution of 0.086°, however, would image the DC light in multiple pixels and enhance the time separation between the two signals using the optics shown in Figure 3.2.

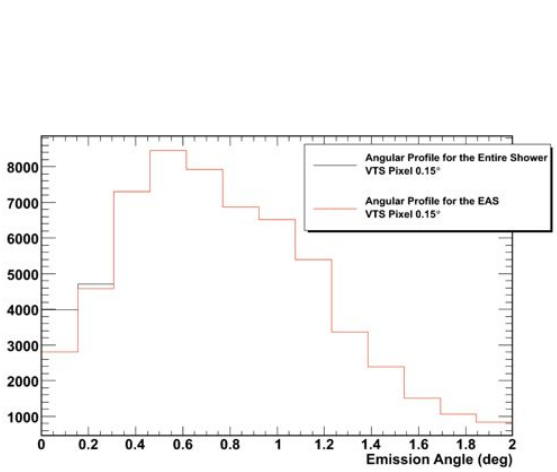

(a) IACT Angular Projection

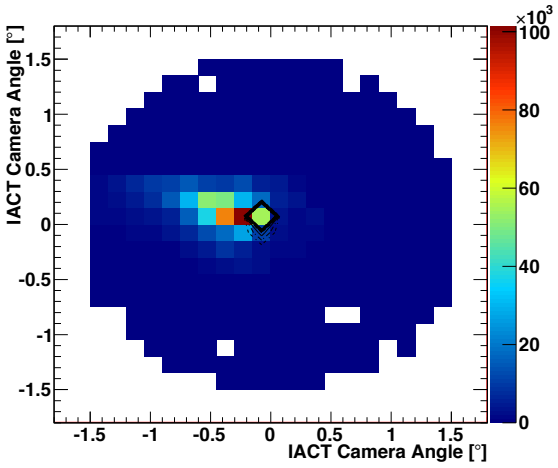

(b) IACT Camera

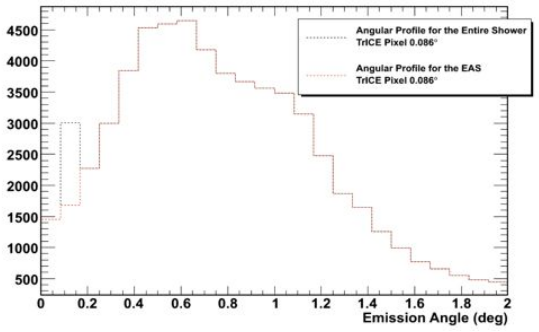

(c) TrICE Angular Projection

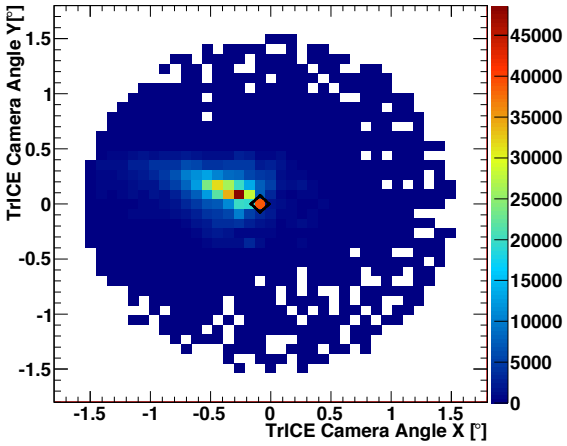

(d) TrICE Camera

Figure 3.3: A comparison of the ability for a telescope with angular resolution comparable to a typical IACT (0.15°, top) and TrICE (0.086°, bottom) to cleanly separate light from the primary and light from the EAS.

3.2 Optical Design

TrICE employs a specialized optical design, shown in Figure 3.2, to provide an optical trigger through one optical path and high-resolution imaging through a second. A Fresnel lens mounted directly above the camera plane enables a trigger signal that precedes a delayed and magnified image of the shower. Eight spherical mirrors are arranged on a square perimeter around the base of the telescope. They focus the high-resolution image onto the camera via a secondary planar mirror that also serves as a frame for the Fresnel lens.

TrICE features a primary mirror area of 6.4 m^2 and a 1.5° field-of-view, with eight 1-m spherical mirrors with focal lengths of 4 m. The 3.7° wide field-of-view of the Fresnel lens collects light from a wider angle than the mirrors and the difference in magnification between these two systems is ∼4x. The light from the air shower imaged by the coarse-grained optics of the Fresnel lens trigger the system, while the light from the mirrors, which comes from both the air shower and the primary particle, arrives nanoseconds later, because of the longer optical path length inherent to the mirror system. Using the Fresnel lens as an early trigger allows TrICE to first get a wide-field view of the air shower and later get a focused image of the shower and the DC light. Since the imaged light arrives 10 ns after the trigger light and the digitization time is 18.8 ns[1], the best candidate events to evaluate the performance of the Fresnel lens as a trigger include an early diffuse shower image from the Fresnel lens followed by a high-resolution air shower image with a DC peak.

Four mirrors were mounted in the grid using a silicone adhesive to make the planar mirror surrounding the Fresnel lens. Concern arose as to whether the mirrors were flat with respect to one another and to the ground. First, micrometer measurements were taken around the edges of the mirrors. Next, a three-dimensional map of the mirrored surface was created using a retractable arm which recorded the three-dimensional spatial coordinates of the

1. The data acquisition system digitizes the data from the MAPMT at 53 MSPS, as discussed in Section 3.3.

mirror with respect to a well-defined origin. The map is shown in Figure 3.4. Overall, the lowest point recorded was 0.208 mm deviant from the average value. The highest point was -0.123 mm away from the average. The total difference from the minimum to the maximum is 0.331 mm. Assuming a tolerance of 0.02°, this value is acceptable.

Each spherical mirror, shown in Figure 3.5, is mounted on 50.8 cm high pedestals to ensure that both the Fresnel lens and mirror system could be focused onto the camera. Lab tests determined the radii of curvature of all of the spherical mirrors to be within 0.64 cm of 7.945 m.

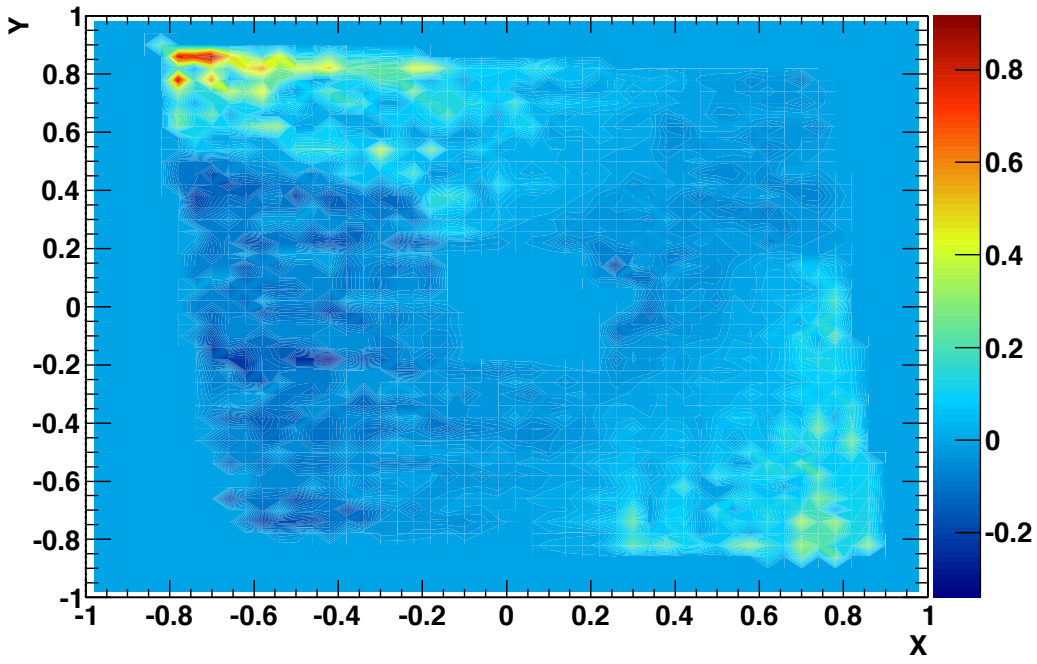

Figure 3.4: The deviations from the average thickness of the planar mirrors. The z-axis values are normalized to the average thickness value to accentuate the deviations therefrom. The highest point (the NE corner) corresponds to the edge where a gap is visible between the honeycomb surface and the mirror.

3.2.1 Night Sky Background

Working with the high level of night-sky background at the TrICE site proved to be one of the most challenging technological requirements. Using a baffle constructed around a single MAPMT showed that the anode current on the phototube without Cerenkov light (i.e., the night sky background rate NSB) was 1 μA per pixel. So the the approximate flux is $\sim 10^{13}$ photons m^2 s^{-1} sr^{-1}, implying that the total NSB rate for the complete telescope would be approximately 10^{11} photons per second. Note that this NSB flux is ten times that at the site of VERITAS, but that VERITAS has in excess of ten times the mirror area of TrICE.

3.2.2 Mirror alignment system

Typically air Cerenkov telescopes use stars to align the mirrors with an object placed at infinity. However, few stars of the necessary magnitude ($\sim$2 per year due to the NSB rate) pass over the fixed field-of-view of TrICE, which means that the mirrors must be placed in relative alignment. A custom motor-control system was designed to ensure that alignment could be done rapidly. The alignment system, shown schematically in Figure 3.6 and in Figure 3.5, allowed all of the spherical mirrors to be controlled simultaneously. Commands given through a graphical user interface are sent through TTL lines to a mirror control module which drives the two actuators on each mirror. Hall effect limit switches prevent the mirrors from moving past their safe range. The planar mirror is also controlled by four actuators that move up and down simultaneously when given commands from the mirror alignment system.

3.2.3 Point-Spread Function

Relative alignment of the spherical mirrors was achieved by fixing a white LED, of diameter 0.56 cm, $\sim$11m above the ground, such that the light would be focused $\sim$40cm above the

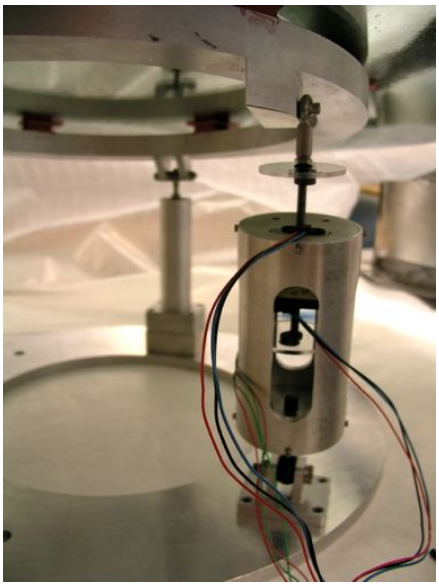

(a)

(b)

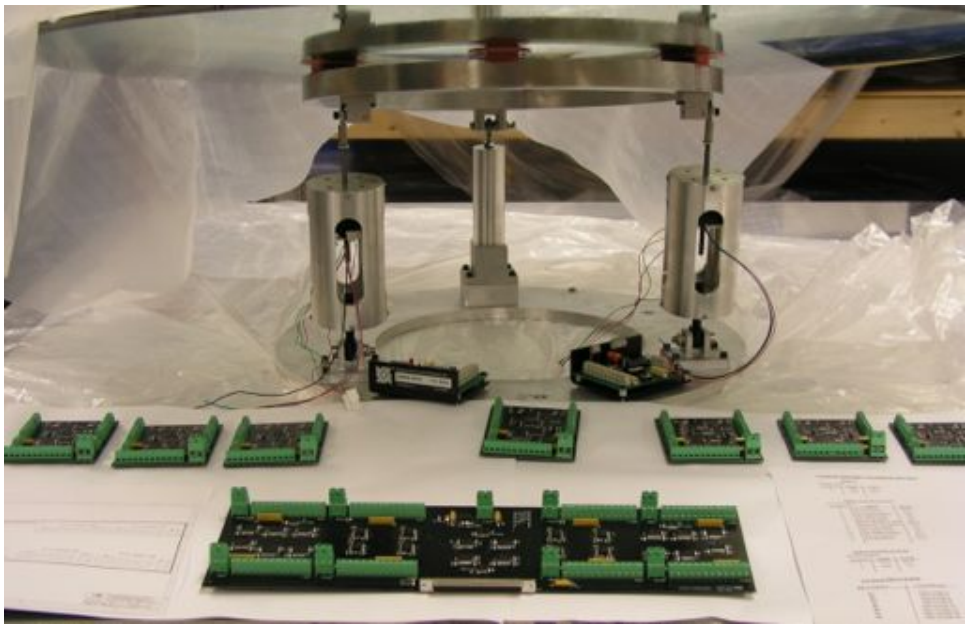

(c)

Figure 3.5: Two actuators remotely control the pitch angle of each spherical mirror of TrICE, pivoting on the third supporting beam. The mirrors were mounted on 50.8 cm heigh pedestals and surrounded by black cylinders with lids for protection. The actuators are controlled individually by chopper drives and together by a single mirror interface board. Precision Hall Effect limit switches engage when a magnet mounted on a wheel comes within 1 mm of the sensor. The entire mirror system is controlled remotely by a mirror interface board. Photos reproduced with the permission of Gary Kelderhouseand Richard Northrop.

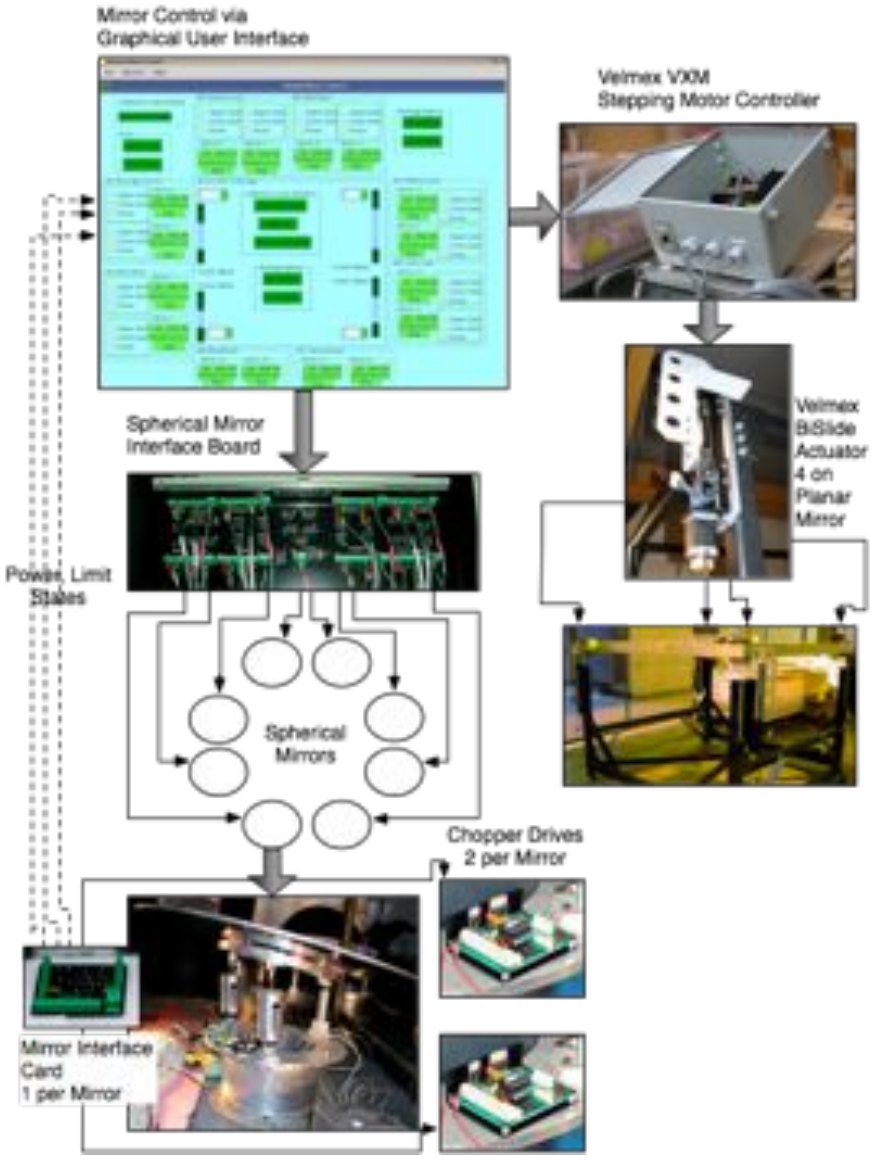

Figure 3.6: The alignment system for the spherical mirrors on the TrICE prototype. Photos reproduced with the permission of Gary Kelderhouse and Richard Northrop.

ground. The LED was first aligned with a laser placed in the center of the telescope on the ground and next with the light collected by the Fresnel lens. Then using a Starlight Xpress SXV-M7 CCD camera to record and analyze the point-spread function (PSF) at the height of the focal point, the images from the mirrors were aligned to one another. This process was performed iteratively, because the focal plane shares space with the data acquisition system. Thus, four mirrors were aligned simultaneously, repeating the procedure until all combinations of mirrors were aligned to each other. The intensity of light at the focal plane had a 90% enclosure region of diameter 0.6 cm, as shown in Figure 3.7. Deconvolution of the intensity function with the inherent width of the LED suggests a point-spread function of 2.2 mm which is smaller than the MAPMT camera pixel width of 6 mm.

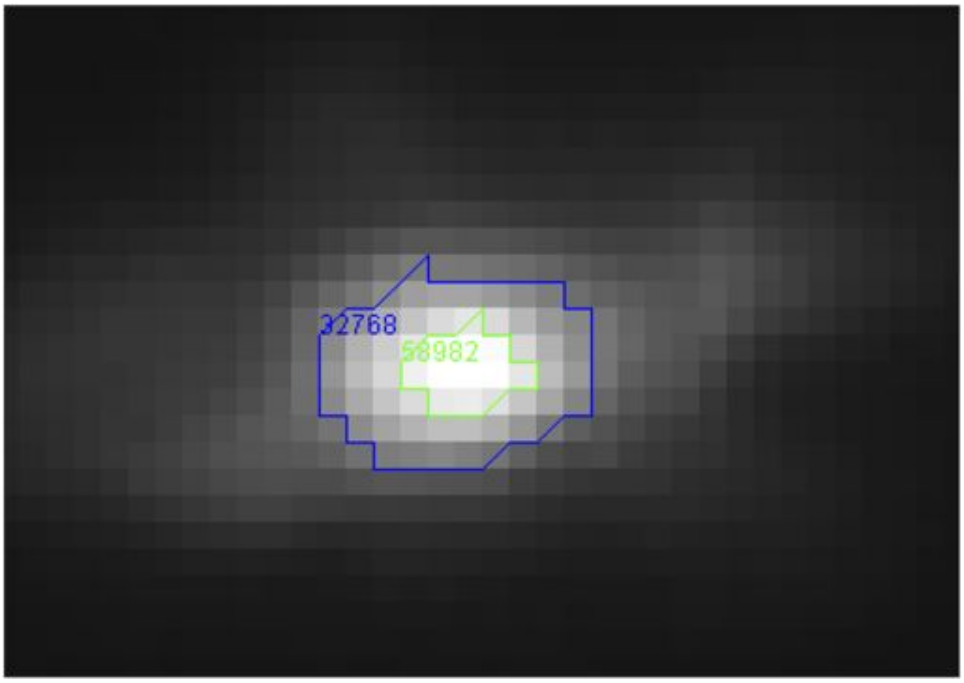

Figure 3.7: Image of 0.56 cm diameter white LED fixed ∼11m above the optical plane that suggests a point-spread function of 2.2 mm. Photo taken by the author.

3.3 Multi-Anode Photomultiplier Camera and Data Acquisition

The TrICE camera consists of 16-channel Hamamatsu R8900 multi-anode photomultiplier tubes (MAPMTs) and is shown in Figure 3.8 (Byrum et al., 2008). The phototubes were selected for their small detector size, good gain stability under high currents, low cross-talk among adjacent pixels, good single-photoelectron characteristics and extensive use in high-energy physics experiments (Skwarnicki, 2005).

The MAPMTs were tested using a custom-built dark box and found to have 2-3% crosstalk among adjacent pixels and linearity over a dynamic range from 1–100 photoelectrons, deviating by $\sim 5\%$ from 200–500 photoelectrons. A constant light source was used to test the response of the camera under noise conditions comparable to the NSB in order to select the optimal operating voltage for the camera. Gain variation across the camera was limited to a factor of 2 to 3, and the camera maintained stable gains from night to night, as shown in Figure 3.9.

Two VME crates hold modules designed for the digitization of MAPMT signals and the buffering of data record the signals from the PMTs. Analog signals from a 16-channel MAPMT travel to a corresponding 16-channel module housed in the front-end VME crate, where 53 MSPS charge integrating encoders, or QIEs, integrate and digitize the current signals. Sixteen MAPMTs were installed for a total of 256 pixels each having an angular width of 0.086°. They are read out using a customized ASIC that digitizes continuously at 53 MHz over a dynamic range of 16 bits (Cundiff et al., 2006). Upon receiving a trigger, the digitized data are transferred to a separate "back-end" VME crate.

The dynode signals from the 4 central MAPMTs of the camera are used to trigger the front-end electronics. A trigger is generated by the coincidence of at least two MAPMT dynode signals above a programmable threshold. An approximate analysis threshold requires a minimum of approximately 15 photoelectrons summed over an MAPMT. In addition to

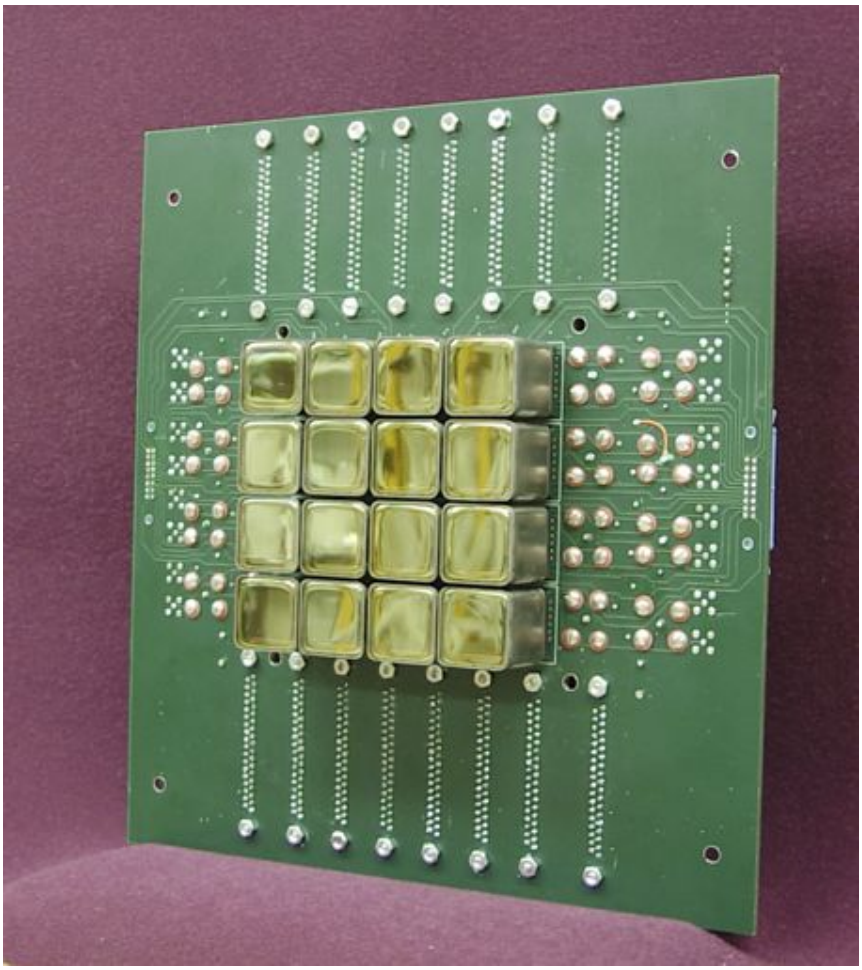

Figure 3.8: The multi-anode photomultiplier tube camera installed on TrICE. Photo credit: Bob Wagner, reproduced with permission.

the dynode-based trigger, the front-end electronics also accepts an external trigger signal. This mode is run separately from normal observations and is primarily used for measuring the effects of the night sky photon background on integrated charge values.

The back-end VME data acquisition consists of 9U VME modules designed to receive and buffer the digitized signals until they can be transferred to disk. A VMIVME 7766 single board computer running Linux controls the programming of the front-end and back-end VME modules and also handles the transfer and storage of buffered data. The back-end modules employ two memory buffers that switch on 20 ms interrupts. The VME CPU transfers data from the inactive buffer to disk while the active buffer fills with incoming data from the front-end modules.

3.3.1 Simulated NSB Gain Tests

Regular flat-fielding tests were performed to ensure that the camera maintained stable gains throughout the observing season. Using a diffuse light source mounted above the camera, the camera's response to a continuous light source can be simulated. Figure 3.9 shows that the distributions of individual gains are consistent from month to month and vary by $< 23\%$ across the camera. There is some structure in the channel gains for individual photomultiplier tubes, but these remain constant throughout the observations.

3.4 High-Resolution Cosmic-Ray Air Showers

Observations were made using the calibrated TrICE telescope from January through March, 2007. Standard operating thresholds ranged between 1000 mV and 1500 mV, giving rates between 40 and 60 Hz depending on the weather and the number of mirrors included in the observations. Thresholds were selected on a nightly basis to account for the changing weather conditions. Observations where only the Fresnel lens or one spherical mirror is uncovered

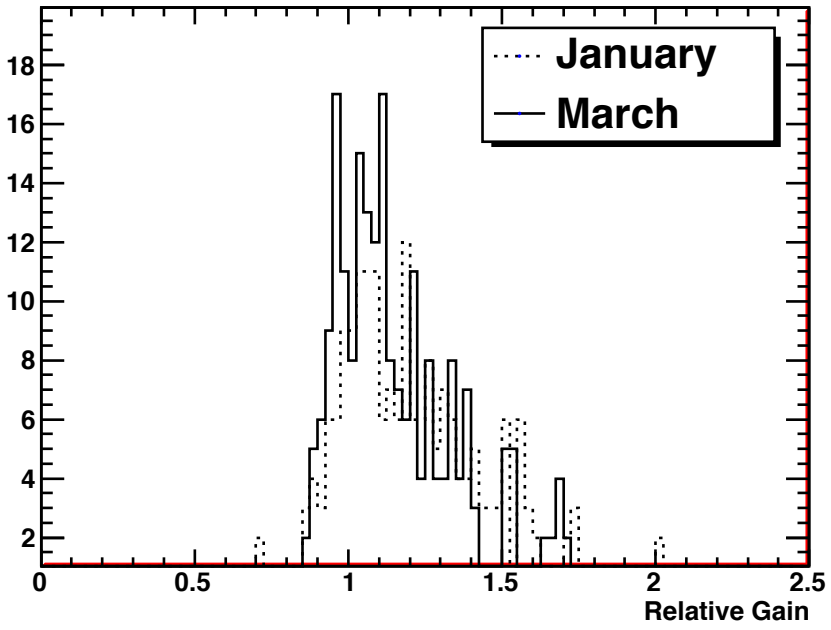

Figure 3.9: Relative channel gains as determined by flat-fielding the camera over the course of a season in 2007.

were used as diagnostic tools during regular observations.

The images of extensive air showers are among the highest resolution images ever recorded. Figure 3.10 shows two such events taken showing an extended shower with a peak slightly displaced from the center. Substructure in the air showers events are also visible. Note that the structure is smaller than the scale of one MAPMT, indicating that the camera is capable of measuring intensity differences for each channel.

The light from the air shower in the Figure 3.10b arrives in the second time slice (i.e., $>$ 18.8 ns) after a diffuse trigger that triggers the inner four photomultiplier tubes. Light imaged by the Fresnel lens should be more diffuse than that from the mirror system. This confirms that the Fresnel lens can be used as an optical trigger; however, a careful study of the conditions that would cause spurious triggers is necessary to proceed.

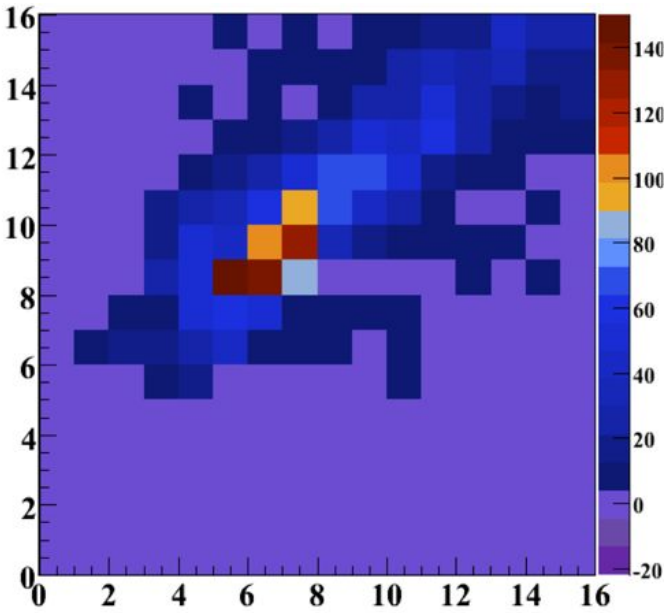

(a)

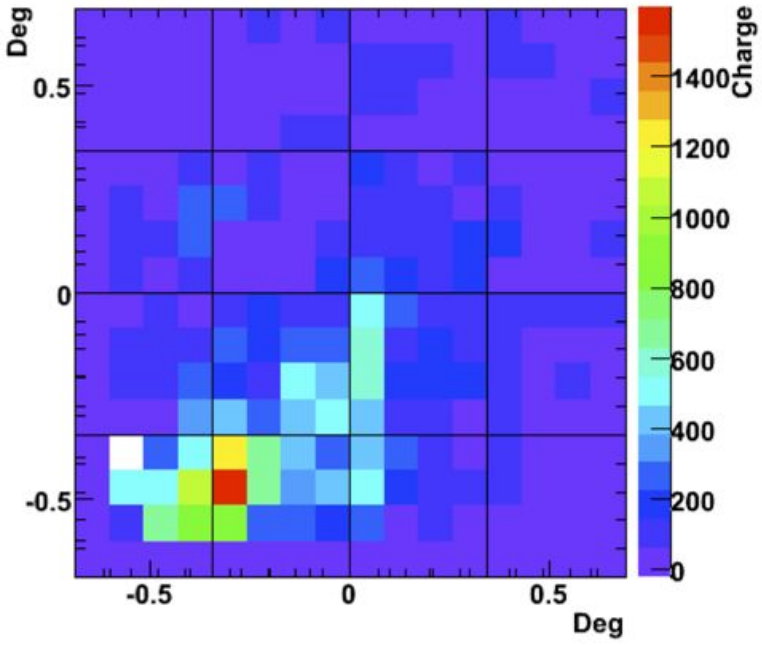

(b)

Figure 3.10: High-resolution shower images taken with the TrICE telescope, plotted as a function of channel number in (a) and camera angle in (b).

3.5 TrICE Data Analysis

Almost all of the signal in the TrICE data is contained in the first three analog-to-digital channels (ADCs), while the last ADC channel contains the pedestal information. The first three ADC channels for each pixel are summed to give the time-integrated image of each event. The electronic pedestal remains fairly constant at a value between 100 and 120 digital counts and is subtracted from every event. After flat-fielding with the lab-measured gain values for each MAPMT, the images are cleaned using a fixed threshold cut set at 5 p.e.s for pixels within the image and 2 p.e.s for pixels on the edges of the image.

The images are then fit to an ellipse (for reasons described Section 5.1) in using a function that finds the borders of an ellipse. A copy of the image – hereafter known as the ellipse map – sets image pixels to a constant value and the border pixels to a value between zero and one . If the point being tested in the fit is inside the ellipse, then the function returns a value of 1 and if it is outside the ellipse, then it returns a value of 0. On the edges, the fit function returns a value between zero and one to ensure that the fit converges. The final fit gives information about the size, shape and orientation of the image in the camera plane. The fit proceeds according to equations 3.1:

$$
\begin{aligned}
\frac{x^2}{l^2} + \frac{y^2}{w^2} &= 1 && \text{Equation of an ellipse} \\
x' &= x - x_0 && \text{Translation} \\
y' &= y - y_0 && \\
\begin{pmatrix} x'' \\ y'' \end{pmatrix} &= \begin{vmatrix} \cos(\phi) & \sin(\phi) \\ -\sin(\phi) & \cos(\phi) \end{vmatrix} \begin{pmatrix} x\prime \\ y\prime \end{pmatrix} && \text{Rotation} \\
\frac{x''^2}{l^2} + \frac{y''^2}{w^2} &= 1 && \text{Equation of the rotated ellipse}
\end{aligned}
\tag{3.1}
$$

The initial offsets, x_0 and y_0, are defined as the mean values along the x and y axes, respectively. The ϕ parameter defines the major axis of the ellipse and defined by the line passing through the edges of the ellipse map. The length, l, and width, w, set the scale of the ellipse along the major and minor axes. They are initially set to the integrals of the ellipse map along the line that runs through the center of the image at an angle of ϕ.

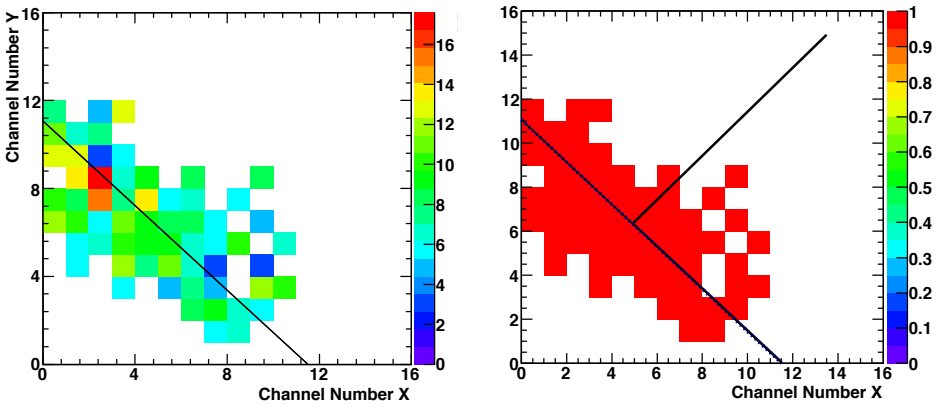

(a)

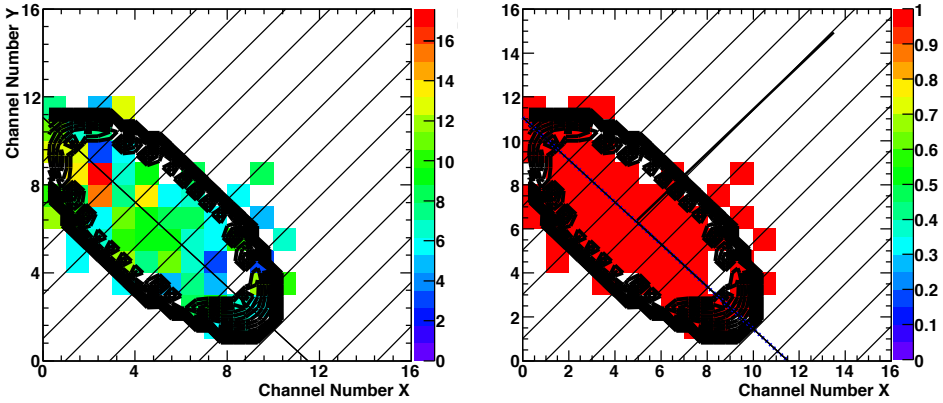

(b)

Figure 3.11: Cleaning and ellipse fitting of a TrICE event. The cleaned and gain-corrected image is shown in (a) and the ellipse fit and projection lines are shown in (b).

After the image ellipse is defined, the image can be projected into a one-dimensional plane along the major axis of the ellipse. If DC light is contained in the image, then it will arrive after the EAS light, and at an angle further away from the center of the ellipse. The

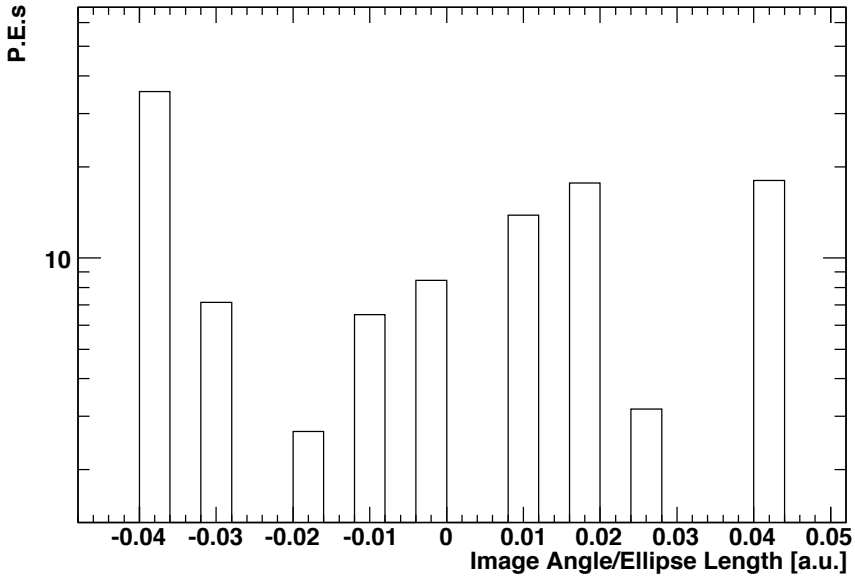

Figure 3.12: The image from Figure 3.11 projected onto the major axis of the ellipse and scaled by the ellipse length.

example event in Figure 3.11 shows the ellipse-fiting procedure and the projection onto the image axis of the event. The event can be projected onto the major axis of the ellipse as shown in Figure 3.11, where it can be seen that the front of the shower is bright.

After performing this image analysis over the course of a night and summing the profiles of the images scaled by their lengths, the underlying structure of the images emerge. As shown in Figure 3.13, the central peak in the image is substantial. There is a slight asymmetry in the images, and considerable deviation from a Gaussian profile.

3.6 Outlook

The TrICE telescope demonstrates that a MAPMT camera can be used in a cosmic-ray telescopes under substantial noise conditions with little variation in operating conditions. The technologies tested during the construction and operation of this prototype may be considered for use in the design of an observatory dedicated to cosmic-ray observations.

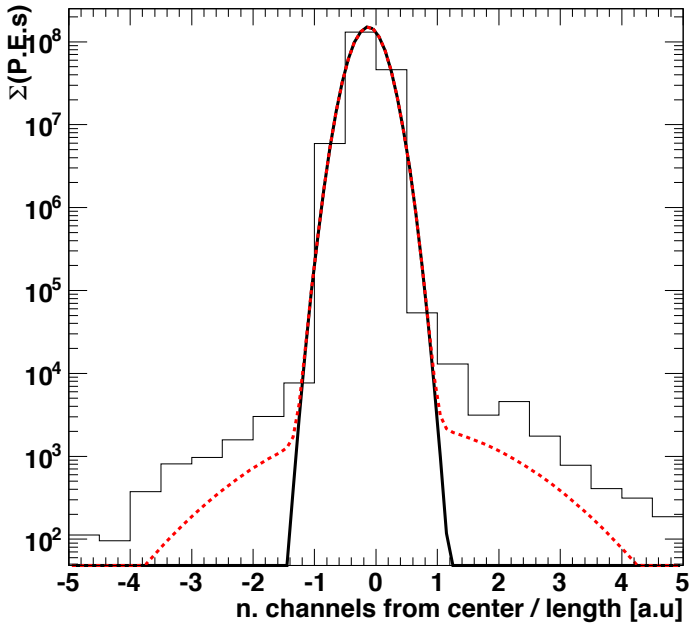

Figure 3.13: Image profiles scaled by their length and summed in angular bins.

The optical system provided both an optical trigger and the convenience of a fixed-mount design. Alignment of the novel optical system proves to be difficult when the telescope must be operated in weather conditions, but using a remotely-controlled alignment system and a fixed point-source, relative alignment of the mirrors has been shown to produce a point-spread function smaller than the MAPMT pixel size. Well-resolved images of the cosmic ray air showers were seen in the TrICE data, demonstrating the level of precision available to the next generation of γ-ray telescopes like AGIS and CTA that will use cameras with comparable angular resolution.

TrICE was built with the primary goal of testing new technologies and the secondary goal of discovering direct Cerenkov light by exploiting both the timing and angular characteristics of the DC signal. Unfortunately, the electronics used on TrICE integrate the light from most events into one ADC time slice. As work proceeded with TrICE, the H.E.S.S. collaboration first observed direct Cerenkov light using an atmospheric Cerenkov telescope designed for

observing very-high-energy γ-rays (Aharonian et al., 2007b), and VERITAS was nearing its final phase of construction. So it seemed appropriate to continue the search for direct Cerenkov events in the VERITAS data.

CHAPTER 4

VERY ENERGETIC RADIATION IMAGING ARRAY SYSTEM (VERITAS)

The Very Energetic Radiation Imaging Array System (VERITAS) is a four-telescope array dedicated to gamma-ray astronomy located in Southern Arizona (31.6747° N and 110.9527° W). It is currently the most sensitive ground-based very-high-energy gamma-ray telescope; it can detect a source at 5σ with a flux equivalent to 1% of Crab Nebula (the standard candle for VHE gamma-ray observations) in under 25 hours.

Figure 4.1: The VERITAS array located on Monte Hopkins in Southern Arizona during the 2007-2009 epoch. Photo credit: Kenn Gibbs and Steve Criswell.

4.1 Optical Design

The imaging atmosphere Cerenkov technique requires a large field-of-view in order to image the entire development of an air shower from the height of first interaction to the height of maximum development, as well as a large mirror area to enhance the light collection. In addition, the DC technique requires better than 0.5° field-of-view per pixel to be able to separate DC light from EAS light. VERITAS employs a Davies-Cotton design in which segmented mirrors are adjusted to correct for spherical aberration in the outer regions of the

dishes. Davies and Cotton originally designed this optical system for use in solar furnaces in 1957 (Davies & Cotton, 1957). The design was adopted by the gamma-ray astronomy community, because the atmospheric imaging technique requires large dishes with substantial focusing power. This culminated in the discovery of TeV gamma rays coming from the Crab Nebula in 1989 (Weekes et al., 1989). Incidentally, if the VERITAS mirrors were used as a solar concentrator, they would collect ~ 0.4 MW/m^2 under average conditions.[1]

It is straight-forward to calculate the aberration incurred by a spherical dish of similar dimensions as VERITAS. If you assume that the distance from the center of the dish is y and the radius of the curvature is R (24 m for VERITAS), the aberrations scale as $\sim \frac{y^3}{R^3}$. So the aberrations can become severe for a spherical mirror of radius 12 m. The misalignment is 1 m at the edge of the mirror. To correct for this, the mirror is segmented and its pointing direction is adjusted to account for the spherical aberrations. Ray-tracing simulations show that the off-axis aberrations incurred by a Davies-Cotton design are smaller than those from a parabolic mirror design (Lewis, 1990).

The main disadvantage to the Davies-Cotton design is the inherent time spread introduced by the reflector geometry. Because of the spherical design, photons incident close to the reflector's edge travel shorter distances than those near the center, and therefore, arrive at the camera plane earlier. Simulations show that the time spread introduced is 5 ns, with a rise-time of 1.7 ns (White, 2005).

Each VERITAS telescope employs 350 hexagonal mirror facets, shown in Figure 4.2, which measure 60.96 $\pm$ 0.3 cm along the straight edges (Roache et al., 2008). They have a radius of curvature of 24 m $\pm$ 1%, and therefore, a focal length of 12 m. Each facet has a mirror area of 0.322 m^2, giving a total mirror area of $\sim$ 110 m^2. Each telescope employs

1. The total concentration factor of a VERITAS reflector is the ratio of the mirror area to the camera area. For VERITAS, this would be 110 m^2/0.28 m^2 $\sim$ 400. Assuming that the average solar intensity is 1 kW/m^2 the total power is 0.4 MW/m^2.

Figure 4.2: The VERITAS mirror facets. Photo taken by the author.

a 12-m aperture with a 12-m focal length, generating fast optics with an f-number of one[2]. The speed of the optics generates an inherent time spread across the dish of 3-4ns, which is sufficiently smaller than the timescale of the showers. The mirrors are attached to the optical support structure (OSS) with triangular mounts, which allow for easy manual alignment.

Until May 2009, the mirrors were aligned using a fixed mount laser system placed 24 m away from the center of the mirror plane. By placing a point source at the $2f$ point, the mirrors are placed in relative alignment by adjusting the tension on the mounting bolts. Measurements of the point-spread function (PSF) at varying elevations are taken to assess the optical quality. After May 2009, a new alignment system was adopted in which the PSF's at different elevations are used to determine the level of misalignment. Following a description of the technique found in (Arqueros et al., 2005), a CCD camera was installed in the focal plane of the camera that imaged the mirrors as they imaged stars at different zenith angles. The intensity of the collimated light from the star should be uniform across the mirrors area, assuming that the mirrors are properly aligned. Therefore, the level of intensity of light from the point sources indicated the misalignment of each mirror. Figure 4.3 shows that this method improves the PSF by 22% such that 90% of the light from a point-source is contained within less than half of a pixel size. (McCann et al., 2009).

4.2 Camera

Each VERITAS telescope is equipped with a 499 pixel camera consisting of Photonis XP2970/02 photomultiplier tubes (PMTs) of diameter 2.86 cm. The PMTs were selected for their UV sensitivity, a critical characteristic for observing Cerenkov radiation. They achieve a quantum efficiency of 25% at a wavelength of 320 nm. Each cylindrical phototube consists of a

2. The speed of the optics is a dimensionless quantity indicating the light intensity. In photography terms, the ratio of the aperture (in this case the mirror diameter) to the focal length determines the amount of time necessary to open the shutter to expose the film. Smaller f-numbers therefore indicate more intense light collection efficiency.

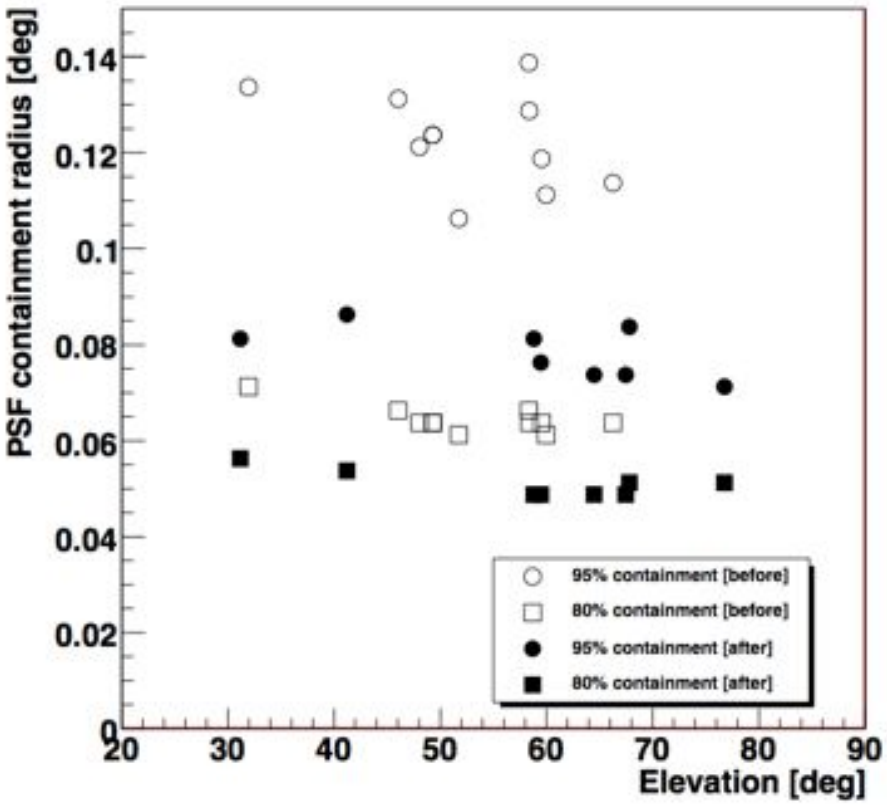

Figure 4.3: The VERITAS point-spread function as a function of elevation for the two mirror alignment systems.

bi-alkali photocathode on UV glass with 10 gain stages (VERITAS Collaboration: T. Nagai et al., 2007).

Housed within the bases of the PMTs are custom-made preamplifiers. The signal is amplified by a factor of 6.6 before traveling the 140 ft to an electronics trailer situated close to each telescope. The signals travel along 75 ohm coaxial cables (RG-579) selected for their low probability of breaking and high signal-to-noise (Kieda et al., 2003).

Light concentrators mounted on top of the PMTs simultaneously reduce the dead space between pixels and reject extraneous light from the night-sky-background. The light cones are made of molded plastic with an evaporated aluminum coating on the inner surface. They have hexagonal entrance windows to permit closer packing and evolve into Winston cone shapes at the base to permit more light. With this design, they achieve $> 85\%$ reflectivity at 260 nm (VERITAS Collaboration: T. Nagai et al., 2007).

4.3 Trigger System

VERITAS operates with a 3-level trigger system: a camera level trigger, a pattern trigger and an array trigger. The data collection rates can be reduced from a few hundred Hertz, at the single telescope level, to $\sim$150-200 Hz at the array level, depending on the elevation and source being observed.

Starlight from the night-sky background as well as Cerenkov radiation from secondary muons created close to the telescope contributes substantially to a single telescope's trigger rate. Noise from the night-sky background, which is typically $\sim$2-0.8 pe/ns (Vassiliev et al., 2003) can be eliminated using a threshold cut on the charge accumulated in each pixel. Triggers due to bright stars, or other sources of bright, uncorrelated noise in the camera can be reduced by using a topological trigger which only passes events that have patterns of pixels firing at the same time.

The output from each photomultiplier is fed into a constant-fraction discriminator (CFD),

which when paired with a feedback loop dependent on the CFD frequency, can reduce the coincidence resolving time between adjacent pixels to ∼5 ns (Vassiliev et al., 2003). During normal operation, the thresholds set on each CFD to produce a level-one trigger are set to 50 mV and, during moonlight observations, to 70 mV. Reducing the time required to identify a pattern in the second-level trigger is critical to reducing the energy threshold, because it reduces the instrument's dead time due to noise triggers (Bradbury, 1999). Second-level triggers are generated when programmable patterns are found in the camera. In order to pass the level-two trigger, three adjacent pixels must produce level-one triggers.

Stereoscopic imaging also helps reduce triggers due to muons from hadronic showers. Cosmic-ray air showers produce penetrating muons. Those produced at ∼4 km above the ground produce Cerenkov rings in only one telescope. By requiring that more than one telescope gets triggered by an event, these events can be removed from the sample. The third trigger level, therefore, is the array-level trigger which communicates with the pattern triggers on each telescope via ECL signals transmitted through optical fibers by custom-built Digital Asynchronous Transceiver modules (DATs). The array trigger comprises a programmable delay module (PDM) and a SubArray Trigger (SAT) board. Differences in the arrival times of the pattern trigger signals from each telescope are caused by differing cable lengths and differing arrival times of the Cerenkov telescopes at each telescope. The first delay can be corrected for exactly, but the second must be adjusted as the telescopes move through the sky (Weinstein, 2008). Level-three triggers are generated when at least two out of four telescopes produce a level-two trigger.

Scans in triggering threshold, or bias curves, are performed regularly to assess the performance of the array (shown in Figure 4.4). At low CFD thresholds (<30 mV), the triggers are dominated by the night-sky background, while at high thresholds (> 70 mV), they are generated by triggers from cosmic-ray air showers. The optimal threshold for observations is just above the change in slope of this curve, because employing lower thresholds permits

triggers from lower-energy gamma rays, but if the threshold is too low, the exposure will be reduced by an increase in dead time.

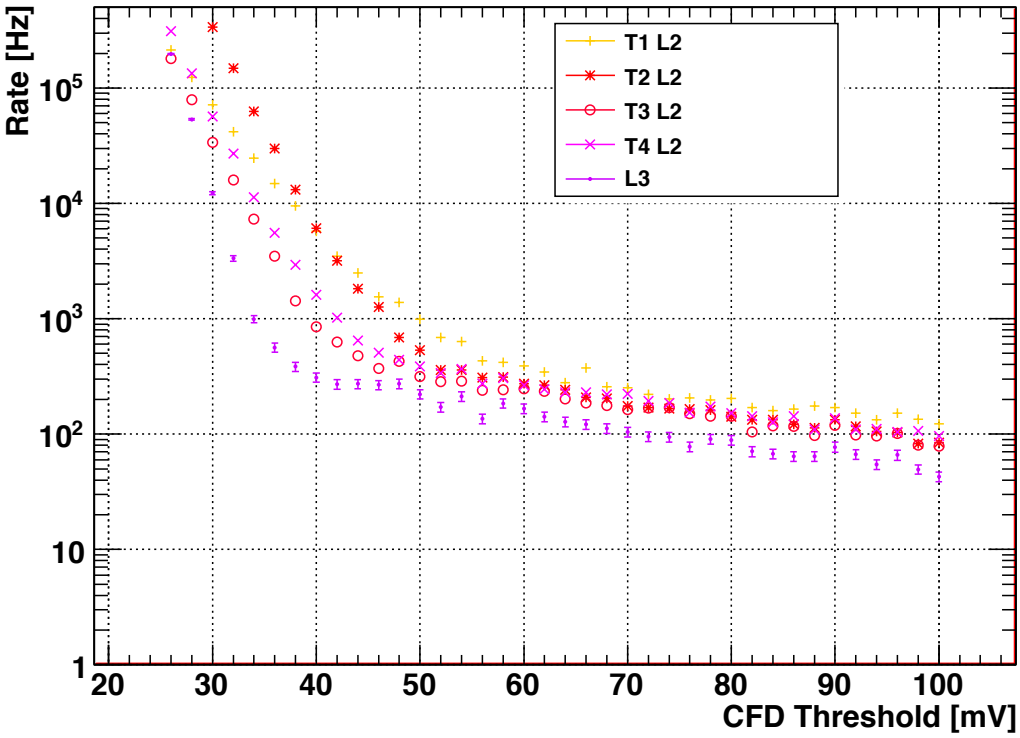

Figure 4.4: Bias curves from June, 11, 2008 demonstrating the use of the 50 mV CFD threshold, 3/3 pattern trigger and 2/4 array-level trigger.

4.4 Data Acquisition

VERITAS records events using a flash analog-to-digital converter (FADC) with a sampling rate of 500 Mega Samples Per Second (MSPS). The data stream is buffered at a depth of 32-bits and copied into one high-gain and one low-gain channel, one of which is read out by the FADC depending on whether the pulse saturates the high-gain channel.

Figure 4.5 shows how the data acquisition systems respond to triggers. While the data is being buffered in the FADCs, a decision is made by the L3 system as to whether the

event receives an array-level trigger. If an event passes the 3-level trigger, then each event from every telescope is read out and compiled into a single event with a dead-time of 10%, employing a BUSY signal while the data are read out and sent to the central computing trailer. The "harvester" process compiles the data from all telescopes into one single event which is then stored in the data stream.

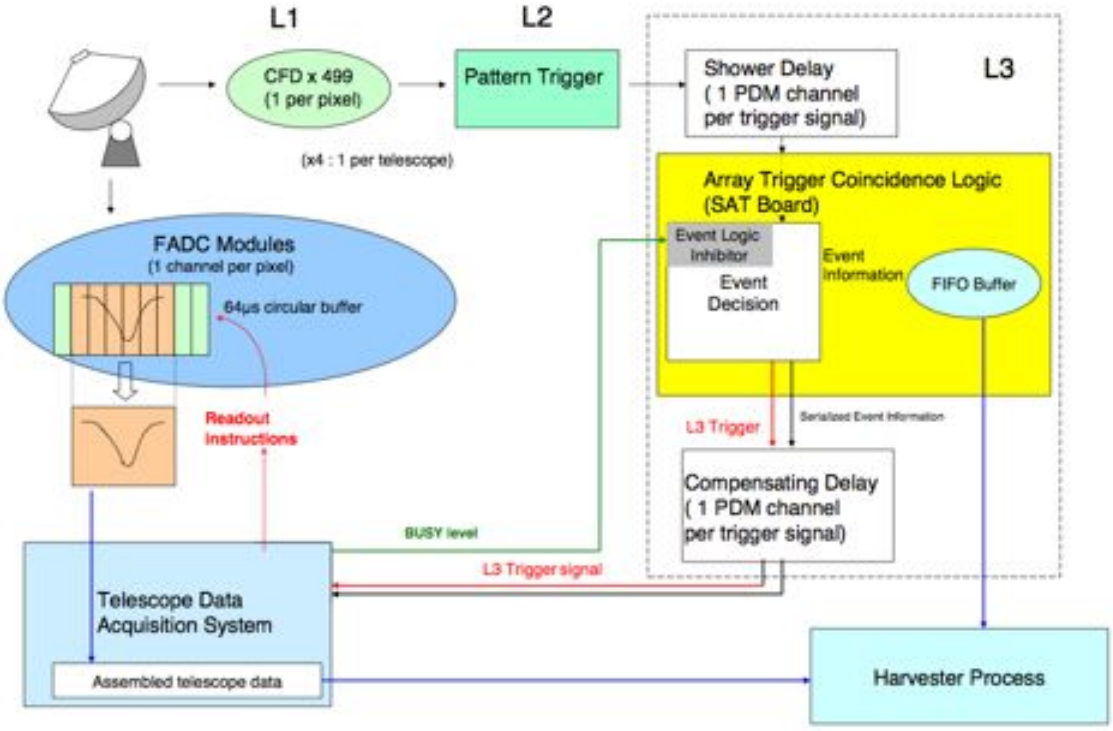

Figure 4.5: Schematic of the interplay between the data acquisition and trigger system on VERITAS from Weinstein (2008).

CHAPTER 5

DIRECT CERENKOV RADIATION AS OBSERVED IN VERITAS

This chapter describes the detailed analysis used to analyze each cosmic-ray event imaged by VERITAS. In particular, the method used to separate DC light from the air shower light using the angular and timing characteristics of each image is described. A large ensemble of simulations are generated to understand the response of the VERITAS array to DC events and the background events from proton- and helium-induced air showers. Cuts used to reject the air showers from low-mass nuclei are also described.

5.1 Air Shower Parameterization

A pulse generator injects triggers into the L3 trigger system on VERITAS at a rate of 1 Hz to collect signals for all of the FADC channels when no Cerenkov pulse is present. The average value of these signals is the mean pedestal, and their root-mean-squared variation σ_{peds}, provide a measure of the night sky background. Prior to parameterizing the air shower image, the pedestal for a given FADC channel is subtracted. The cameras are also flat-fielded on a nightly basis using a dye laser that runs at 10 Hz and provides its own trigger. The laser illuminates the camera with the same overall intensity, permitting the calculation of relative gains among the photomultiplier tubes. The pulse from each FADC channel can be corrected for the average gain on a nightly basis.

A double-pass algorithm eliminates channels that do not contribute to the air shower image. The first pass uses a wide integration window (24 ns) that searches for the time, t_0, when the Cerenkov pulse reaches one-half of its maximum. It also parameterizes the images and looks for a gradient in the timing of each image to refine the estimate of t_0. The second pass uses a narrower window (14 ns) to compute the integrated charge on the

FADC channel. The charges are then compared with the variations in the pedestal values. The pedestal values vary across the sky depending on how bright the portion of the sky is within the field-of-view. Diffuse optical light, bright stars ($>$ 4-th magnitude) and weather conditions generate fluctuations in the noise seen at each PMT. The images are cleaned of pixels that are dominated by noise by setting analysis threshold that depend on the root-mean-square of the pedestal values, σ_{peds}. A channel passes the cleaning thresholds if the integrated charge is greater that $5\sigma_{peds}$ or if it is greater than $2.5\sigma_{peds}$ and neighboring an image pixel (Holder et al., 2006).

After the events are cleaned, they are passed through a moment analysis algorithm that represents the image as an ellipse. A series of parameters defined by Hillas, hereafter known as the Hillas parameters, define the two-dimensional structure of the image and were originally developed to distinguish γ-rays from hadronic showers. The "width" and "length" parameters are the root-mean-square variations along the lateral and longitudinal development of the shower. The "dist" parameter measures the angular distance from the center of the image to the field-of-view of the camera. α is the angle between the major axis of the ellipse and the center of the field-of-view. The arrival direction of the incoming particle lies along the image axis (Hillas, 1996).

Parameters that depend on the total integrated charge are often given in units of the digital counts (d.c.) in a FADC channel. Measurements of the response of the telescopes to single photoelectrons (p.e.s) using atmospheric muons calibrate the ratio of p.e.s to digital counts to ~ 5 (Humensky, 2005).

5.1.1 Shower Core and Arrival Direction Reconstruction

Stereoscopic parameters relate the images in different cameras to each other and can resolve the uncertainty in the arrival directions of the incoming cosmic rays. Because they are viewing the same region of the sky – but often different portions of the shower – the camera

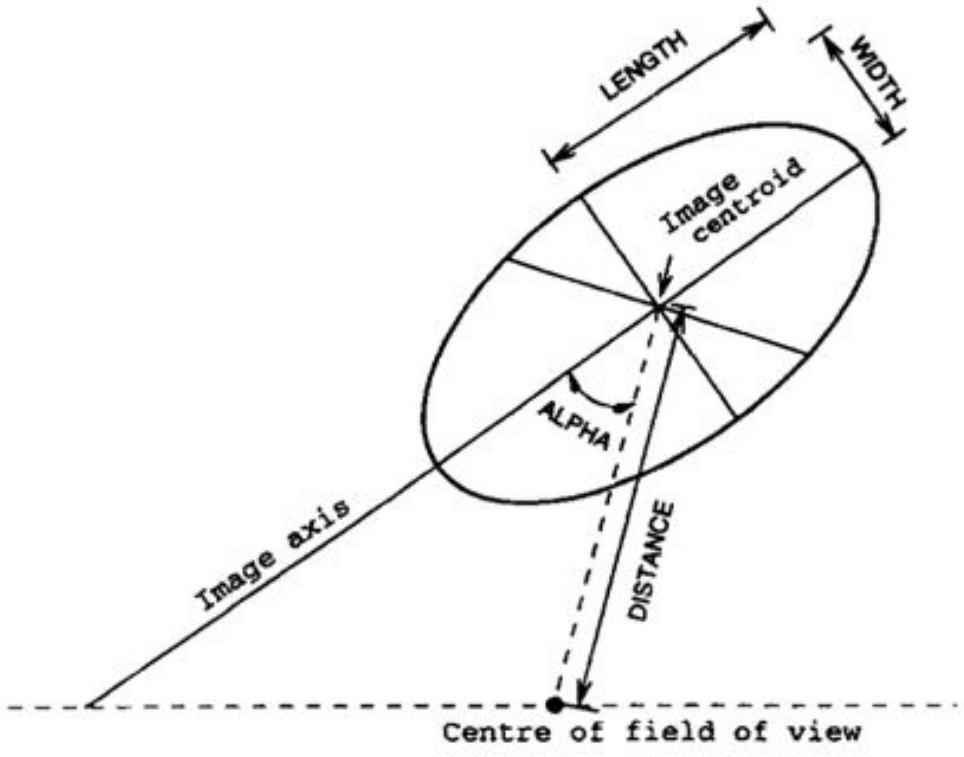

Figure 5.1: The geometric definitions of the Hillas parameters. [a]

a. Reprinted from Astroparticle Physics 9, G. Mohanty et al. *Measurement of TeV gamma-ray spectra with the Cherenkov imaging technique*, Copyright (1998), with permission from Elsevier

images can be superimposed onto a single camera plane. The point in the field-of-view where the image axes intersect indicates the arrival direction. The camera plane can then be projected into the reference frame of the air shower, where the core location–the place on the ground that primary particle would have impacted had it penetrated the atmosphere–can be reconstructed. If two telescopes contribute to the image, then the core location and arrival direction are exactly determined; more than that and they are over-constrained. There can be some error involved in estimating each image ellipse due to fluctuations in the showers, making it difficult to estimate these parameters precisely. This is illustrated schematically in 5.2. The square of the difference between the two-dimensional arrival direction and the center of the field-of-view defines a useful parameter, θ^2, that indicates how close to the pointing direction an air shower arrives (Hofmann et al., 1999).

In general γ-ray air showers are more compact (smaller width and length parameters) and more aligned with the source generating them (smaller α or θ^2) than hadronic showers (Hillas, 1985) .

5.2 Monte Carlo Simulations

Extensive Monte Carlo simulations are necessary to fully account for hadronic interactions of the cosmic rays in the atmosphere and for all of the detector efficiencies. Particle interactions and Cerenkov light production are simulated using the CORSIKA 6.702 air shower simulation package (Heck et al., 1998) in conjunction with FLUKA 2006 (Battistoni et al., 2007) for the low-energy interactions and QGSJET-II for the high-energy ones. Cerenkov light production is tracked from the top of the atmosphere by using a special flag in CORSIKA. Major components of the cosmic-ray all-particle spectrum, including ^{56}Fe, ^{16}O, ^{1}H, and ^{4}He were simulated from energies 1 TeV to 316 TeV. To minimize statistical errors in the energy resolution at high energies, the iron showers were simulated such that there would be at least 20,000 showers triggering the array in each bin of log-energy. The background simulations,

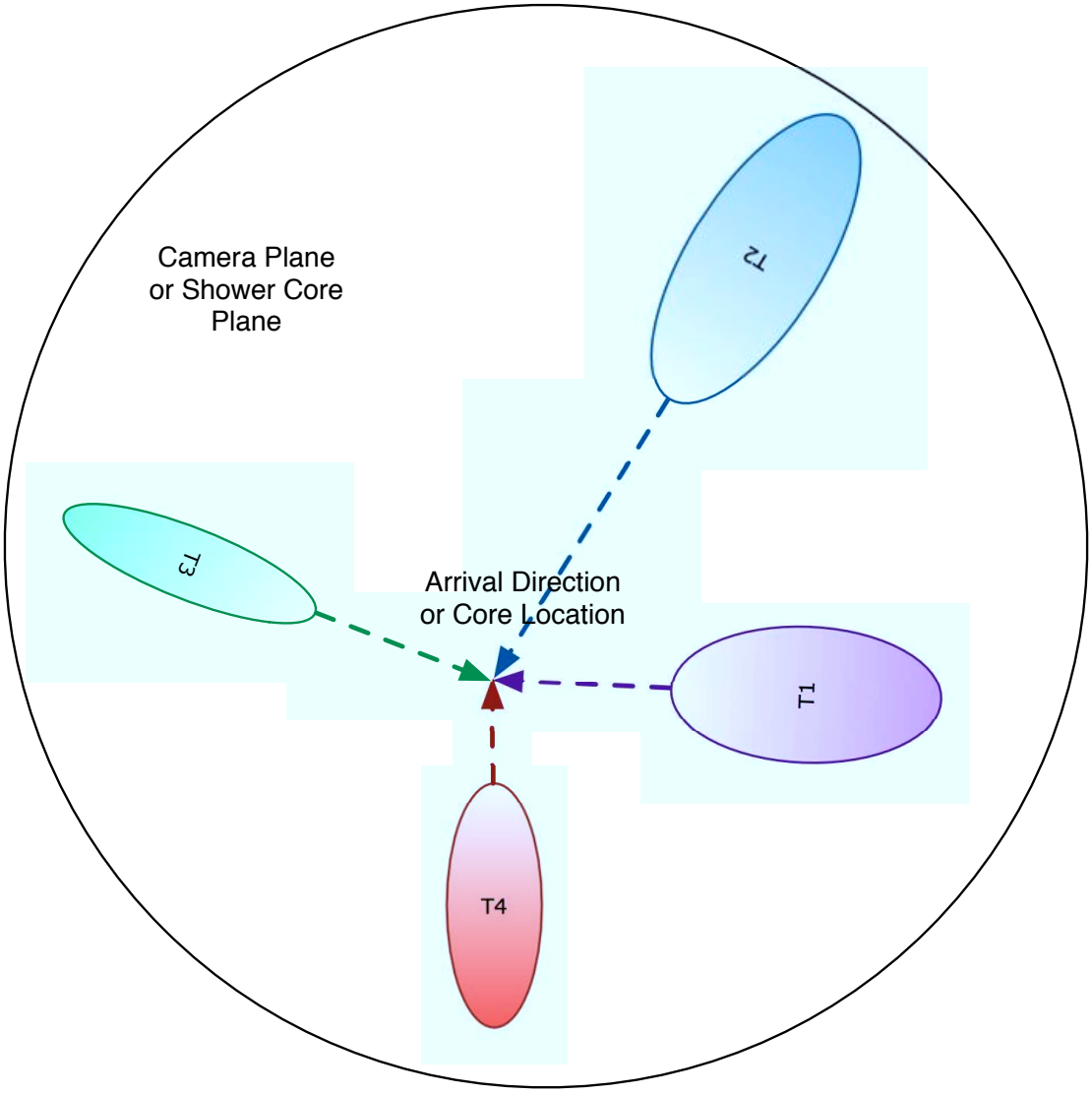

Figure 5.2: Four telescope images are superimposed into a camera plane, or projected into the reference frame of the shower. The arrival direction and core location are represented by the intersection of the image axes.

proton and helium, as well as oxygen simulations were instead simulated on a spectrum of $E^{-2.7}$, because of computing resource constraints. Each component is rescaled to match direct measurements made by TRACER (Ave et al., 2008).

All of the simulations are scattered about a 400 m by 400 m square area, five times per shower for the iron simulations and 50 times per shower for the others. Cerenkov photons are collected in four spherical volumes centered at the positions of the VERITAS telescopes, with radii larger than the mirror diameter to ensure that no light was lost. Atmospheric absorption and the changing density of the atmosphere are calculated using the standard 1976 U.S. atmosphere (Heck et al., 1998).

The depth of maximum electron production, χ_{max}, varies with the mass and energy of the incoming particle. The variations in χ_{max} depend on the cross-section of the nuclear interaction with the air and the inelasticity of the interactions. Protons in general have longer nuclear interaction lengths than iron nuclei, and therefore more variation in their depth of maximum. Furthermore, since the sub-showers in the air showers produced by nuclei must divide the energy of the primary particle among them, they will reach their depth of maximum earlier. Higher-mass cosmic rays will therefore develop their extensive air showers higher in the atmosphere and with less variation (see e.g. Sokolsky (1989)).

Because the Cerenkov light production follows that of the electron production and Cerenkov light is absorbed by aerosols and Rayleigh scattering in the atmosphere, less light will reach the ground from an iron shower than from a proton shower of the same energy. Therefore, the energy threshold for VERITAS will increase with increasing primary mass. Figure 5.3 illustrates this effect by comparing the VERITAS energy threshold for different nuclei.

The response of each telescope is simulated using the GrISU package (Duke & Lebohec, 2010), modified to collect the number of photons emitted above the first interaction height (DC photons) that land on individual photomultiplier tubes. Events that have a minimum of fifty DC photons concentrated into a photomultiplier tube are labelled as "DC events"

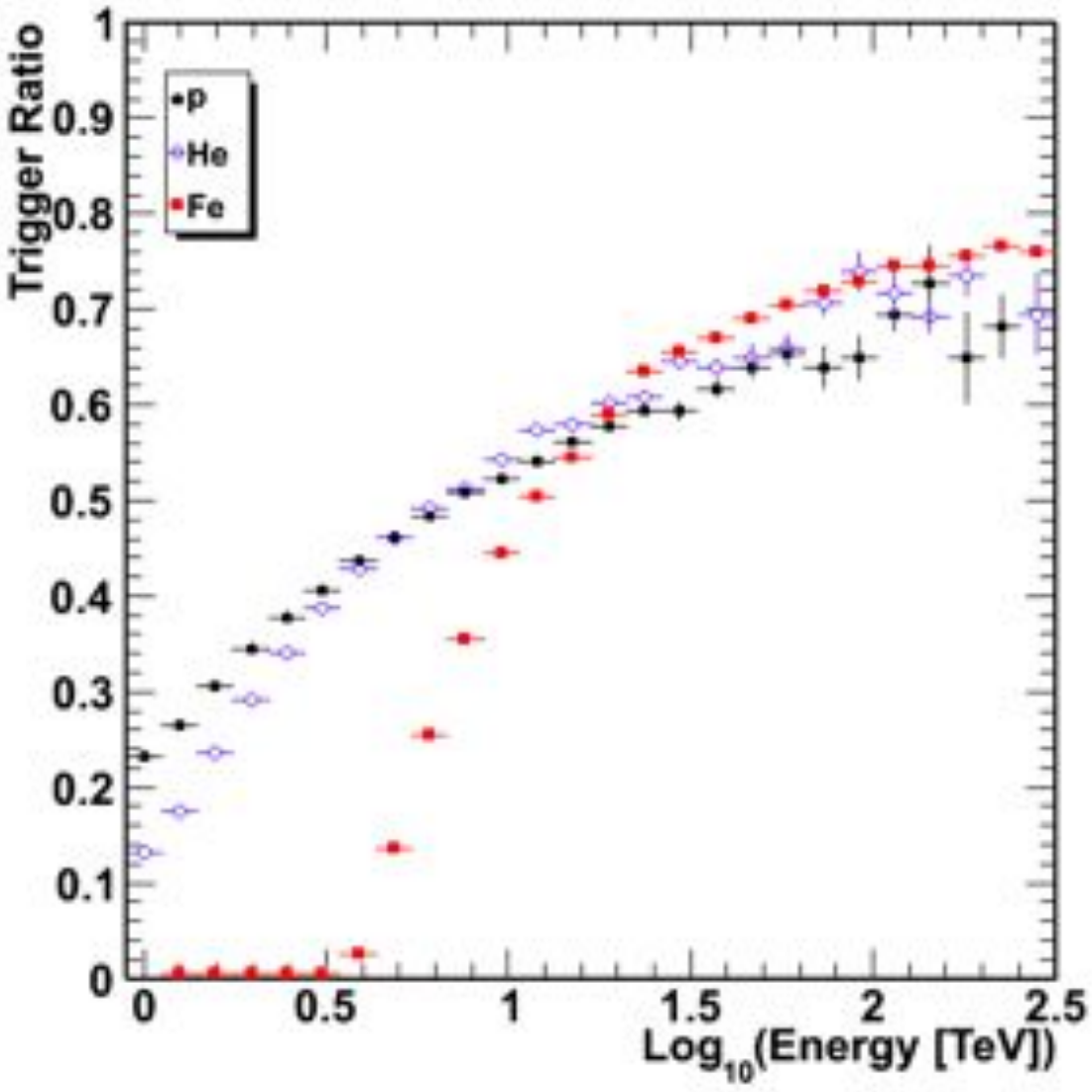

Figure 5.3: The fraction of simulated showers triggering the array plotted as a function of energy. The trigger-level energy threshold various by nuclear species.

for use in training the simulations and cut optimization. GrISU uses measured values for the VERITAS point-spread function, mirror reflectivity and quantum efficiency of each photomultiplier tube. The source position of each simulated event is varied across the entire camera to simulate isotropy in the arrival directions of the cosmic rays.

Figures 5.4 and 5.5 shows the agreement between the simulations and the data selected for the DC analysis (described in more detail in 6.1). Cuts on the total size of the shower and geometry cuts ensure that the data used match the limitations of the simulations. Uncut data include events generated with lower energies and those landing outside of the inner 1.6×10^5 m^2. These data are ignored for this analysis, and therefore, not simulated, because of properties of direct Cerenkov events. The data, shown in black, agree largely with the dominant background due to helium and protons, shown in red. Blue and cyan indicate the DC showers generated by iron and oxygen nuclei, respectively. The background simulations from the protons and helium as well as the nuclear events where DC light does not land within the field-of-view of any of the telescopes (green for oxygen and magenta for iron) follow similar distributions, while the DC distributions are brighter in total size and have a narrower range of geometric constraints.

5.3 DC Light Selection in VERITAS

Direct Cerenkov events are identified in the camera plane by identifying events with two separate Cerenkov light samples: that from the extensive air shower and that from the primary particle. Each camera image in each event is searched for such features and identified using the criteria described in 5.3.2. The direct Cerenkov light is expected to be a compact pulse which will fall into 1-3 pixels on the camera plane. For this reason, one pixel is identified as the "Direct Cerenkov" pixel. As described in 5.3.1, one can exploit the geometry and, to a marginal degree, the timing characteristics of the events to identify that pixel.

A candidate event containing direct Cerenkov light is shown in Figure 5.6. The elliptical

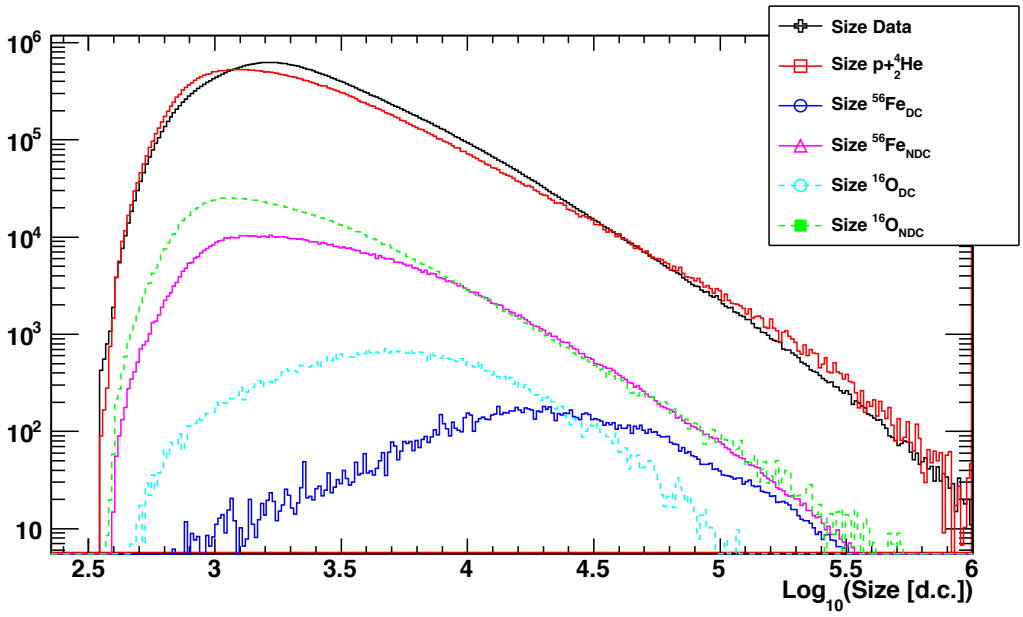

(a) Total shower size (digital counts)

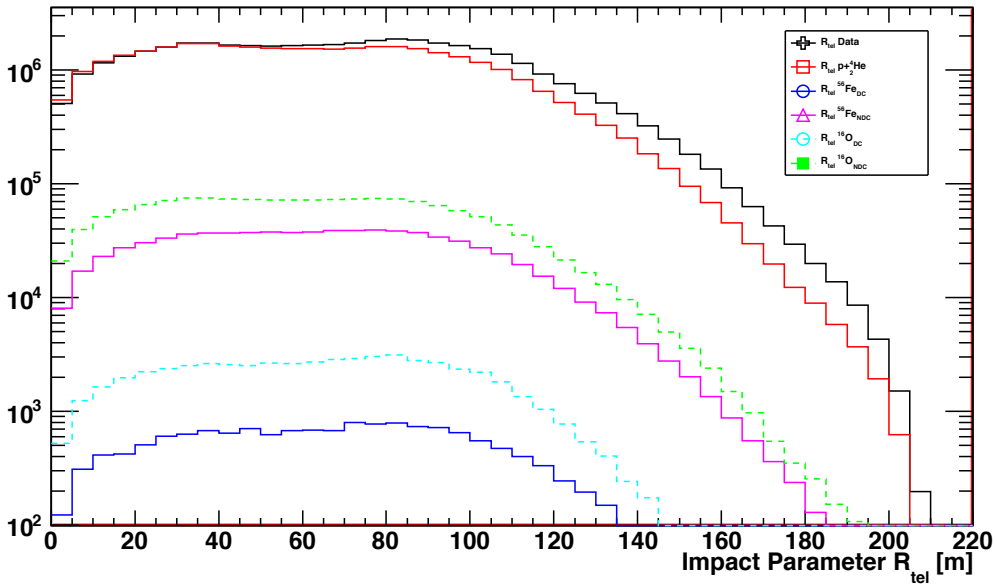

(b) Impact Parameter (m)

Figure 5.4: The total shower size and impact parameter for simulated and data events after quality cuts.

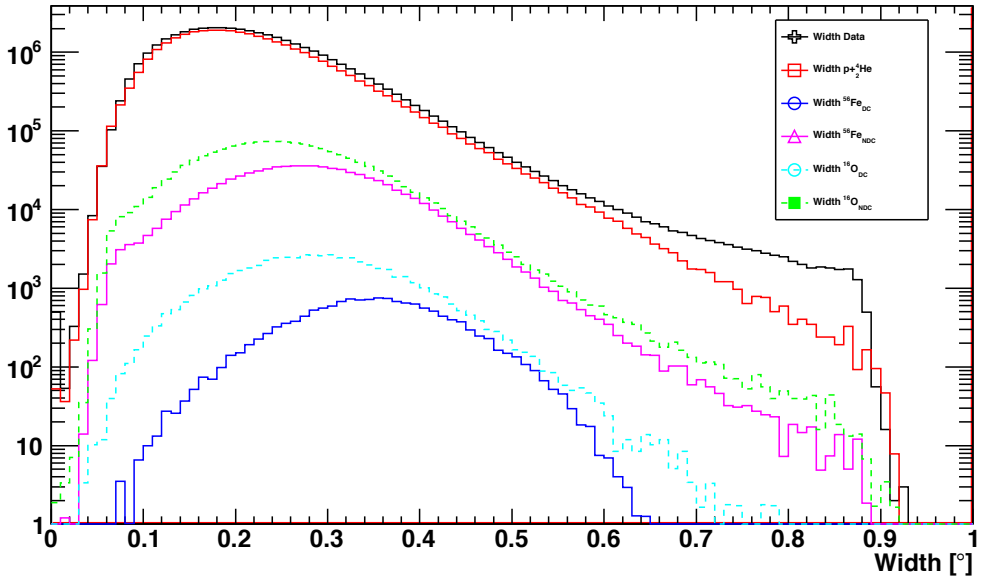

(a) Width (°)

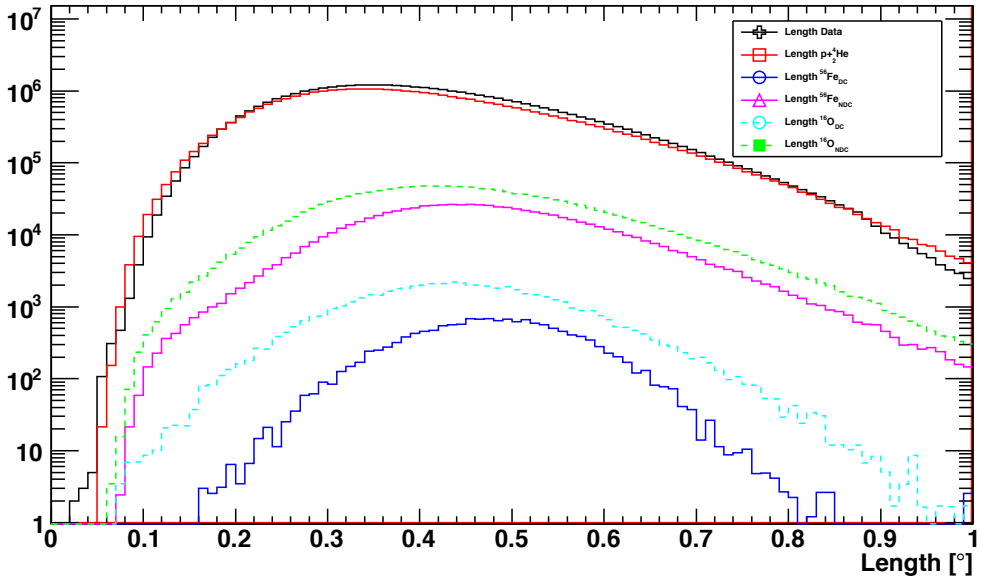

(b) Length (°)

Figure 5.5: Ellipse width and length for simulated and data events after quality cuts.

development of the air shower is clearly seen in all of the cameras, and in three cameras (T1, T3 and T4), one pixel has a high integrated charge close to the front of the shower where the DC light is concentrated. The fourth telescope (T2) is too close to the shower core to collect much Cerenkov light from the primary, so there is no DC light present in that image.

5.3.1 DC Pixel Identification

A search is performed in the camera plane for one pixel containing direct Cerenkov light, because simulations show that the light will be concentrated in 1-3 pixels (evident in Figure 3.3). The DC pixel will be a bright pixel isolated from the rest of the shower, and the search takes advantage of this feature. The pixel will be the one that minimizes the quality parameter defined as:

$$Q_{DC} = \frac{\bar{I}_{neigh}}{I_{DC}} \tag{5.1}$$

where $\bar{I}_{neigh}$ is the average intensity of the neighboring pixels and I_{DC} is the intensity of the pixel itself. To comply with the angular requirements of the event geometry, the search is restricted to a region of the camera defined by three angular distance parameters: that between the DC pixel and the center-of-gravity of the air shower Δ^{DC}_{CoG}; that between the DC Pixel and the arrival direction of the cosmic ray Δ^{DC}_{Dir}; and that from the DC Pixel to the major axis of the shower ellipse $\Delta^{DC}_{\perp}$. During the search, the center-of-gravity (as defined by equations 5.2 and 5.3) is calculated iteratively, ignoring the candidate DC pixel being examined.

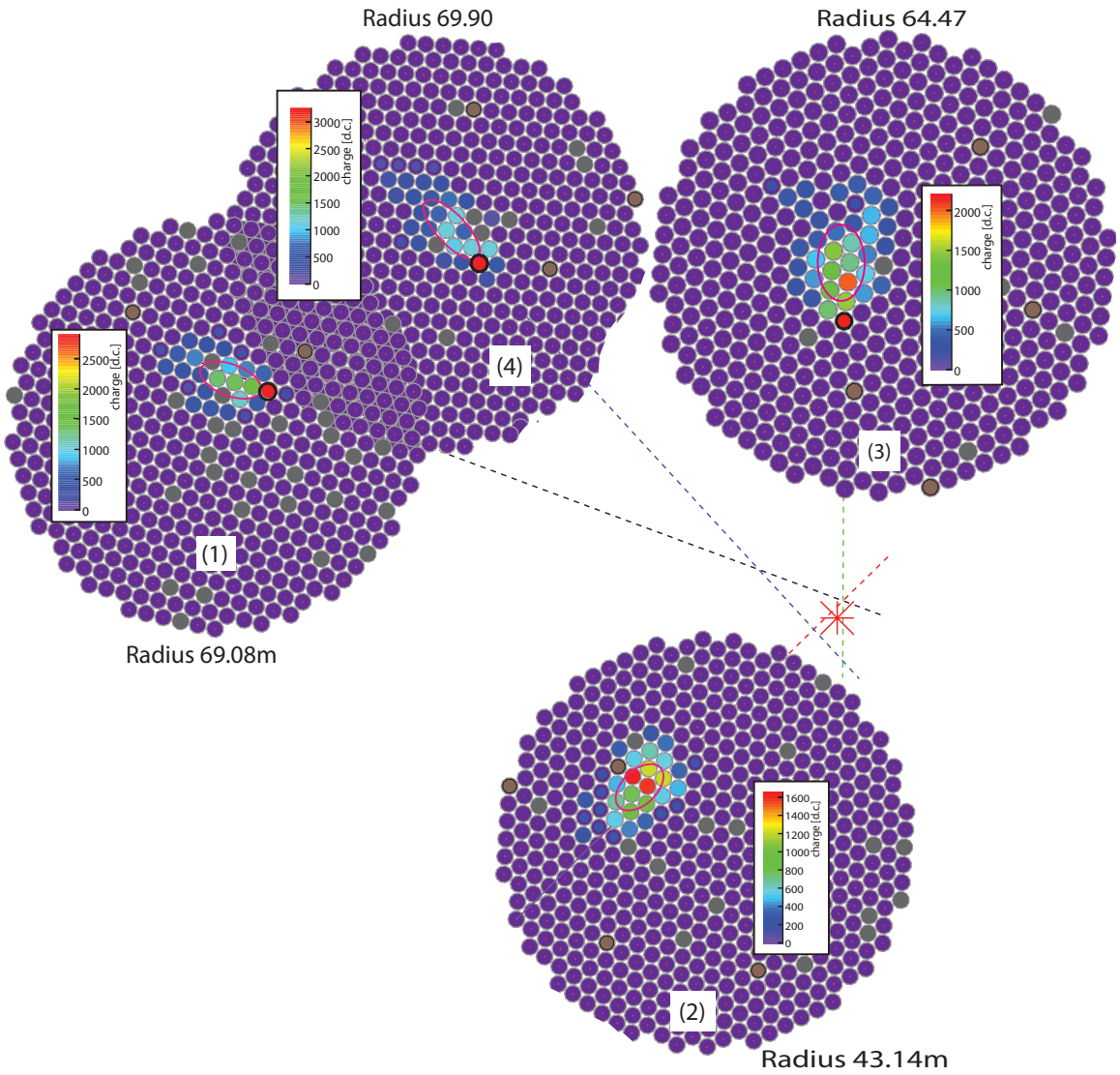

Figure 5.6: A candidate event displayed as integrated charge sums on the camera planes. When a telescope is too close to the shower core (< 50 m as in telescope 2), the density of primary Cerenkov photons is too low to produce a significant DC excess, but at radii between 60 and 70 meters (as in telescopes 1,3, and 4), the maximum number of DC photons seen by each of the three telescopes is 500 photoelectrons.

$$x_{CoG} = \frac{\sum_{i \neq j_{DC}} I_i x_i + \bar{I}^{DC}_{neigh} x_{DC}}{\sum I_i - (I_{DC} - \bar{I}^{DC}_{neigh})} \tag{5.2}$$

$$y_{CoG} = \frac{\sum_{i \neq j_{DC}} I_i y_i + \bar{I}^{DC}_{neigh} y_{DC}}{\sum I_i - (I_{DC} - \bar{I}^{DC}_{neigh})} \tag{5.3}$$

Once the pixel is identified, the amount of DC light can be parameterized by estimating the fraction of light in the pixel that comes from the primary particle. In the absence of DC light, the pixel would likely have a value near the average of its neighboring pixels. So the DC light in the pixel can be estimated as

$$N_{Cerenkov} = I_{DC} - \bar{I}_{neigh}; \tag{5.4}$$

The variation in the $N_{Cerenkov}$ parameter depends on the charge of the primary and the path length through which the primary particle travels. It will be discussed in more detail in Section 6.3.

The geometric region in which the search for the DC pixel is performed was optimized for accuracy. Scanning through the 6-dimensional parameter space defined by minimum and maximum cuts on Δ^{DC}_{CoG}, Δ^{DC}_{Dir} and $\Delta^{DC}_{\perp}$ resulted in the cuts listed in table 5.1. Applying the requirement that the Cerenkov photons in the DC pixel arrive after the photons in the CoG pixel results in a 10% increase in the number of events with accurately identified DC pixels.

Table 5.1: DC Search Region Cuts

Parameter	Minimum	Maximum
Δ_{DC}^{CoG}	0.17	0.91
Δ_{dir}^{DC}	0.	0.45
$\Delta_{\perp}^{DC}$	0.	1.0

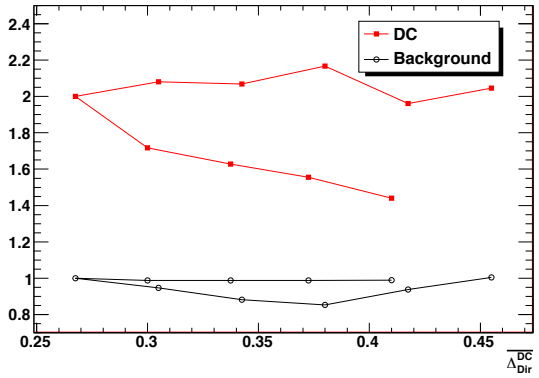

(a) Δ_{Dir}^{DC}

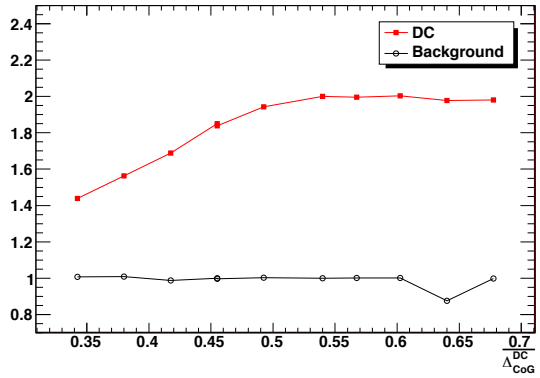

(b) Δ_{CoG}^{DC}

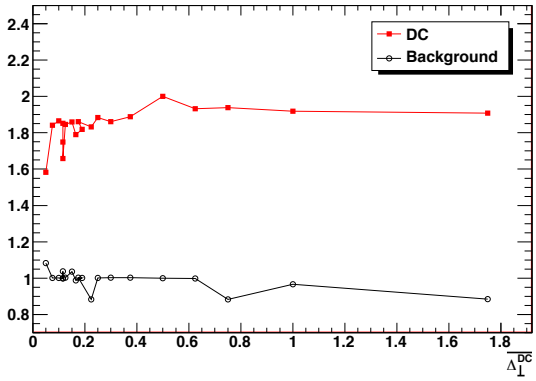

(c) $\Delta_{\perp}^{DC}$

Figure 5.7: DC identification accuracy as a function of the average of the minimum and maximum on the geometric search parameters: Δ_{Dir}^{DC}, Δ_{CoG}^{DC}, and Δ_{Dir}^{DC}, $\Delta_{\perp}^{DC}$. The number of background events that identify a pixel that mimics a DC pixel is also plotted in black for comparison. The DC accuracy is shift by one unit for ease of reading. The curves are non-monotonic, because the minima and maxima of each parameter were varied independently.

5.3.2 Event Selection

The DC events must first be separated from the dominant background coming from protons and helium that should also produce direct Cerenkov light, but at such a low level that it would be indistinguishable from the air shower light. The cuts can be divided into four main categories: quality cuts ensure that the event passes reconstruction requirements and that the simulations match the data; cuts on the Hillas width and length select for an appropriate shower geometry; identification accuracy cuts select DC-like events that have properly identified the DC pixel in the image; and cuts on the geometric search parameters and as well as the impact parameter, R_{tel} help reject the proton and helium background. The final cuts and their proton and helium rejection efficiency are given in Table 5.2, which is subdivided by category.

The expected number of events from protons integrated over 400 hours in an 1.6×10^5 m^2 area would be $\sim 10^5$. Therefore, the cuts must be able to reject $> 10^5$ proton and helium simulations. When all of the cuts are combined, the proton rejection power is 2×10^7, satisfying this requirement. It is important to note that all of the simulated proton and helium showers do not pass the cuts, and they can be excluded from the sample at the 99.4% level.

The minimum cut on $N_{Cerenkov}$ ensures that the DC pixel is accurately identified in the camera. Figure 5.8 compares the $N_{Cerenkov}$ distributions from all of the cameras where at least one telescope collects DC photons. The black curve includes contributions from all events that pass the quality cut $Q_{DC} < 1.0$, while the red curve includes only events that have accurately identified the pixel that contains the most DC photons in the simulations and requires that the minimum number of photons in that pixel is fifty. A cut requiring that $N_{Cerenkov} > 80$ photoelectron (400 digital counts) ensures that the pixel identified is the true DC pixel. Note that some events that are labelled as inaccurate may still contain DC light in the selected DC pixel: there would be either less than fifty DC photons or the

Table 5.2: The proton and helium rejection power ("pHe Rej.") and remaining DC to background ratio ("Ratio") are given for the three categories of DC cuts described in the text. The cases where only the selected category of cuts are applied (the "Cut Power" column) and where all of the cuts excluding the selected category (the "Power without Cut") are shown. Using all of the cuts in coincidence generates a proton-rejection power of 2×10^7.

Category	Parameter	Min	Max	Cut Power		Power without Cut	
				Ratio	Rej.	Ratio	pHe Rej.
Hillas	width	0.3	...	0.011	9.45	3.36	176211
	length	0.3	0.7				
DC Event	I_{CoG}	100	...	0.049	152.918	4.16	115232
	$N_{Cerenkov}$	400	...				
	Q_{DC}	0.2	1.0				
	Q_{DC}	$< 0.428 \log(\text{size})$ -1.4					
Geometry	Δ^{DC}_{CoG}	0.6	0.9	0.13	3295	0.63	2506
	$\Delta^{DC}_{\perp}$	0.0	0.2				
	Δ^{DC}_{Dir}	0.0	0.2				
	Δ^{CoG}_{Dir}	0.5	0.9				
	R_{Tel}	50.0	150.0				

selected pixel is adjacent to the pixel with the most DC photons.

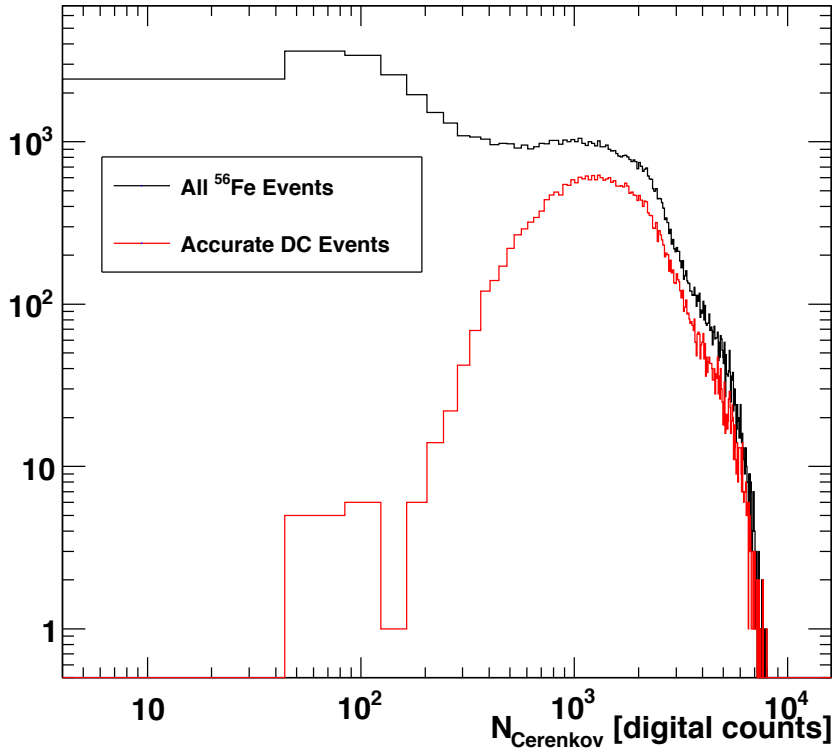

Figure 5.8: The distribution of $N_{Cerenkov}$ shown for simulated events that have DC light in at least one telescope (black) and only the events that have accurately identified DC pixels (red). A cut applied at 80 p.e.s (400 digital counts) ensures that the DC pixel is likely identified.

A particularly powerful cut is the cut on the Q_{DC} parameter (see equation 5.1) as a function of the total shower size. The Q_{DC} value should be lower for the bright isolated pixel expected in a DC event, but because more light from the extensive air shower leaks into the DC pixel as the air shower becomes brighter, the Q_{DC} parameter should grow with size. The Q_{DC} of the background events should also grow with the total brightness in the camera, because fluctuations in the shower will become comparably dimmer as the size increases. However, because those events in which the DC light is discernible should have brighter, more isolated pixels, Q_{DC} is lower for the DC events than for the background at a

given shower size, as seen in Figure 5.9.

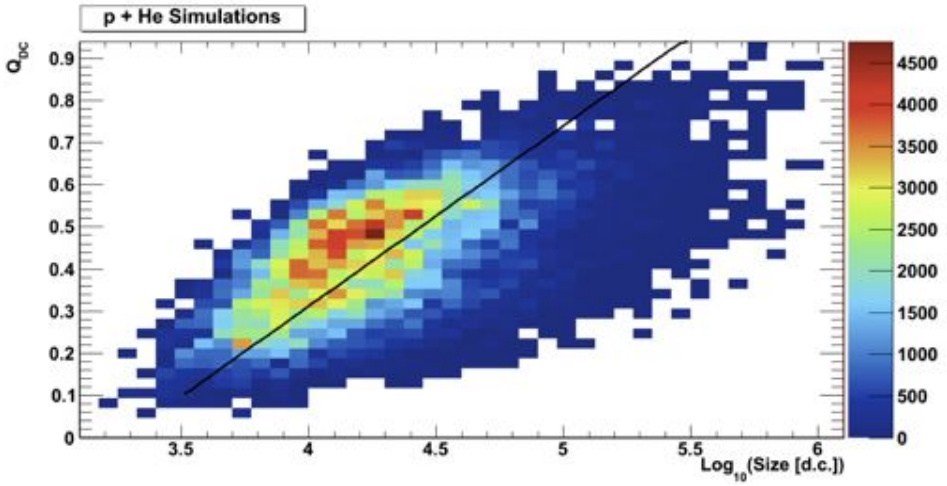

(a) Simulated proton and ^2He events

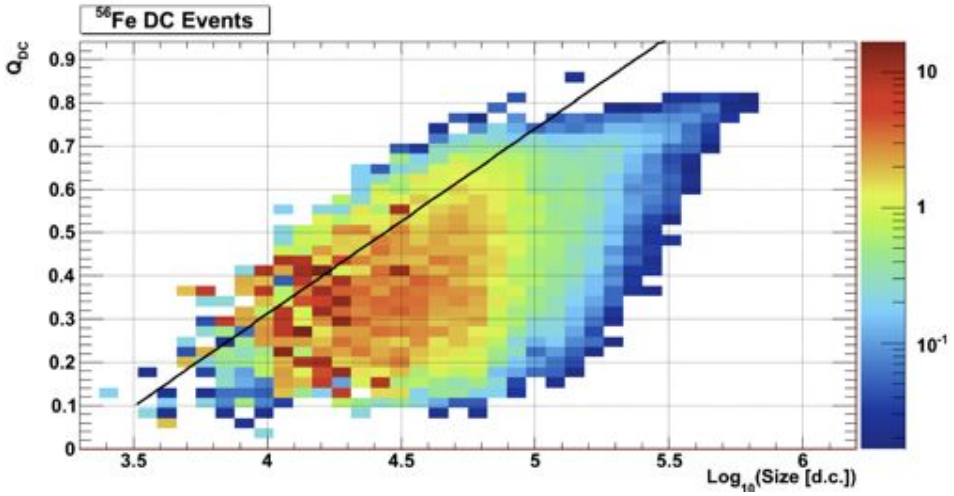

(b) Simulated ^{56}Fe events

Figure 5.9: The shower size-dependent cut on the quality parameter, Q_{DC} (equation 5.1), eliminates proton and helium showers by an additional factor of 580 when used in conjunction with the other cuts. The black line follows the size-dependent cut listed in Table 5.2.

The expected rates after cuts are applied are shown in Figure 5.10. The cuts were selected to eliminate the background from proton- and helium-induced showers. DC light from oxygen is too low to be included in this analysis and is effectively removed from the sample particularly when employing the shower-size-dependent cut on the Q_{DC} parameter. Protons and helium are expected to be present at the 0.06% level, meaning that one in

1.7×10^3 events will be a background event. An estimation of the remaining oxygen events is included in Section 6.3.

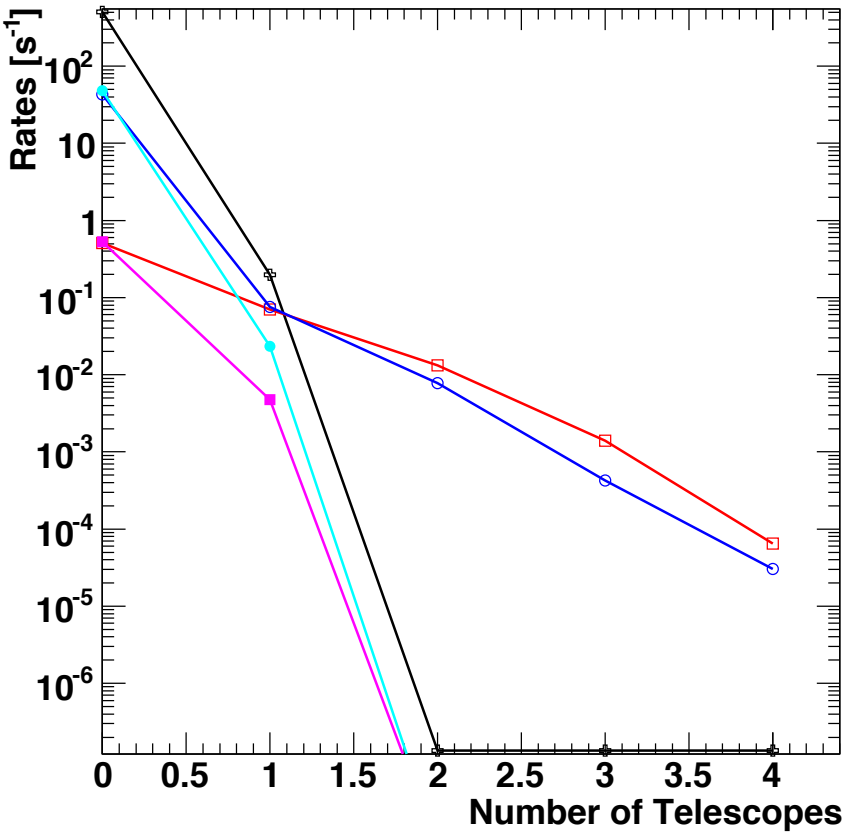

Figure 5.10: The expected rates for protons and helium (black crosses), iron events tagged as DC events (red, open squares) and those without DC light (blue open circles), and oxygen events tagged as DC events (magenta, closed squares) and those without DC light (blue closed circles) when requiring between zero and all four telescopes pass the DC cuts. The cuts are capable of rejecting all of the proton and oxygen simulations after requiring that two telescopes pass the cuts.

CHAPTER 6

OBSERVATIONS OF THE IRON NUCLEI AT VERY-HIGH ENERGIES

6.1 Data Selection

Because cosmic rays are effectively isotropic at TeV energies, all observations taken by VERITAS can be used for the DC measurement; however, to reduce the amount of simulations necessary for the analysis, it was appropriate to select data that only fall into a high elevation band. A survey of the mean elevation of the telescopes shows that the most populous elevation band is between 70° and 80°. Therefore, the data selected are restricted to this zenith angle band.

Another analysis requirement employed during data selection was that the observations must have been taken in consistent weather conditions where there was little to no cloud coverage. Observers record the weather conditions for each 20-minute run on a graded scale (A-D). Additionally, the far-infrared (FIR) data taken simultaneously with gamma-ray observations correlates with the level of cloud coverage, such that a low FIR temperature of $\sim 41°$ F that remains steady corresponds to a clear night with little humidity. The data used in this analysis must receive at least a B rating.

The third and final requirement for data to be included in this analysis was that all four telescopes were used during data-taking. Occasionally, a telescope is removed from the array due to safety concerns or to perform engineering tasks, but since the likelihood of observing DC light in more than one telescope is greatly reduced when a telescope is removed from the array (see Figure 5.10), the data taken under those conditions unnecessarily complicate the sample.

The total sky covered in the final data sample shown in Figure 6.1 illustrates that only a small portion of the Northern celestial sphere can be sampled when employing these con-

straints in an observatory that makes pointed observations. However, the cosmic-ray observations can be made in conjunction with the higher-priority gamma-ray targets, meaning that the background data taken for gamma-ray observations can be used in the DC analysis. More detail about the data selected for use in this analysis is given in Appendix A.

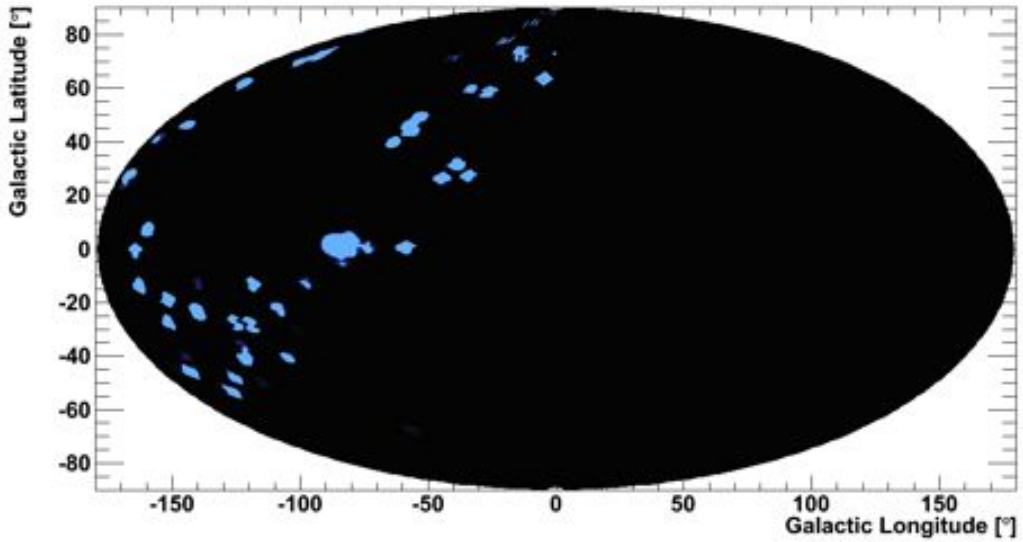

Figure 6.1: The exposure in minutes covered by VERITAS during the 2007-2009 seasons shown in galactic coordinates. Data are only used if taken at high elevation (70°–80°) and in favorable weather conditions.

Because most of the DC events produce showers close to the telescopes and have high primary energies (> 10 TeV), the data can be reduced on a raw-level basis, by applying a cut on the total charge collected by a camera. Summing the FADC channels above a certain threshold correlates with the Hillas parameter size calculated after cleaning the image. Applying this cut on the raw data greatly reduces the computing resources required to analyze 409 hours of data. In spite of there being 73 different source-fields included in the data set, the Hillas sizes remain uniform for both galactic sources and extragalactic sources, as shown in Figure 6.2.

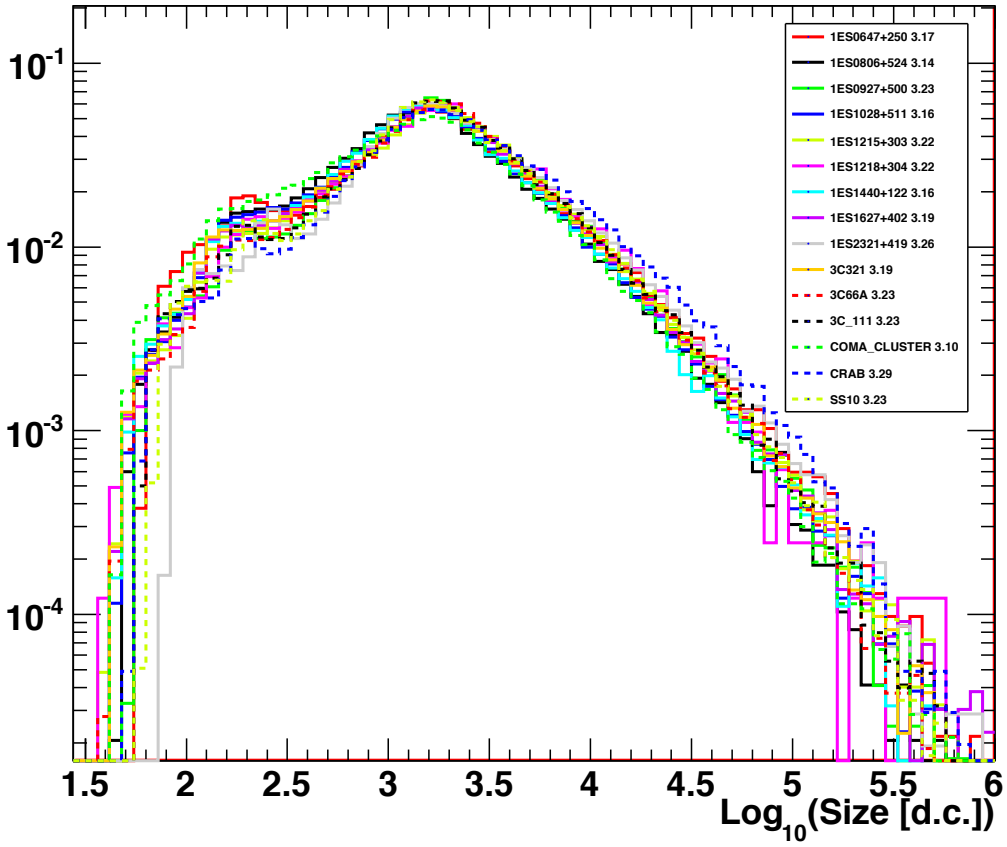

Figure 6.2: The Hillas size distribution for a number of sources selected from the complete data set.

During the normal course of observations, the data acquisition system will miss some

air shower images as it writes data to disk. So for a small fraction of each data run, the telescope will not be taking data. To properly recover the flux of cosmic rays, it is therefore necessary to estimate the observation time as accurately as possible. Each event includes a timestamp set by the L3 GPS clock and by comparing the timestamps of subsequent events, the total dead time is a exponential fit to the time differences between events.

6.2 Energy Reconstruction

Qualitatively, more particles above the Cerenkov threshold are available to initiate Cerenkov radiation in higher energy showers than lower energy showers. Telescopes that are further away from the shower core will image light coming from outside of the core. Therefore, the total light collected by an individual telescope increases with primary energy and decreases as the telescope gets further from the shower core. However, these are not strictly linear relationships. Shower-to-shower fluctuations in particle production and the first interaction height as well as Cerenkov light absorption in the atmosphere complicate energy reconstruction. Furthermore, depending on the angular distance from the center of the camera (dist) to the center of the shower image, showers can be truncated in the camera plane. For the reasons listed above, tables are constructed from 80% of the ^{56}Fe Monte Carlo simulations using the shower size, impact parameter and offset distance in the camera to reconstruct the primary energy.

Look-up table construction proceeds by selecting the bin that corresponds to the size, impact parameter and dist for each simulated event. Each bin contains the log-weighted average of the energies of the showers with parameters that correspond to the bin. Two-dimensional slices of the look-up table used are shown in Figures 6.3a, 6.3b and 6.3c.

While each telescope gives an estimate of the energy of each shower, combining measurements from all of the telescopes permits a more robust estimate of the total shower energy. A log-weighted average of the contribution from each telescope that passes rudimentary

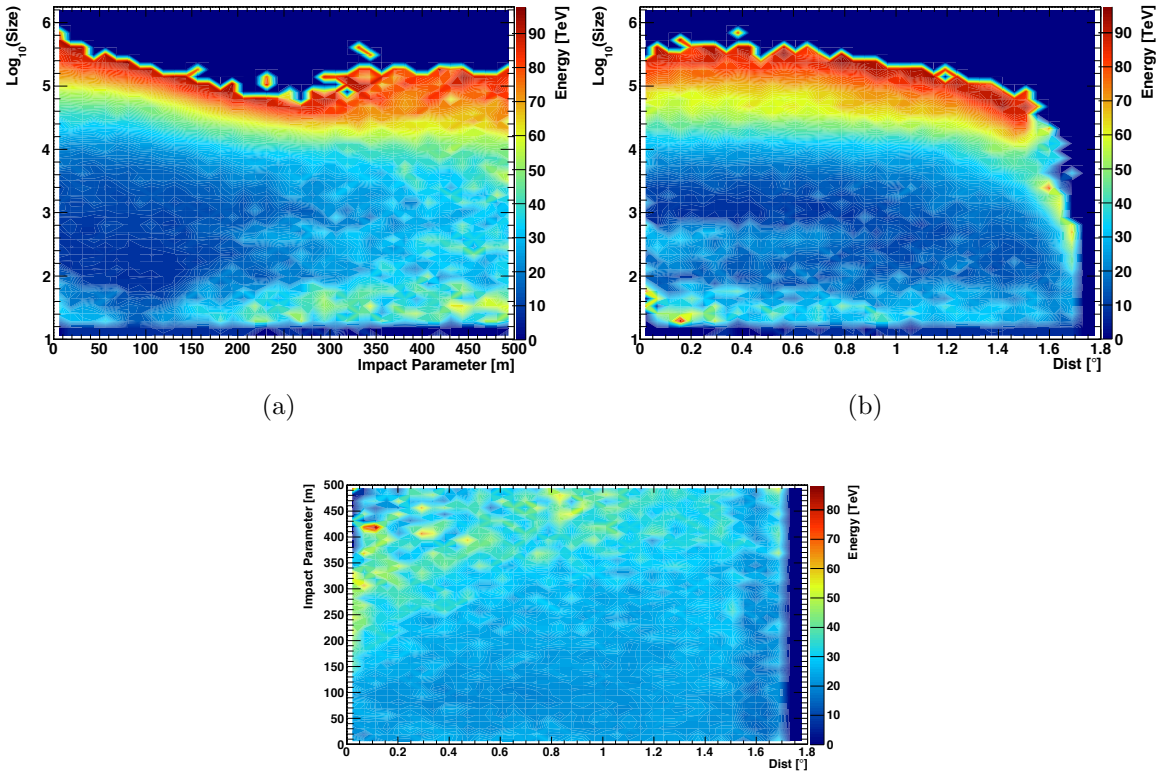

(a) (b)

(c)

Figure 6.3: Two-dimensional slices of the look-up table used to reconstruct shower energies. The shower size is the total amount of Cerenkov light in digital counts, while the impact parameter is the distance from the telescope to the shower core, in the reference frame of the air shower. The "dist" parameter is the angular distance in each camera plane from the center of the camera to the center of the ellipse fitted to each cleaned shower image.

quality cuts required for proper shower reconstruction is used to make the final estimate, as in Equation 6.1. Each telescope is weighted by the root-mean square of the number of simulations used to make the estimate, σ_t. The final energy is computed after interpolating among bins adjacent to the selected bin in the look-up table.

$$\log_{10} E_{final} = \frac{\sum_{t=1}^{4} \sigma_t \log_{10} E_t}{\sum_{t=1}^{4} \sigma_t} \tag{6.1}$$

To estimate the energy resolution, the difference between the true Monte Carlo energy and the reconstructed energy is fit with a Gaussian in the range defined by the full-width half-maximum, as shown in Figure 6.4. This is performed for evenly spaced bins in log-energy. The mean value of the Gaussian indicates the most likely error in the reconstructed energy, while the width of the gaussian represents the energy resolution in each bin.

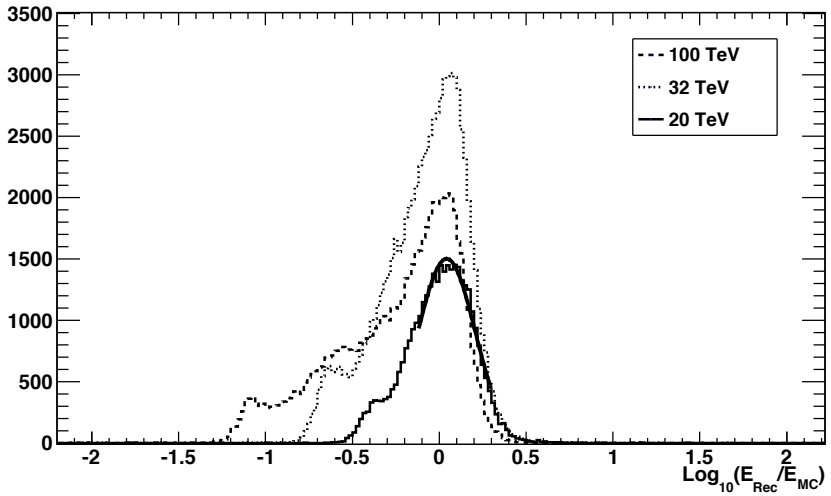

Figure 6.4: The error in energy reconstruction for 3 energy bins: 20 TeV (solid line), 32 TeV (dotted line), 100 TeV (dashed line). The number of entries in each histogram reflects the change in collection efficiency as a function of energy.

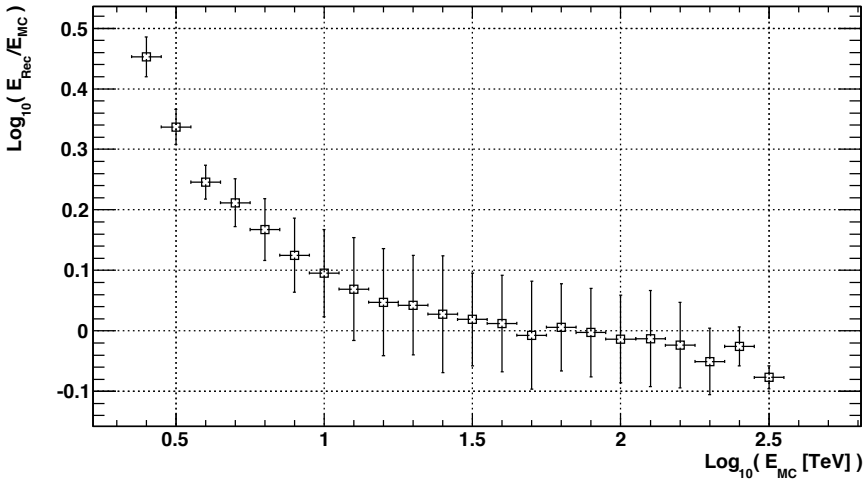

(a)

Figure 6.5: The bias in energy reconstruction as a function of energy. The figure shows the energy reconstruction bias for tables constructed with a log-weighted average.

The error in energy reconstruction for each bin in log-energy, as shown in Figure 6.5, depends on the range of energies used to construct the look-up tables. The lack of energies below the trigger threshold cause the lower-energy showers to get systematically reconstructed to a higher energy. A similar effect occurs at higher energies, where the showers are reconstructed to lower energies, on average. However, as the energies increase, the degeneracy in the energy reconstruction becomes more pronounced and the error distribution becomes non-Gaussian, as shown in Figure 6.4. For this reason and because the expected flux from cosmic rays follows a heavy-tailed distribution, overlap corrections are necessary for constructing the final energy spectrum. The energy resolution in the region of interest for this measurement is 16.4% on average (23.5% at worst), while the bias in energy reconstruction ranges from -20% to 25% in the energy range of interest for this measurement (10 TeV – 158 TeV).

6.3 Charge Reconstruction

The cuts used in this analysis are optimized to reject the dominant proton and helium background, but in order to confirm that the DC technique is a viable method for measuring the composition of the nuclear component of the cosmic ray spectrum, an estimation of the charge of the incoming particle must be made. As discussed in Section 2.4, the Cerenkov light emitted by a charged particle per unit path length, $\frac{dN_{Cer}}{d\chi}$, scales as Z^2. Ideally, after extracting the DC light from the image and estimating the distance over which the particle emits Cerenkov light, $\Delta\chi$, the charge would be reconstructed as $Z_{rec} \propto \sqrt{N_{Cer}/\Delta\chi}$. However, in practice, it is difficult to reconstruct the path length through which the particle travels through for two reasons. Firstly, nuclei of the same energy will initiate Cerenkov radiation at different altitudes, as shown below. Secondly, the narrow angle of the Cerenkov light emitted at the top of the atmosphere makes it difficult to estimate the emission height.

The changing index of refraction affects the energy threshold at which a given nucleus will initiate Cerenkov light. Using the approximation given in equation 2.7 and the requirement for Cerenkov light production defined by equation 2.1, a toy model can be constructed that yields great insight into the DC photons collected at the ground level, but without a large overhead in computing resources.

The energy threshold, E_{th}, as a function of altitude and the height, h_{max}, at which a nucleus of a certain energy starts initiating Cerenkov light can be calculated in this toy model. The equations 6.2 and 6.3 are represented graphically in Figure 6.6.

$$E_{th} = \frac{E_0}{\sqrt{1 - \frac{1}{(1+\delta \exp(-h/h_0))^2}}} \tag{6.2}$$

$$h_{max} = -h_0 \ln\left(\frac{-1}{\delta} + \frac{1}{\delta\sqrt{1-(E_0/E)^2}}\right) \tag{6.3}$$

After collecting the direct Cerenkov photons, the charge needs to be reconstructed with-

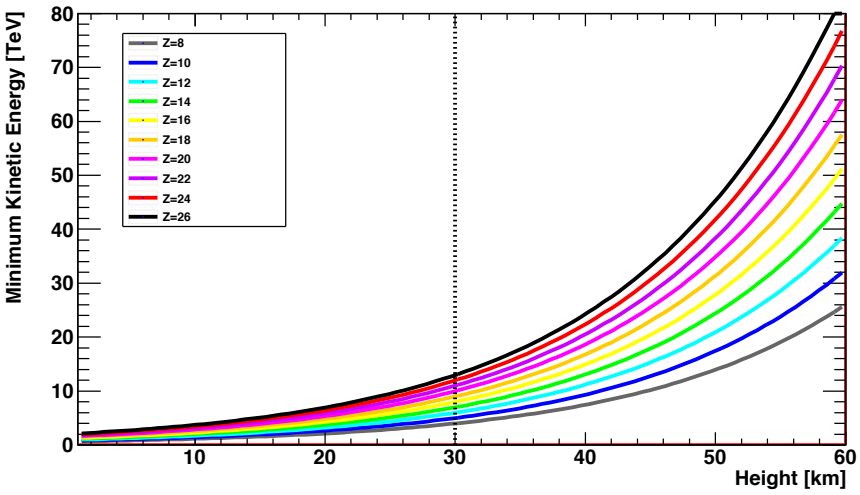

(a)

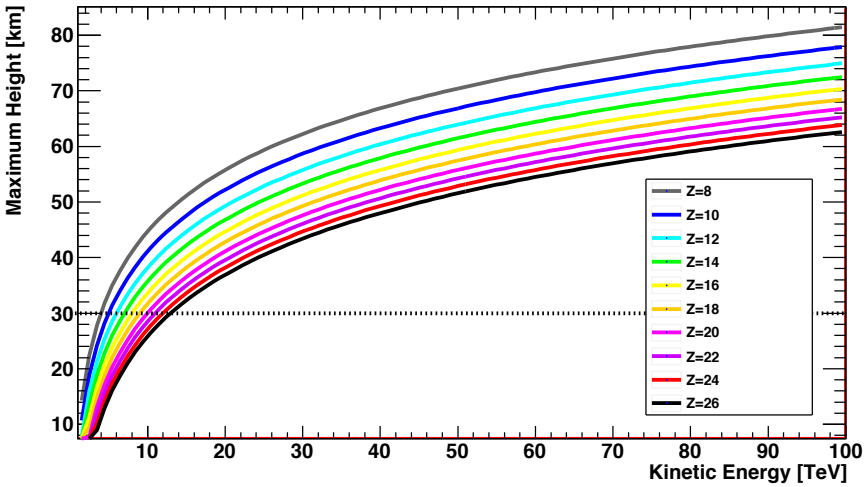

(b)

Figure 6.6: Thresholds for Cerenkov light production in a medium that increases its density exponentially. The energy thresholds (a) and maximum height at which Cerenkov radiation would begin (b) are shown for even-charged nuclei from oxygen to iron. Note that below approximately 30 km, these nuclei will interact hadronically and will therefore not produce any direct Cerenkov light.

out precisely knowing the amount of material traversed by the particle before interacting, $\Delta\chi$. The probability distribution of $\Delta\chi$ for each nucleus is a convolution of the exponentially varying density, the energy spectrum of the species, the energy threshold for DC light production and the likelihood of a nuclear interaction. The $\Delta\chi$ distribution can roughly be estimated by an exponential with a long tail. As a result the total light emitted by each nucleus integrated over the distance between the height where DC light begins and where the air shower begins varies over many orders of magnitude as shown in Figure 6.7b. If $\Delta\chi$ could be estimated on an event-by-event basis, then the charge spectrum would emerge as in Figure 6.7a.

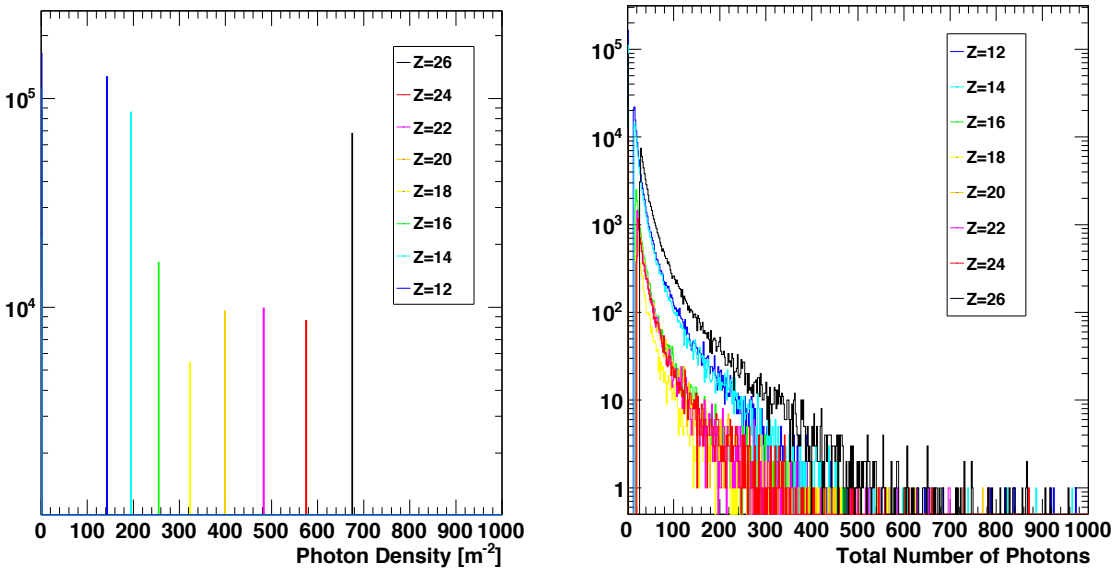

(a) (b)

Figure 6.7: Simulated DC light from various nuclei weighted by their known abundances and spectra integrated from their DC-light production energy threshold. The density of photons per unit path length scales as Z^2 (a), but the total number of photons accumulates until the particle interacts (b).

Instead, the charge spectrum must be estimated by assuming that the radius at which the photon lands can act as a proximate estimate for the height at which it was emitted.

Figure 6.8a shows the reconstructed charge for simulations where the radius is known for each photon and the nuclear interaction length is known for each nucleus (the solid histograms) and where a rough approximation for the radius and interaction length are used in the reconstruction (dotted histograms). The latter more accurately represents the capabilities available to VERITAS, because the distance between the telescope and the shower core is the best estimate of the radius at which each photon lands and has an associated error of ~ 40 m that grows with the true distance from the center of the array. Nuclei are simulated at energies weighted by their known spectra, integrated from each nucleus's energy threshold. The total number of nuclei simulated is controlled by their known abundances (Amsler et al., 2008), starting at the energy threshold defined by equation 6.2. Light is only collected from nuclei that have $h_{max} > 30$ km. Each reconstructed histogram is fit using a Landau function where the most-probable value is used to estimate the charge reconstruction efficiency shown in Figure 6.8b. While there are distinctly long tails in the charge distribution, peaks are still visible for oxygen, neon, magnesium, silicon, and iron. The reconstructed charge number from the fits, shown in Figure 6.8b, is roughly linear with the simulated charge number.

In terms of estimating the iron fraction in the charge spectrum, the dominant background would come from the more abundant lighter nuclei like oxygen, because their energy threshold is a factor of four lower than that of iron nuclei. These simulations motivate the charge reconstruction method used on the data. Oxygen simulations are shown in Section 5.3.2 to be eliminated in the event selection after requiring that two telescopes contain DC events, because they mimic proton and helium events. However, limitations in the number of oxygen simulations cause me to revisit this issue. Comparing the charge distributions after single telescope cuts defines the scale between where the oxygen and iron distributions peak, as shown in Figure 6.9. Note that the simulations and data are scaled such that the iron simulations match the peak in the data. There remains a corresponding peak where the oxygen simulations reconstruct.

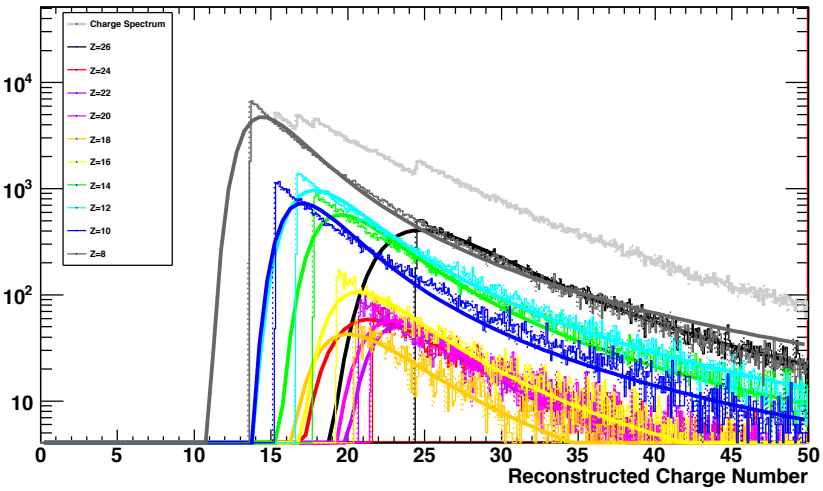

(a)

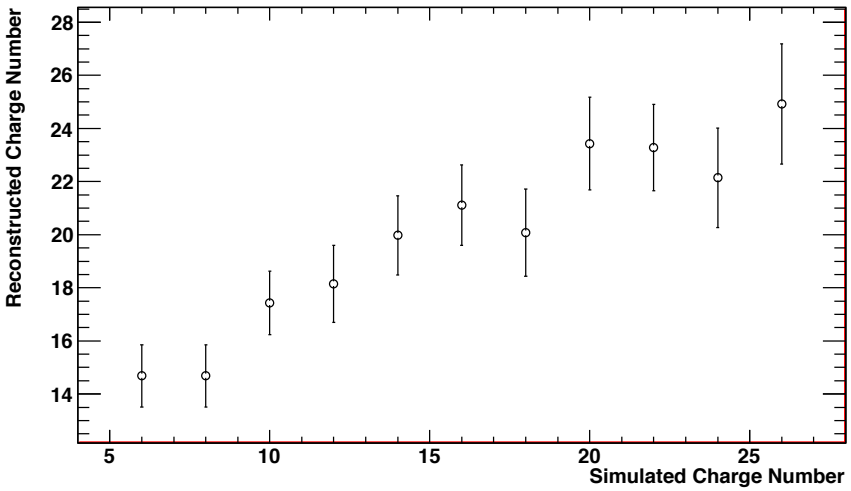

(b)

Figure 6.8: The reconstructed charge can be represented by a Landau function, given the radius at which the photons arrive. The solid histograms use the simulated radius at which the photons arrive and the nuclear interaction path lengths for each nucleus, while the dotted histograms assume an average nuclear interaction path length of 122 g cm^{-2} and a mean radius of 27.9 m (a). The most-probable value and sigma parameters of the Landau function represent the charge reconstruction efficiency for each nucleus (b).

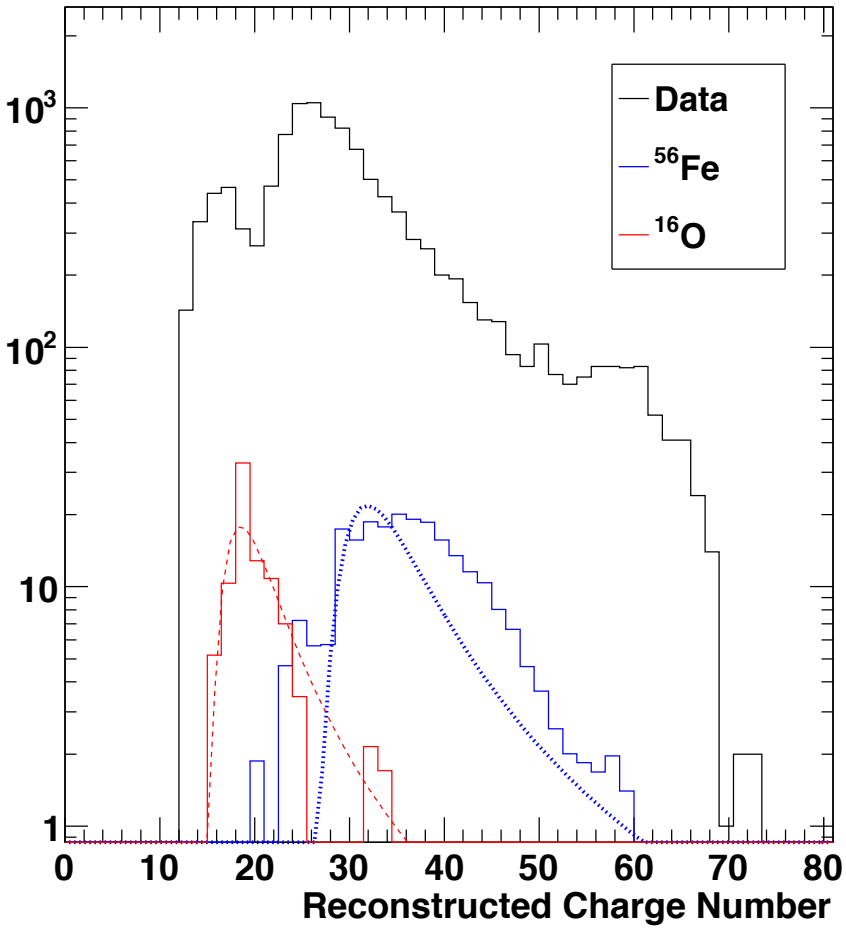

Figure 6.9: The reconstructed charge distribution after requiring that at least one telescope pass the DC cuts. The data are contaminated by protons, but the simulated oxygen and iron set the scale for the charge reconstruction described in the text.

The contamination from oxygen nuclei after requiring that two telescopes image DC light can then be estimated by comparing the data and the iron simulations with an additional contribution from oxygen. The charge distribution from the data shows a peak that matches the iron simulations and a "shelf" at lighter charges. The level of oxygen contamination is varied on the 1% level until the χ^2 between the simulations and the data is reduced by 20%, as shown in Figure 6.10. The process is repeated by adding in contributions from other evenly-charged nuclei at the 0.1% level. The best fit maintains that oxygen is present in the data at the 19.3% level and that the other nuclei are present at the 1% level. Applying a cut on the charge at $Z_{rec} = 22$ reduces the level of oxygen contamination to 12.0% and the nuclear contamination to 0.8%. The half-width-half-maximum of the simulated iron nuclei after applying the cut on the reconstructed charge at implies a charge resolution of 21.5%.

6.4 Spectral Reconstruction

6.4.1 Effective Area

The effective area for the VERITAS array can be considered the fraction of simulated events that both trigger the array and pass the quality and DC selection cuts within the area about which the showers were simulated. So the effective area as a function of energy represents the responsiveness of the detector and analysis technique. Only one in ten simulated iron showers produces DC light in the telescope array. The area simulated is limited to 1.6×10^5 m^2 even though events in the data have reconstructed shower cores that extend 1000 m from the telescopes. The effective area is therefore rather low ($\sim 10^2$–10^3 m^2), as shown in Figure 6.11, when compared to the typical effective area of a gamma-ray analysis (10^5 m^2).

The analysis is most efficient between 20 TeV and 125 TeV. There is a slight loss of efficiency at high energies likely due to the showers getting truncated in camera. This is compounded by requiring that more than one telescope pass the cuts.

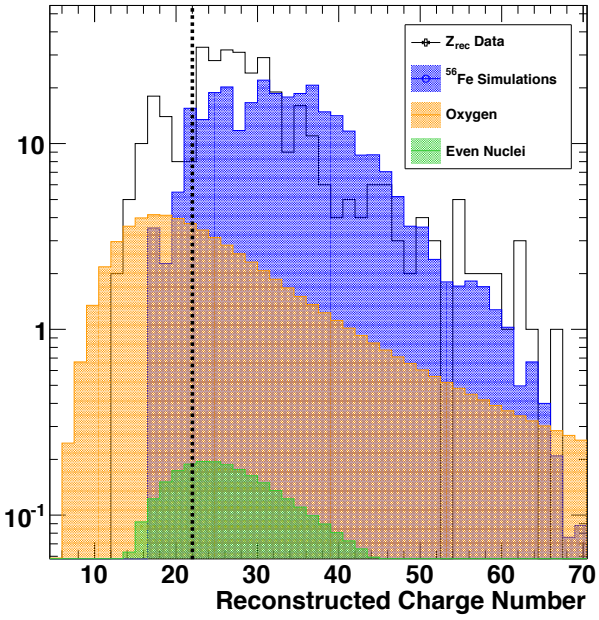

(a)

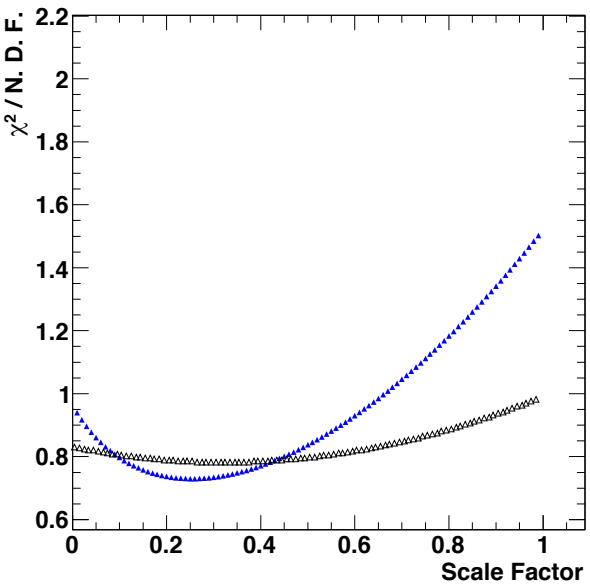

(b)

Figure 6.10: χ^2 minimization shows that the oxygen nuclei are the dominant contaminant to the iron sample, where the peak in the oxygen simulations is 17% of the iron peak. A contribution from other nuclei is present at the 1% level.

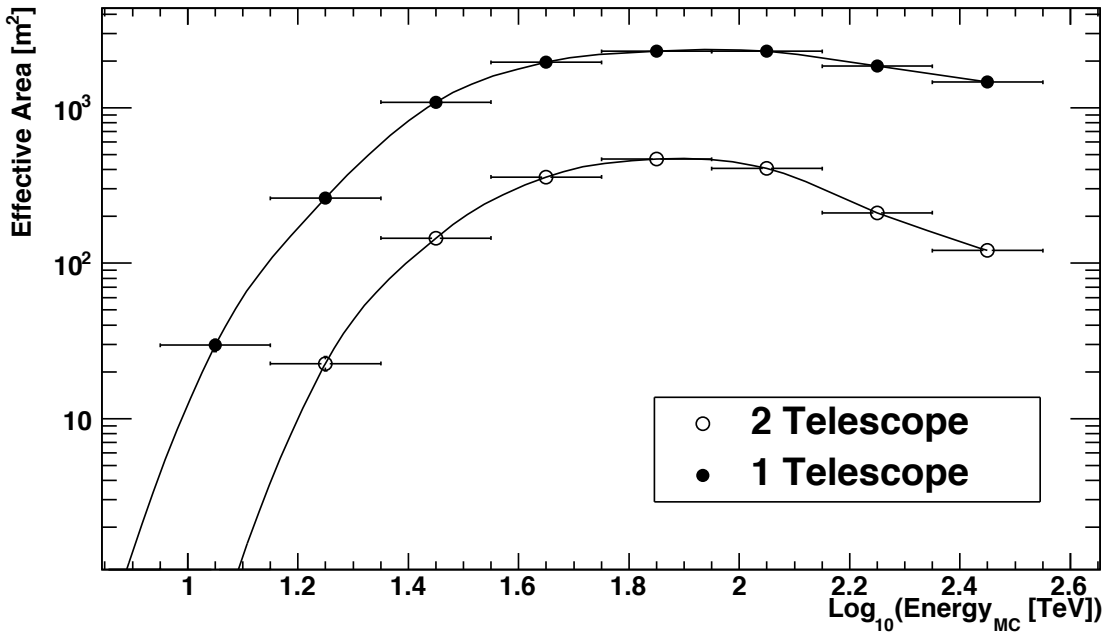

Figure 6.11: The effective area for the DC analysis is shown with a single-telescope requirement (solid circles) and a two-telescope requirement (open circles). The exposure area decreases as more telescopes are required to pass DC cuts, particularly because the DC technique is dependent on the impact parameter.

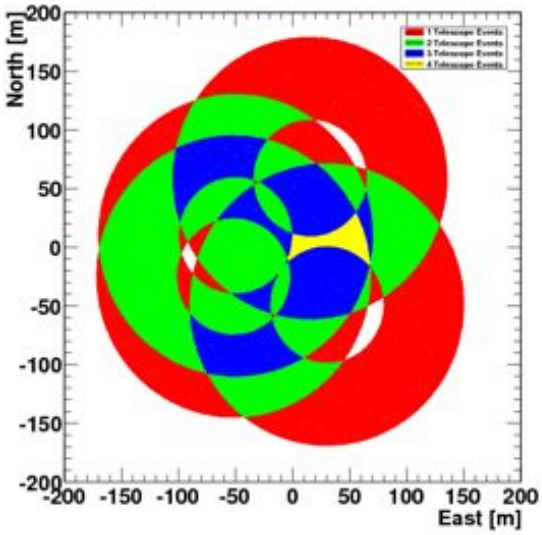

(a)

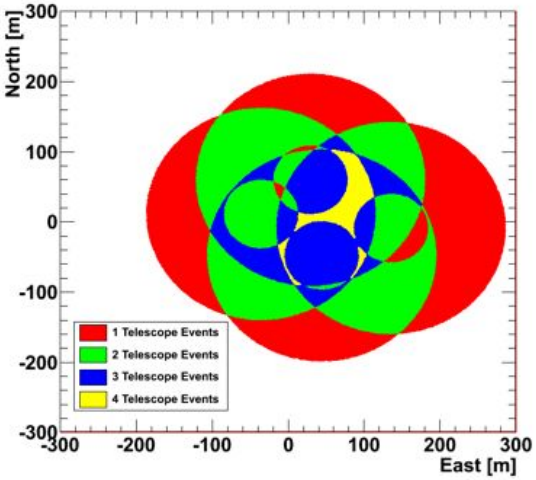

(b)

Figure 6.12: Allowed shower core locations for DC events that must pass the restrictive impact parameter cut. The configuration of the VERITAS array is shown in (a); the new VERITAS array in (b).

It is important to note, however, that careful consideration of the baselines of adjacent telescopes will expand the effective area immensely. Figure 6.12a shows the allowed core locations when events are selected to land between 50 m and 150 m from each telescope, both for the 2007-2009 VERITAS epoch (Figure 6.12a) and the new array layout (Figure 6.12b). Expanding the average baseline from 84 m to 118 m reduces the allowed area for 4-telescope events by a factor of 1.4, but the exposure for fewer than four telescopes is largely unchanged. It is important to note, however, that the new arrangement of telescopes improves the reconstruction in arrival direction for γ-ray analyses, and could improve the core reconstruction of cosmic ray air showers. Adding additional telescopes around the current array reduce the required exposure time by increasing the area in which two telescopes are optimally placed to collect direct Cerenkov light.

6.4.2 Matrix Deconvolution

The reconstructed DC events must pass through an unfolding algorithm to account for the asymmetric bias in energy reconstruction. Because events are more likely to be reconstructed to energies lower than their true energies, the spectrum that would be constructed without unfolding would be too soft. This effect can be corrected by filling a matrix with the probability that an event with true energy, E_j, would be assigned a reconstructed energy, E_i, as given by equation 6.4:

$$P(E_j|E_i) = \frac{1}{\sum_j N_{i,j}} \sum_i N_{i,j} \tag{6.4}$$

where $N_{i,j}$ is the number of simulated events that have reconstructed energy E_i and true energy E_j. The reconstructed distribution will then be given by the matrix equation $N_j =$

$P(E_j|E_i)N_i$. The deconvolution matrix used in this analysis is shown in Figure 6.13.

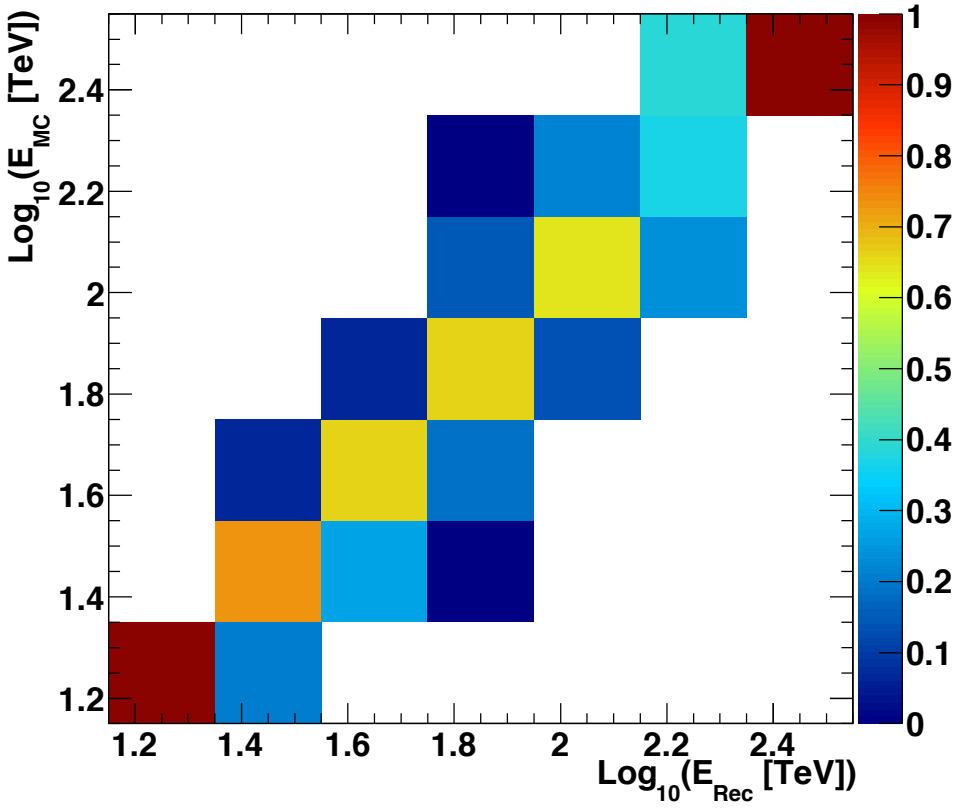

Figure 6.13: Deconvolution matrix constructed from simulated events. The matrix is used to correct for the non-Gaussian energy bias described in Section6.2.

Deconvolution techniques can be dependent on the assumed spectrum in the Monte Carlo. To ensure independence, the deconvolution matrix was tested using Monte Carlo simulations weighted using different spectral indices, as shown in Figure 6.14.

6.5 Iron Spectrum

The task remains to convert the data, binned in counts, N_i per log-energy, E_i, to a differential flux. The flux in each bin is the total counts divided by the effective aperture of the array and the total observation time. The aperture is the effective area times the solid angle subtended

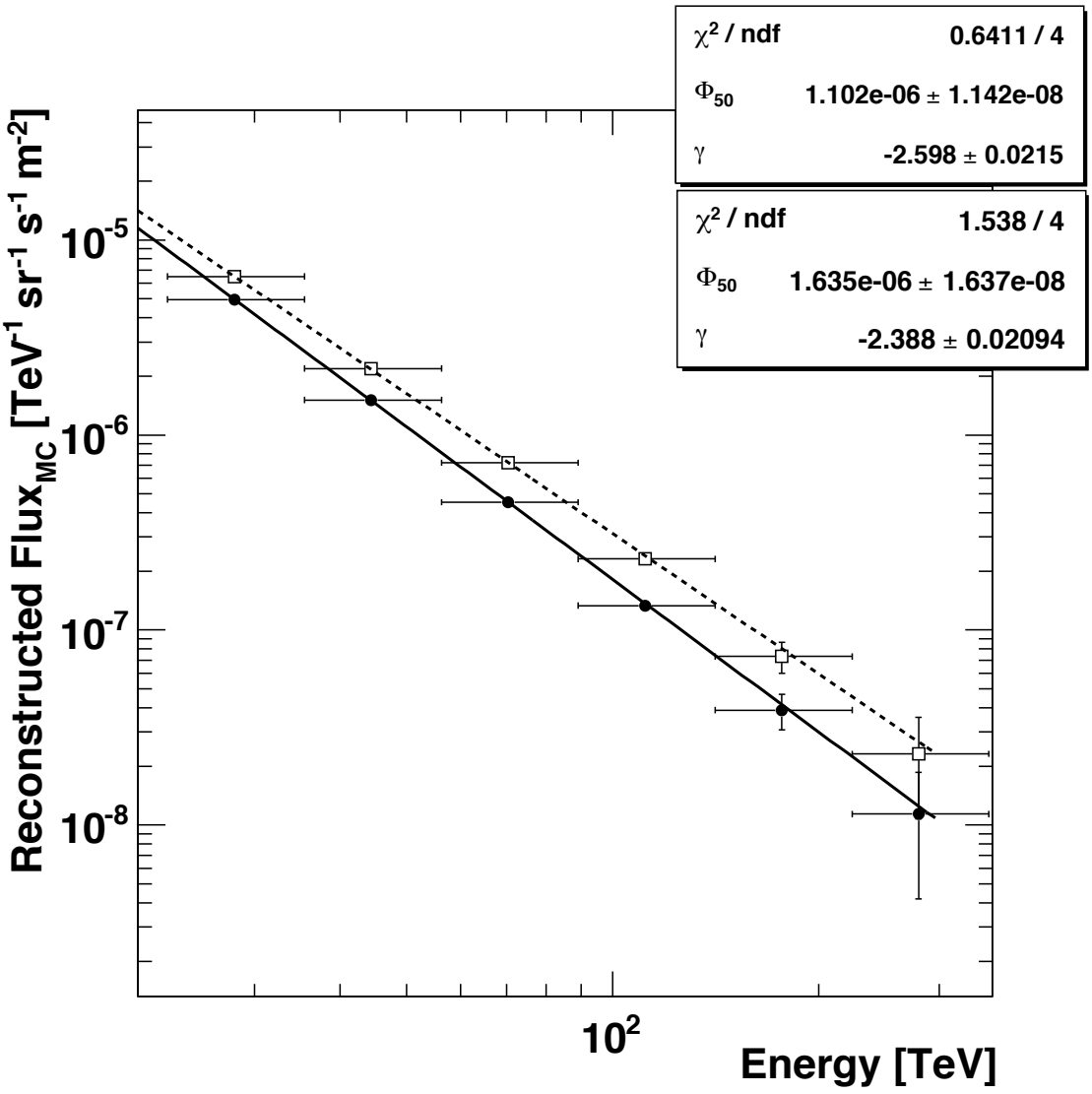

Figure 6.14: Spectrum constructed from simulated ^{56}Fe events that have been reconstructed using energy look-up tables, cut using the DC cuts described in 5.2 and re-weighted using matrix deconvolution. The input spectra of -2.68 (solid, dots) and -2.38 (dashed, square) are recovered within errors when fit to the power law function $\Phi = \Phi_{50}$ (E/50 TeV)$^{-\gamma}$.

by the telescope array, and is energy dependent. Therefore the binned flux $\Phi_i = N_i/(A_i(E)t)$. Following (Buckley et al., 1994), the differential flux of iron nuclei is related to the binned histogram of deconvolved, reconstructed energies by:

$$\Phi_i = \int_{E_i}^{E_{i+1}} \frac{d\Phi}{dE'} dE' \tag{6.5}$$

$$\Phi_i = \int_{E_i}^{E_{i+1}} \Phi_0 (E'/E_0)^{-\delta} dE' \tag{6.6}$$

assuming that the differential flux can be represented by a power law of the form $\frac{d\Phi}{dE} = \Phi_0(E/E_0)^{-\delta}$. The expectation value within each bin is equivalent to the energy, E_b, at which the flux is equal to the mean value of the power-law function across the entire bin. It is particularly important to calculate the flux at the expectation value of the assumed power-law function, because the bins are wide (Lafferty & Wyatt, 1995). They are set to be twice as wide as the energy resolution of 16.5%. Therefore the most likely value for the energy, E_b in each bin of width $\Delta E = E_{i+1} - E_i$ is given as follows:

$$\frac{d\Phi}{dE}(E_b) = \frac{1}{\Delta E} \int_{E_i}^{E_{i+1}} \Phi_0 (E'/E_0) dE' \tag{6.7}$$

$$E_b = \left(\frac{1}{\Delta E (1-\delta)} (E_{i+1}^{1-\delta} - E_i^{1-\delta}) \right)^{-1/\delta} \tag{6.8}$$

The differential flux evaluated at E_b is therefore given by:

$$\left. \frac{d\Phi}{dE} \right|_{E_b} = \Phi_i \left(\frac{\delta - 1}{E_i^{1-\delta} - E_{i+1}^{1-\delta}} \right) E_b^{-\delta} \tag{6.9}$$

Because the expectation value of the energy and the effect of differentiating over the

bin is dependent on the assumed spectrum, the process of extracting the spectrum must be performed iteratively until δ changes very little. For this analysis, the tolerance on the differential index is set to 0.1%.

Fluctuations in the counting rates follow a Poisson distribution. Likewise the error in estimating the effective area curves contributes another term to the overall error due to the statistical error in the Monte Carlo simulations. Adding these terms in quadrature gives the statistical error for each data point:

$$\sigma_i^2 = \Phi_i^2 \left(\frac{1}{N} + \frac{\sigma_A^2}{A^2} \right) \tag{6.10}$$

Equation 6.10 represents the error in the flux when the number of events in a given energy bin follows Gaussian statistics, i.e., when the number of events in that bin is greater than 10. For bins with fewer than ten events, the errors become asymmetric and must follow Poisson statistics. In that case, the error is given by:

$$\sigma_i^2 = \Phi_i^2 \left(\frac{\sigma_N^2}{N^2} + \frac{\sigma_A^2}{A^2} \right) \tag{6.11}$$

where σ_N is given by the 1 σ=0.8413 values listed in Table 1 for the upper limits and Table 2 for the lower limits of Gehrels (1986).

The final spectrum of iron nuclei is shown in Figure 6.15. The data are fit by a function anchored at 50 TeV to minimize the errors in the fitting, such that that the overall flux can be represented by the power law: $\Phi = (5.8 \pm 0.84_{stat} \pm 1.2_{sys}) \times 10^{-7} (E/50 \text{ TeV})^{-2.84 \pm 0.30_{stat} \pm 0.3_{sys}}$ TeV^{-1} m^{-2} sr^{-1} s^{-1}. The measurement extends from 22 TeV to >140 TeV with no sign of a cutoff in energy. The systematic uncertainty used is typical analyses of VERITAS data, and is estimated to be 20% in the flux normalization and 0.3 in the spectral index.

Table 6.1: The flux points in the iron spectrum measured by VERITAS. The expectation value, E_b, and the minimum, E_{min}, and maximum energy, E_{max}, of each bin are listed in kinetic energy per particle (TeV). The flux is given in $\mathrm{m}^{-2}\ \mathrm{sr}^{-1}\ \mathrm{s}^{-1}\ \mathrm{TeV}^{-1}$.

E_b	E_{min}	E_{max}	Counts	Flux
28	22	35	17	$(2.62 \pm 0.64) \times 10^{-6}$
44	35	56	26	$(1.03 \pm 0.20) \times 10^{-6}$
70	56	89	11	$(2.10 \pm 0.63) \times 10^{-7}$
112	89	141	3	$(3.63^{+3.53}_{-1.98}) \times 10^{-8}$

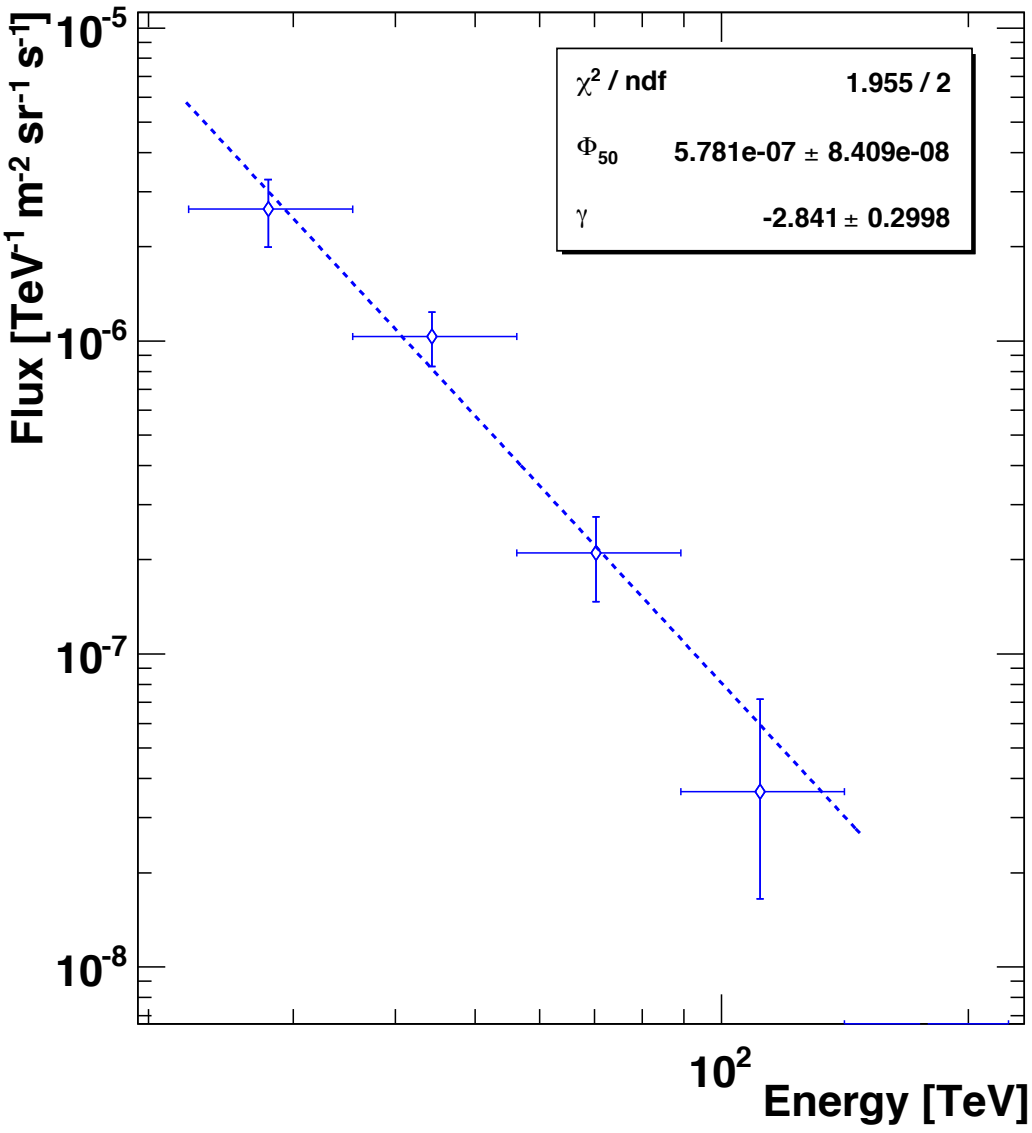

Figure 6.15: The energy spectrum of iron as determined by VERITAS using the direct Cerenkov technique ranging from 22 TeV to 141 TeV. Statistical errors are shown and described more in the text. The results of a fit to the function $\Phi = \Phi_{50}(E/50 \text{ TeV})^{-\gamma}$ are listed in the legend.

CHAPTER 7

CONCLUSIONS

The measurement of the iron spectrum extends from 22 TeV to 141 TeV and overlaps with measurements made by balloon-borne experiments as well as previous measurements of the iron spectrum using the DC technique. With a charge resolution of 21.5% and energy resolution of 24%, these data are among the most-precise measurements made by a ground-based instrument. The cuts developed for this analysis have a overall proton rejection power of 2.25×10^7, and the level of contamination from nuclei other than iron is less than the 14%.

These data are in good agreement with previous measurements of iron spectrum, as shown in Figures 7.1 and 7.2. Direct measurements from the balloon-borne experiments TRACER (Ave et al., 2008) and ATIC (Panov et al., 2006) and the space-borne experiments HEAO-3 (Binns et al., 1988), and CRN (Grunsfeld et al., 1988) extend to > 80 TeV. They agree well with the measurements made here by VERITAS and previously by H.E.S.S. (Aharonian et al., 2007b) using the ground-based direct Cerenkov technique, which extend to higher energies.

Key to understanding the composition of cosmic rays is measuring the composition at knee energies to a high precision. These data measure the flux of iron nuclei with good charge resolution, but energies a factor of ten below the knee of the all-particle spectrum. Observing the expected break in the iron spectrum – and other nuclei as well – will constrain models of diffusive shock acceleration, while comparing the ratio of iron nuclei to sub-iron nuclei at high energies can constrain the propagation models and help elucidate the distribution of sources throughout the galaxy. In order to make precision measurements at PeV energies using the DC technique, arrays must be constructed such that they achieve large effective areas and have the ability to separate DC light from the air shower light with nanosecond time sampling and 0.01° angular resolution.

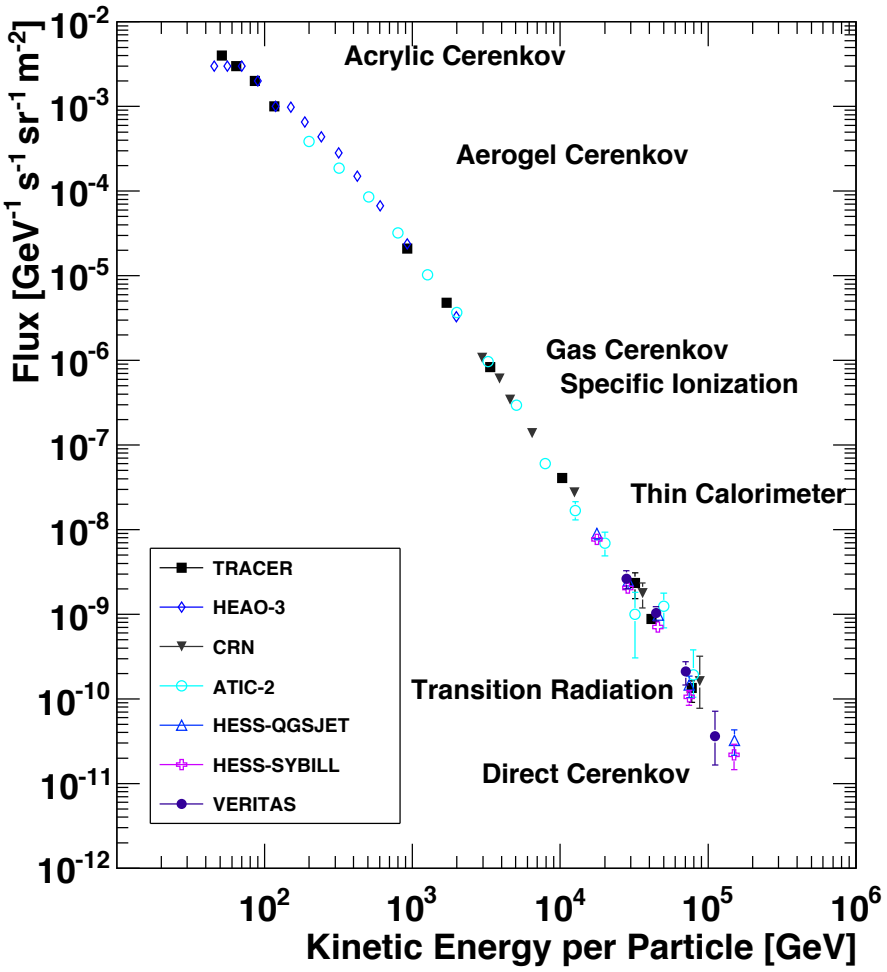

Figure 7.1: The spectrum of iron as measured by VERITAS compared with direct techniques shows that many different methods agree up to 141 TeV.

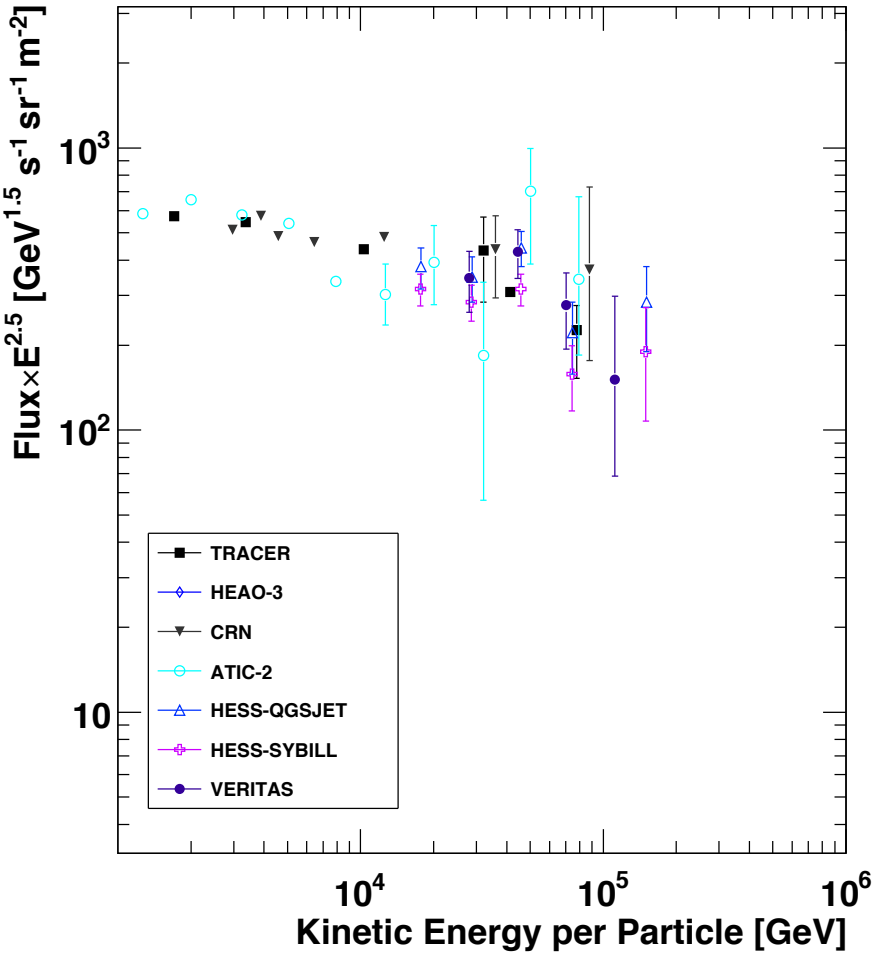

Figure 7.2: The measured spectrum of iron from 1 TeV to $>$ 140 TeV enhanced by a factor of $E^{2.5}$ so that the spectral features are more visible.

As discussed in Section 6.4.1, care should be taken in selecting the baselines of a telescope array meant to use the DC technique, because the telescope must be within the narrow Cerenkov light cone of the primary particle. Requiring that at least two telescopes collect DC light can reduce the effective area dramatically, but is necessary to ensure that the light identified as DC light is not due to a shower fluctuation or noise in the cameras.

The new VERITAS array (shown in 6.12b) has an improved collection area for high-energy events and better angular resolution, but is less likely to collect DC light in all four telescopes, because the array from the 2007–2009 epoch had two telescopes placed very close to each other. However, the area over which four telescopes could collect DC light can increase by a factor of five simply by adding one telescope, as shown in Figure 7.3b. Close-packing of the telescopes optimizes the number of telescopes available to image DC light. Based on the effective areas shown Figure 7.3c and in Figure 7.3, the effective area of the close-packing case is a factor of two greater than for the array with wider baselines. Table 7.1 shows that adding four will double the effective area, but the arrangement determines what fraction are four-telescope events.

The DC technique is optimized for high-mass nuclei and permits the search for exotic particles. Particularly interesting would be the observation of the direct Cerenkov light from magnetic monopoles with a predicted charge quantized in integer multiples of 68.5 (Dirac, 1931). The most stringent upper limit on the flux of magnetic monopoles was placed by the MACRO collaboration at $10^{-16}\mathrm{cm}^{-2}\mathrm{sr}^{-1}\mathrm{s}^{-1}$ (MACRO Collaboration et al., 2002). While VERITAS and TrICE cannot constrain the flux of monopoles at such a low level, a dedicated experiment employing the direct Cerenkov technique could exceed the flux sensitivity in less than 300 hours with a 10° field-of-view and 1 km^2 effective area.

TrICE demonstrates that MAPMT cameras can be used in Cerenkov telescopes and fully resolve cosmic-ray air showers. Measurements made by VERITAS and H.E.S.S. show that the direct Cerenkov method is a viable way to measure the composition of heavy nuclei at

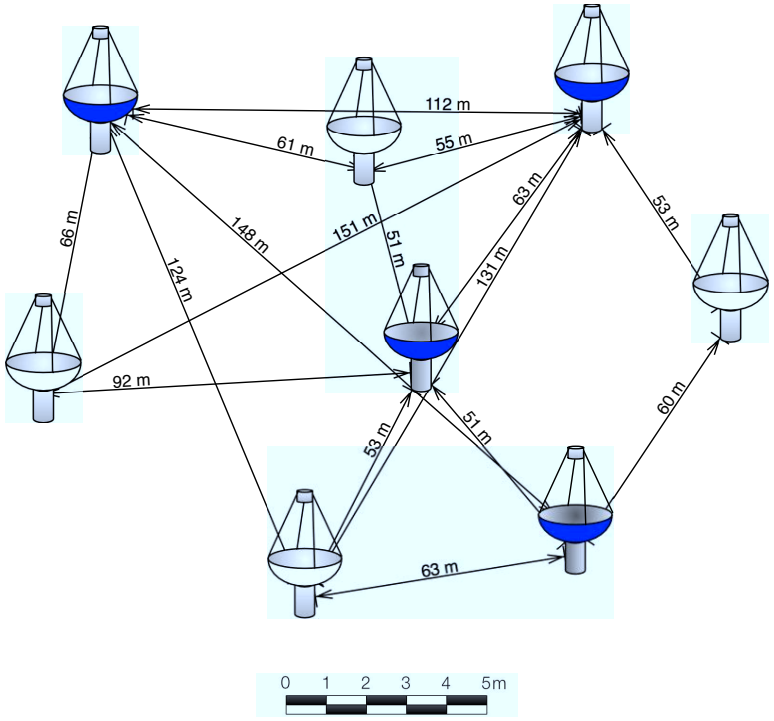

(a)

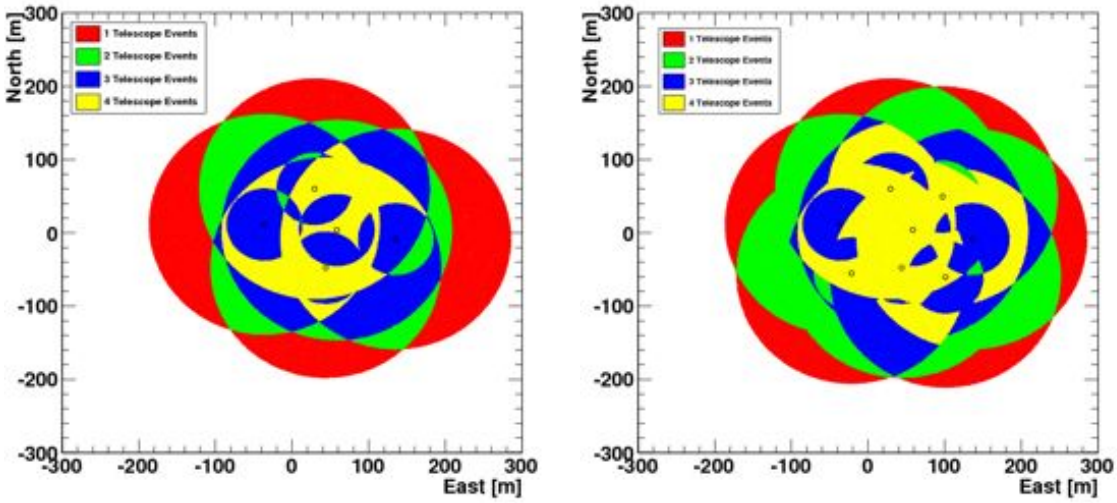

(b) (c)

Figure 7.3: The area over which four telescope events can be observed is expanded by adding one central telescope to the modern VERITAS array (b). Adding three more telescopes placed such that the new baselines are between 50 m and 150 m expands the four-telescope and two-telescope effective area (c). The modern VERITAS array are shown in (a) as grey telescopes, while the additional telescopes are shown in blue in a close-packed arrangement.

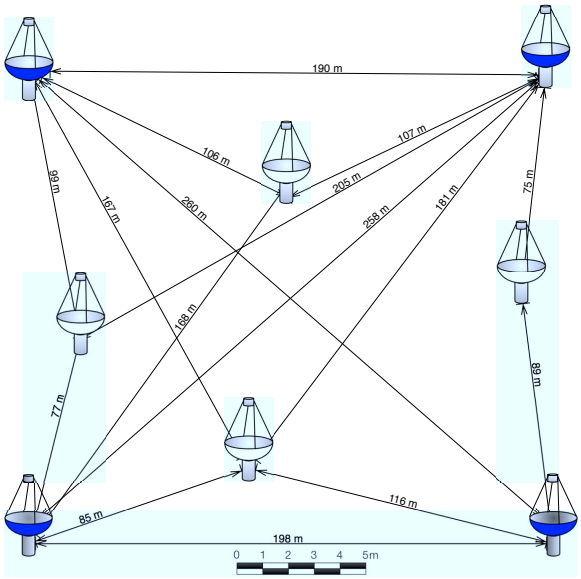

(a)

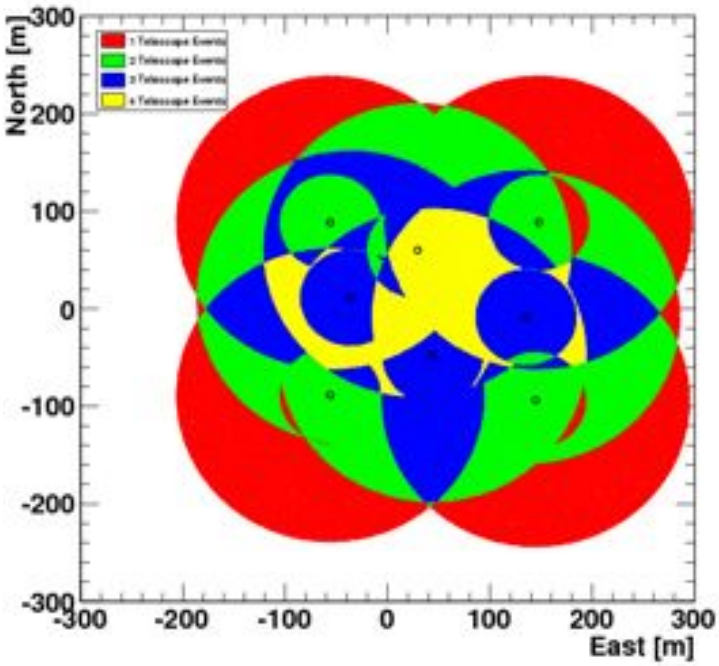

(b)

Figure 7.4: Placing four telescopes at wider baselines increases the four-telescope effective area over the existing VERITAS array, but by less than when the telescopes are more densely packed. The colors are as in 7.3.

TeV energies. The data presented in this work of the spectrum of iron nuclei are among the most precise made in this energy regime by a ground-based instrument.

Table 7.1: The gains in effective area are given. The total gain includes events in which two or more telescopes can image DC light; the "4-Tel." column indicates the gain in effective area for 4 or more telescopes; the "3-Tel." column, for 3 telescopes. The arrangements refer to adding one telescope (as in Figure 7.3b), adding four telescopes in a close-packed arrangement (as in Figure 7.3c), and adding four telescopes with longer baselines (as in Figure 7.4).

Arrangement	Additional Telescopes	Total	4-Tel.	3-Tel
Central Telescope	1	1.5	5.4	2.7
Close Packing	4	2.1	9.7	3.6
Long Baseline	4	2.0	4.8	2.8

APPENDIX A

SELECTED DATA

Data accumulated by VERITAS are selected for the direct Cerenkov analysis using the three following criteria. Four telescopes actively collect data during the run, to minimize the number of simulations necessary to reproduce the data and to maximize the array's exposure. Data taken with a mean elevation between 70° and 80° to decrease the amount of material through which the Cerenkov light traverse and minimize scattering. Data must be collected during good weather conditions, defined by the observer's assessment of the conditions and the far-infrared (FIR) cameras mounted on the first and third telescopes. Dry, cool weather manifests itself in the FIR data as a steady temperature at $\sim -40^\circ$ F. When clouds pass over the telescopes, the temperature of the FIR varies substantially and this is also reflected in the rates in the L2 systems. The total data amassed corresponds to 397 hours, collected at a mean rate of 220 ± 34 Hz.

Data were taken in three distinct modes relevant to $\gamma-$ray observations: tracking, survey and wobble modes. When the array operates in the tracking mode, it follows the ascent of the object at which it points the telescope as it moves through the sky. When run in the wobble mode, the telescopes track a position slightly displaced from the source position so as to collect more background (cosmic ray) data from the region of the sky expected to have a negligible γ-ray flux. This enables observers to collect signal and background data simultaneously, thereby increasing the amount of time available spent observing the source. Survey mode permits following a certain region of the sky as well, but with the intention of generating a uniform exposure across the field-of-view.

Table A.1: Comparison of the modes of observation used in the cosmic-ray analysis

Mode	% Galactic	% Extragalactic	Time [min]	Elevation [°]	Rate [Hz]
Wobble	24	75	22063	74.1±3.1	224±34.1
Survey	100	0	1560	74.2±3.0	223.8±26
On/Off	9	91	220	73.2±2.7	257±76.2
Tracking	0	100	10	73±1.4	244±11.3

REFERENCES

Abbasi, R. et al. 2005, Physics Letters B, 619, 271

Abbasi, R., Desiati, P., & the IceCube Collaboration. 2009, ArXiv e-prints 0907.0498

Abbasi, R. U. et al. 2009, ArXiv e-prints 0910.4184

Abdo, A. A. et al. 2008, ArXiv e-prints 0801.3827, 801

Abdo, A. A. et al. 2009, The Astrophysical Journal Letters, 700, L127

Abraham, J. et al. 2010a, Physics Letters B, 685, 239

—. 2010b, ArXiv e-prints

Acciari, V. A. et al. 2010, ArXiv e-prints 1002.2974

—. 2009a, ApJ, 703, L6

—. 2009b, ApJ, 698, L133

Aharonian, F. et al. 2001, A&A, 370, 112

—. 2008a, A&A, 486, 829

—. 2008b, A&A, 490, 685

—. 2008c, A&A, 481, 401

—. 2007a, A&A, 464, 235

—. 2007b, Phys. Rev. D, 75, 042004

Aharonian, F. et al. 2007, The Astrophysical Journal, 661, 236

Aharonian, F. et al. 2009, ApJ, 692, 1500

Ahn, H. et al. 2008, Astroparticle Physics, 30, 133

Ahn, H. S. et al. 2009, ApJ, 707, 593

Albert, J. et al. 2007a, ApJ, 664, L87

—. 2007b, A&A, 474, 937

Amenomori, M. et al. 2006, Science, 314, 439

Amsler, C., et al. 2008, Phys. Lett., B667, 1

Antoni, T. et al. 2005, Astroparticle Physics, 24, 1

Antoni, T. et al. 2005, Astroparticle Physics, 24, 1

Arqueros, F., Ros, G., Elorza, G., & García-Pinto, D. 2005, Astroparticle Physics, 24, 137

Ave, M., Boyle, P. J., Gahbauer, F., Hoppner, C., Horandel, J. R., Ichimura, M., Muller, D., & Romero-Wolf, A. 2008, ArXiv e-prints 0801.0582, 801

Battistoni, G., Cerutti, F., Fassò, A., Ferrari, A., Muraro, S., Ranft, J., Roesler, S., & Sala, P. R. 2007, in American Institute of Physics Conference Series, Vol. 896, Hadronic Shower Simulition Workshop, ed. M. Albrow & R. Raja, 31–49

Bell, A. R. 1978a, MNRAS, 182, 147

—. 1978b, MNRAS, 182, 443

Bell, A. R., & Lucek, S. G. 2001, MNRAS, 321, 433

Berezinsky, V. S., Grigorieva, S. I., & Hnatyk, B. I. 2004, Astroparticle Physics, 21, 617

Binns, W. et al. 2008, New Astronomy Reviews, 52, 427 , astronomy with Radioactivities. VI - Proceedings of International Workshop Held at Ringberg Castle of Max Planck Gesellschaft in Kreuth, Germany, 7-10 January 2008

Binns, W. R., Garrard, T. L., Israel, M. H., Jones, M. D., Kamionkowski, M. P., Klarmann, J., Stone, E. C., & Waddington, C. J. 1988, ApJ, 324, 1106

Binns, W. R. et al. 2005, ApJ, 634, 351

Blandford, R. D., & Ostriker, J. P. 1978, ApJ, 221, L29

Bradbury, S. 1999, in International Cosmic Ray Conference, Vol. 5, International Cosmic Ray Conference, 280

Buckley, J., Dwyer, J., Mueller, D., Swordy, S., & Tang, K. K. 1994, ApJ, 429, 736

Burbidge, E. M., Burbidge, G. R., Fowler, W. A., & Hoyle, F. 1957, Reviews of Modern Physics, 29, 547

Butt, Y. 2009, Nature, 460, 701

Byrum, K., Cunningham, J., Drake, G., & et al. 2008, in International Cosmic Ray Conference, Vol. 2, International Cosmic Ray Conference, 469–472

Compton, A. H., & Getting, I. A. 1935, Phys. Rev., 47, 817

Cronin, J. W., Gaisser, T. K., & Swordy, S. P. 1997, Scientific American, 276, 32

Cundiff, T. et al. 2006, IEEE Transactions on Nuclear Science, 53, 1347

Cutler, D. J., & Groom, D. E. 1986, Nature, 322, 434

Davies, J. M., & Cotton, E. S. 1957, Journal of Solar Energy, 1, 16

Dirac, P. A. M. 1931, Royal Society of London Proceedings Series A, 133, 60

Drury, L. 1983, Space Science Reviews, 36, 57

Drury, L. O. ., & Aharonian, F. A. 2008, Astroparticle Physics, 29, 420

Duke, C., & Lebohec, S. 2010, GrISU(tah) http://www.physics.utah.edu/gammaray/GrISU/

Fermi, E. 1949, Phys. Rev., 75, 1169

Fermi LAT Collaboration, & Abdo, A. A. 2009, ArXiv e-prints 0911.5327

Fowler, J. W. 2000, PhD thesis, The University of Chicago

Frank, I., & Tamm, I. 1937, C. R. Acad. Sci USSR, 14

Gaisser, T. K. 1990, Cosmic rays and particle physics (Cambridge University of Press)

Garcia-Munoz, M., Mason, G. M., & Simpson, J. A. 1977, ApJ, 217, 859

Gehrels, N. 1986, ApJ, 303, 336

George, J. S. et al. 2009, The Astrophysical Journal, 698, 1666

Gough, M. P. 1976, Journal of Physics G: Nuclear Physics, 2, 965

Greisen, K. 1966, Phys. Rev. Lett., 16, 748

Grunsfeld, J. M., L'Heureux, J., Meyer, P., Müller, D., & Swordy, S. P. 1988, ApJ, 327, L31

Guzik, T. et al. 2008, Advances in Space Research, 42, 424

Heck, D., Knapp, J., Capdevielle, J. N., Schatz, G., & Thouw, T. 1998, CORSIKA: a Monte Carlo code to simulate extensive air showers., ed. Heck, D., Knapp, J., Capdevielle, J. N., Schatz, G., & Thouw, T.

Heitler, W. 1954, Quantum theory of radiation, ed. Heitler, W.

Higdon, J. C., & Lingenfelter, R. E. 2003, ApJ, 590, 822

Hillas, A. 2005, Journal of Physics G: Nuclear and Particle Physics, 31, R95

Hillas, A. M. 1984, Annual Review of Astronomy and Astrophysics, 22, 425

Hillas, A. M. 1985, in Proceedings of the 19th International Cosmic Ray Conference, La Jolla, Vol. 3, 445–448

—. 1996, Space Science Reviews, 75, 17

Hofmann, W., Jung, I., Konopelko, A., Krawczynski, H., Lampeitl, H., & Pühlhofer, G. 1999, Astroparticle Physics, 12, 135

Holder, J. et al. 2006, Astroparticle Physics, 25, 391

Horan, D., & Wakely, S. 2008, in AAS/High Energy Astrophysics Division, Vol. 10, AAS/High Energy Astrophysics Division

Humensky, T. B. 2005, ArXiv Astrophysics e-prints 0507449

Hunter, S. D. et al. 1997, ApJ, 481, 205

Kieda, D. B., Allen, D., Hall, J., Nagai, T., Snure, M., Vassilev, V. V., & Walker, G. 2003, in International Cosmic Ray Conference, Vol. 5, International Cosmic Ray Conference, 2835–+

Kieda, D. B., Swordy, S. P., & Wakely, S. P. 2001, Astropart. Phys., 15, 287

Krymskii, G. F. 1977, Akademiia Nauk SSSR Doklady, 234, 1306

Lafferty, G. D., & Wyatt, T. R. 1995, Nuclear Instruments and Methods in Physics Research A, 355, 541

Lagage, P. O., & Cesarsky, C. J. 1983, A&A, 125, 249

Lewis, D. A. 1990, Experimental Astronomy, 1, 213

Longair, M. S. 1992, High energy astrophysics. Vol.1: Particles, photons and their detection, ed. Longair, M. S.

—. 1994, High energy astrophysics. Vol.2: Stars, the galaxy and the interstellar medium, ed. Longair, M. S.

MACRO Collaboration, Ambrosio, M., & et al. 2002, European Physical Journal C, 25, 511

Matthews, J. 2005a, Astroparticle Physics, 22, 387

—. 2005b, Astroparticle Physics, 22, 387

McCann, A., Hanna, D., & McCutcheon, M. 2009, in International Cosmic Ray Conference

Mohanty, G. et al. 1998, Astroparticle Physics, 9, 15

Müller, D. 2009, in International Cosmic Ray Conference

Naumann-Godo, M., Beilicke, M., Hauser, D., Lemoine-Goumard, M., & de Naurois H.E.S.S. Collaboration, M. 2008in (AIP), 304–307

Ong, R. A. 1998, Phys. Rep., 305, 93

—. 2003, The Extreme Universe, Colloquium, Department of Physics, University of California, Irvine (UCI)

Panov, A. D. et al. 2006, ArXiv Astrophysics e-prints 0612377

Perrone, L. 2008, in International Cosmic Ray Conference, Vol. 4, International Cosmic Ray Conference, 331–334

Porter, T. A., Moskalenko, I. V., , & Strong, A. W. 2006, The Astrophysical Journal Letters, 648, L29

Roache, E., Irvin, R., Perkins, J. S., & et al. 2008, in International Cosmic Ray Conference, Vol. 3, International Cosmic Ray Conference, 1397–1400

Rossi, B., & Greisen, K. 1941, Rev. Mod. Phys., 13, 240

Salvati, M., & Sacco, B. 2008, A&A, 485, 527

Seo, E. S., & Ptuskin, V. S. 1994, ApJ, 431, 705

Sitte, K. 1965, in International Cosmic Ray Conference, Vol. 2, 887

Skwarnicki, T. 2005, Nuclear Instruments and Methods in Physics Research Section A: Accelerators, Spectrometers, Detectors and Associated Equipment, 553, 339 , proceedings of the fifth International Workshop on Ring Imaging Detectors

Sokolsky, P. 1989, Frontiers in Physics, 76

Sood, R. K. 1983, Nature, 301, 44

Streitmatter, R. E., & Jones, F. C. 2005, in Proceedings of the 29th International Cosmic Ray Conference, Puna, Vol. 3, 157–160

Strong, A. W., Moskalenko, I. V., & Ptuskin, V. S. 2007, Annual Review of Nuclear and Particle Science, 57, 285

Swordy, S. P., Mueller, D., Meyer, P., L'Heureux, J., & Grunsfeld, J. M. 1990, ApJ, 349, 625

Takeda, M. et al. 1998, Physical Review Letters, 81, 1163

The HESS Collaboration: F. Acero. 2009, ArXiv e-prints 0909.4651

The Pierre Auger Collaboration: J. Abraham et al. 2009, ArXiv e-prints 0906.2189

Uchiyama, Y., Aharonian, F. A., Tanaka, T., Takahashi, T., & Maeda, Y. 2007, Nature, 449, 576

Vassiliev, V. V., Hall, J., Kieda, D. B., Moses, J., Nagai, T., & Smith, J. 2003, in International Cosmic Ray Conference, Vol. 5, International Cosmic Ray Conference, 2851

VERITAS Collaboration et al. 2009, Nature, 462, 770

VERITAS Collaboration: T. Nagai, McKay, R., Sleege, G., & Petry, D. 2007, ArXiv e-prints 0709.4517

Weekes, T. C. et al. 1989, ApJ, 342, 379

Weinstein, A. 2008, in International Cosmic Ray Conference, Vol. 3, International Cosmic Ray Conference, 1539–1542

Weinstein, A. 2009, ArXiv e-prints 0912.4492

White, R. J. 2005, in American Institute of Physics Conference Series, Vol. 745, High Energy Gamma-Ray Astronomy, ed. F. A. Aharonian, H. J. Völk, & D. Horns, 797–802

Wibig, T., & Wolfendale, A. W. 2004, ArXiv Astrophysics e-prints 0410624

Zatsepin, G. T., & Kuz'min, V. A. 1966, Soviet Journal of Experimental and Theoretical Physics Letters, 4, 78